Nonlinear gyrokinetic simulations of intrinsic rotation in up-down asymmetric tokamaks

by

Justin Richard Ball

Submitted to the Department of Nuclear Science and Engineering
in partial fulfillment of the requirements for the degree of

Master of Science in Nuclear Science and Engineering

at the

MASSACHUSETTS INSTITUTE OF TECHNOLOGY

September 2013

Author .....
Justin R. Ball
Department of Nuclear Science and Engineering
August 20, 2013

Certified by .....
Felix I. Parra
Assistant Professor
Thesis Supervisor

Certified by .....
Peter J. Catto
Assistant Director, Plasma Science and Fusion Center
Thesis Reader

Accepted by .....
Mujid S. Kazimi
TEPCO Professor of Nuclear Engineering
Chair, Department Committee on Graduate Students

Nonlinear gyrokinetic simulations of intrinsic rotation in up-down asymmetric tokamaks

by

Justin Richard Ball

Submitted to the Department of Nuclear Science and Engineering
on August 23, 2013, in partial fulfillment of the
requirements for the degree of
Master of Science in Nuclear Science and Engineering

Abstract

Experiments and theory show that tokamak plasmas with strong toroidal rotation and rotation shear can suppress turbulent energy transport as well as allow violation of the Troyon β limit. However, using external neutral beams to inject toroidal momentum, as is done in many current experiments, would require a prohibitive amount of energy in larger, reactor-sized devices. The most promising alternative to achieve significant mean plasma flow that scales to large devices is intrinsic rotation, the rotation that is observed in the absence of external momentum injection. Intrinsic rotation is observed in current experiments, but is generated by effects that are formally small in $\rho_* \equiv \rho_i/a$, the ratio of the ion gyroradius to the tokamak minor radius. These effects are insufficient in anticipated reactors because ρ_* will be significantly smaller.

Recent theoretical work concludes that up-down asymmetry in the poloidal cross-section of tokamaks can drive intrinsic rotation to lowest order in ρ_* [1, 2]. In this thesis, we extend GS2, a local δf gyrokinetic code that self-consistently calculates momentum transport, to permit up-down asymmetric configurations. MHD analysis shows that ellipticity is most effective at introducing up-down asymmetry throughout the plasma. Accordingly, tokamaks with tilted elliptical poloidal cross-sections were simulated in GS2 to determine nonlinear momentum transport. The results suggest that the current experimentally measured rotation levels can be generated in reactor-sized devices using up-down asymmetry.

Surprisingly, linear and nonlinear gyrokinetic simulations also suggest that tilted elliptical flux surfaces may naturally suppress turbulent energy transport. Using cyclone base case parameters [3] (except for an elongation $\kappa = 2$), a 40% reduction in the linear turbulent growth rate was observed by tilting the flux surface $\pi/4$ from vertical. However, this reduction of energy transport was not observed when the background temperature gradient was increased by 50%.

Thesis Supervisor: Felix I. Parra
Title: Assistant Professor

Acknowledgments

I would like to thank fusion's entering class of 2011, star-crossed as we were, for providing me with a community worthy of MIT. I would like thank my family and friends, in particular Carter Wang and Matthew Bouse for keeping me honest socially. I would like to thank Peter Catto for recruiting me to MIT and for his understanding during the inevitable last minute thesis rush. Lastly, and most importantly, I would like to thank my advisor Felix for devoting more time to my instruction than graduate school stereotypes would have you think possible. I hope you, the reader, will find this work a direct reflection of that.

Contents

List of Figures

List of Tables

Chapter 1

Introduction

The nuclear fusion community is fairly unique in its possession of an idealistic and unambiguous common goal: to produce an economical fusion power plant. A fusion power plant generates base load electricity using virtually unlimited, cheap, and accessible fuel. It cannot meltdown and, relative to fission power, creates little radioactive waste or proliferation concerns. Fundamentally one must bring two light nuclei, generally deuterium and tritium, close enough for the strong nuclear force to overcome Coulomb repulsion and bind them. This Coulomb barrier is measured in 10's of keV whereas the strength of chemical bonds is measured in eV. This factor of 10^4 suggests that relying on solid materials to confine/compress fuel, as is frequently the case in cold fusion schemes, is unrealistic. Also, when two nuclei interact, a scattering collision is more than 10 times as likely as a fusion reaction [4]. This, for the most part, makes particle accelerators infeasible as a means to generate net energy. The focus of this work will be within the field of Magnetic Confinement Fusion (MCF), one of two approaches that dominate fusion research.

In MCF, the fuel is confined and heated to the temperatures necessary to overcome the Coulomb barrier, fuse nuclei, and produce energy. However, these temperatures are around 20 keV or 100 Million °C, which precludes any contact between the fuel and solid material. This temperature also ionizes the fuel and creates a charged gas, called a plasma. Since, ideally, the Lorentz force constrains charged particles to follow a magnetic field, the plasma can be confined using magnetic field lines that do not

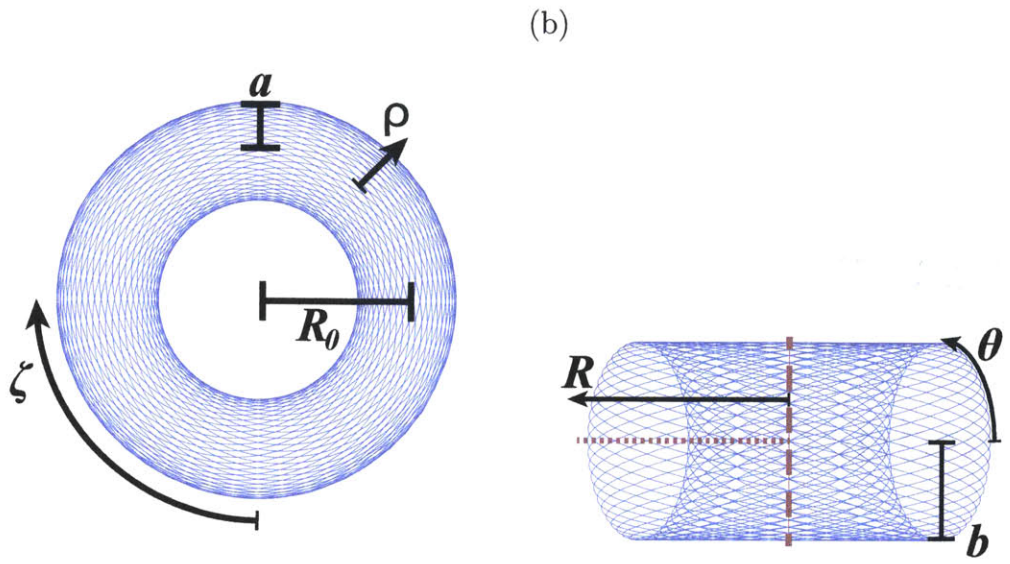

Figure 1-1: Outermost magnetic field lines of an example elliptical tokamak viewed from (a) above and (b) the side with the axis of symmetry (red, dashed) and midplane (red, dotted). Also shown are the major radial coordinate R, minor radial coordinate ρ, poloidal coordinate θ, toroidal angle ζ, tokamak major radius R_0, tokamak minor radius a, and the edge elongation $\kappa_b \equiv \frac{b}{a}$.

contact solid walls. This work focuses exclusively on a MCF device with such a closed magnetic field geometry called the tokamak.

The first tokamak was built in 1956 and, ever since, has consistently produced the best results of any MCF design. It keeps a toroidally symmetric plasma confined using the magnetic field produced by the current in a complex web of coils and the plasma itself. The toroidal symmetry guarantees that the magnetic field lines form nested surfaces, called flux surfaces. Originally, tokamaks were constructed with flux surfaces that had circular cross-sections, but quickly advanced to elliptical (see fig. 1-1) and then D-shaped.

However, despite the success of the tokamak, results have never been as good as was initially hoped. Since particles are constrained to follow field lines it was thought that the confinement losses may only be caused by collisions between particles. Collisions allow particles to change field lines and gradually diffuse out of the machine. This is referred to as classical and neoclassical confinement and has turned out to be too optimistic. What experiments have discovered is that plasma turbulence dominates confinement losses. These electromagnetic fluctuations are driven

by background gradients in plasma temperature and density and ultimately dictate the minimum size, required heating power, and economic viability of a fusion power plant.

This work is focused on the effects of the poloidal cross-section shape on the turbulent transport of energy and momentum. Specifically, it investigates tokamaks with poloidal cross-sections that are not symmetric about the midplane, referred to as up-down asymmetric tokamaks. This chapter attempts to provide context by describing both the work that enables this thesis and recent research that is important in interpreting results. Since little work of any kind has been done for up-down asymmetric tokamaks, Chapter 2 presents simple MHD analysis that helps to identify feasible configurations. Chapter 3 provides a description of the turbulence analysis code GS2 and how it was utilized in this work. A general investigation of energy confinement properties is given in Chapter 4, whereas Chapter 5 presents a focused discussion of GS2 momentum transport results and how they compare to experiment. Lastly, Chapter 6 summarizes the most noteworthy points of this thesis.

1.1 Motivation

Fundamentally, the motivation for advocating a new tokamak configuration must be economic. The ultimate goal of the field is to produce a fusion power plant with the lowest possible cost of electricity and any new design must appeal to this.

1.1.1 Cost of fusion power

Because the fuel is expected to be relatively inexpensive, we are mostly seeking to minimize the capital cost of the reactor. ITER [5] is the flagship fusion experiment, currently under construction in France, which we will take to be indicative of the cost breakdown of a future reactor. From table 1.1, we see that the magnets are the most expensive component, the machine core dominates the total cost, and heating/current drive is relatively inexpensive. Therefore, as a rough approximation, we can say that cost is only dependent on the magnetic field produced and the plasma volume.

Component	Cost (% of total)
Machine core	**53**
Magnet systems	28
Vacuum vessel	8
Blanket system	6
Divertor	3
Machine assembly	3
Cryostat	3
Thermal shields	1
Vacuum pumping & fueling system	1
Auxiliaries	**33**
Buildings	14
Power supplies & distribution	8
Cooling water systems	5
Cryoplant & distribution	3
Remote handling equipment	2
Tritium plant	1
Waste treatment & storage	0
Radiological protection	0
Heating and current drive	**7**
Electron cyclotron	3
Neutral beam	3
Ion cyclotron	1
Miscellaneous	**7**
Diagnostics	4
Control, data access, & communication	2
Other	1

Table 1.1: ITER direct capital cost breakdown (table adapted from ref. [5]).

This approximation clearly favors devices that can contain more and hotter plasma at the same toroidal field. This confinement efficiency is quantified by the toroidal plasma beta,

$$\beta_T \equiv \frac{2\mu_0 \langle p \rangle_V}{B_0^2}, \tag{1.1}$$

where $\langle p \rangle_V$ is the volume-averaged plasma pressure, μ_0 is the vacuum magnetic permeability, and B_0 is the on-axis toroidal magnetic field. Furthermore, the cost approximation straightforwardly motivates increasing the energy confinement time because of its definition

$$\tau_E \equiv \frac{W}{P_{loss}}, \tag{1.2}$$

where

$$W \equiv \frac{3}{2} \int dV p \tag{1.3}$$

is the total plasma stored energy and P_{loss} is the power lost from the plasma. If we hold p constant and increase τ_E, the power lost from the plasma decreases. This eases the power handling requirements on the divertor and plasma-facing components, one of the major engineering challenges in reactor design. Decreasing P_{loss} also minimizes the required heating power to maintain a steady-state plasma. This means that less of the fusion power is needed for plasma heating. In other words, the plant is able to sell a higher fraction of the electricity it generates. This section will attempt to show how plasma rotation, driven by up-down asymmetry, can allow reactors to operate at both higher plasma beta and confinement times.

1.1.2 Benefits of vertical elongation

To preface the arguments of this thesis we will demonstrate the benefits of traditional vertical elongation relative to circular flux surfaces. To this end we will attempt to show that, at constant reactor cost, vertical elongation enables the production of

more fusion power and hence better economics. In this analysis we will assume that the reactor volume and the magnitude of the toroidal magnetic field dominate cost. Therefore, we can consider cost approximately fixed by fixing R_0, B_0, and the total plasma volume $V = (2\pi R_0)(\pi a^2 \kappa)$.

We start with an expression for the 50-50 deuterium-tritium volumetric fusion power density

$$p_f = \frac{n_e^2}{4}\langle \sigma v \rangle_{DT} Q_{DT} \tag{1.4}$$

where n_e is the electron density, Q_{DT} is the total energy yield per fusion reaction, and $\langle \sigma v \rangle_{DT}$ is the DT reaction rate constant, which only depends on ion temperature. In the temperature range of interest to fusion, $T_i \in [5, 20]$ keV, the rate constant can be approximated to within 10% as $\langle \sigma v \rangle_{DT} \approx c_{\sigma v} T_i^2$, where $c_{\sigma v}$ is some constant of proportionality [6]. This means that the fusion power density is roughly proportional to p^2, where the thermal pressure is $p \equiv \sum_s n_s T_s = 2 n_e T_e$, which is constrained by the Troyon limit.

The Troyon limit [7] is an estimate of the maximum β_T possible in a tokamak. Increasing β_T is a vital for power plants because it means more plasma pressure can be confined with the same magnetic field. When the beta limit is exceeded the plasma kinks and contacts the wall, which quenches the plasma and can damage the surrounding reactor components. The Troyon limit is given by the normalized plasma beta,

$$\beta_N \equiv \frac{(a/\mathrm{m})\,(B_0/\mathrm{T})}{(I_p/\mathrm{MA})}\beta_T \lesssim 0.03, \tag{1.5}$$

where I_p is the plasma current. Importantly, the Troyon limit is only appropriate in the absence of any conducting medium, such as a vacuum vessel, surrounding the plasma. The value of 0.03 is not a universal constant and depends on geometry parameters such as elongation. However, it is a good estimate that has been extensively verified for tokamaks with circular and vertically elongated poloidal cross-sections [8]. Throughout this work, it is assumed that the Troyon limit is also valid for tilted

elongation, though this has never been shown.

Using the Troyon limit, we find that the plasma current directly constrains the pressure, which motivates increasing the plasma current. However, increasing the plasma current to arbitrarily high values leads to violent disruptions that quench the plasma and potentially destroy the machine. For vertically elongated flux surfaces, in addition to the Troyon limit, the edge safety factor, q_a, needs to be

$$q_a \gtrsim 2.2 \tag{1.6}$$

to avoid major disruptions. Throughout this work, we will also assume this limit applies to tilted elongation. To calculate q_a we need to use an approximate form of the safety factor, $q_a \approx \frac{L_p}{L_\zeta}\frac{B_0}{B_p}$, and Ampere's law, $B_p L_p \approx \mu_0 I_p$, where $L_\zeta = 2\pi R_0$ is the toroidal circumference and $L_p \approx 2\pi a\sqrt{\frac{1}{2}\left(1+\kappa^2\right)}$ is the poloidal circumference. Eliminating a using V, we arrive at

$$\frac{5}{4\pi^2}\frac{VB_0}{I_p R_0^2}\frac{1+\kappa^2}{\kappa} \gtrsim 2.2\frac{m-T}{MA}. \tag{1.7}$$

This condition shows that increasing elongation permits more plasma current to be driven without disruptions. This, in turn, allows more plasma pressure to be confined, creating higher fusion power densities. Combining eqs. (1.4), (1.5), and (1.7) we find the total Troyon-limited fusion power is

$$P_f \lesssim \frac{1}{8}\left(\frac{0.03}{2.2}\right)^2\left(\frac{5}{4\pi^2}\right)^2\pi^2 c_{\sigma v} Q_{DT}\left(\frac{B_0^2}{2\mu_0}\right)^2\frac{V^2}{R_0^3}\frac{\left(1+\kappa^2\right)^2}{\kappa}. \tag{1.8}$$

We see that fusion power scales as κ^3 at constant R_0, B_0, and V. There are subtleties associated with our choice of constants. For example, we have entirely ignored the effects of elongation on turbulence and confinement time. However we will only argue that the κ^3 scaling is strong enough to merit ignoring these complications and delay more detailed discussion until Chapter 4. In summary, vertically elongated flux surfaces are preferable to circular because it allows more fusion power generation at constant reactor cost. Also, in this calculation we see how critical the Troyon and

major disruption limits are in determining the economic viability a tokamak.

1.1.3 Value of rotation

Due to the symmetry of a tokamak, the plasma flow, to lowest order in $\rho_* \equiv \rho_i/a$, is constrained to be purely toroidal [9, 10]. This toroidal rotation has proven to be beneficial in both reducing turbulence and improving MHD stability.

Turbulence suppression by rotation shear

Turbulence is characterized by fluctuations in electrostatic potential, plasma density, plasma temperature, and magnetic field. These fluctuations are able to transport particles, momentum, and energy by causing an $\vec{E} \times \vec{B}$ drift as well as modifying the background magnetic field to bridge flux surfaces. The size and strength of the turbulent eddies observed in typical tokamaks is sufficient to dominate over other transport mechanisms. Turbulence currently determines the confinement time of devices, making it a major topic of research and a fundamental problem in plasma physics. It has resisted the efforts of many, proving elusive to diagnose, expensive to simulate, and tortuous to treat analytically. Within the last 10 years however, through the use of nonlinear gyrokinetic simulations, the community has begun to grasp the turbulent transport of energy [11, 12] and particles [13]. Only recently, has significant effort been focused on turbulent momentum transport [14].

One of the most promising strategies to reduce turbulent energy transport and increase energy confinement time relies on velocity shear. Experiments [15, 16] and theory [17, 18, 19, 20] show that plasmas with a gradient in toroidal velocity u_ζ, also known as toroidal velocity shear, can exhibit a significant reduction in turbulence.

The competition of dissipative mechanisms (collisions, etc.) with turbulent drive from background gradients sets a natural size for turbulent eddies, referred to as the correlation length l_{corr}. At distances longer than a correlation length, dissipative mechanisms are able to randomize and destroy information, which prevents any correlated structures from existing. Since turbulent transport in a tokamak can be

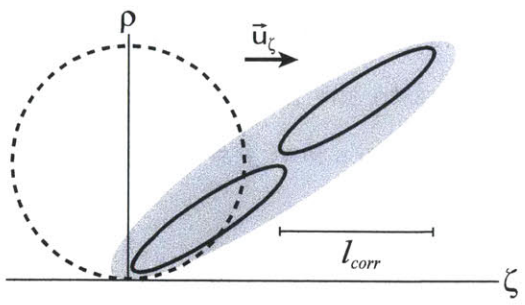

Figure 1-2: A cartoon showing a turbulent eddy with (solid) and without (dotted) the effects of flow shear of the form $u_\zeta(\rho) = \gamma_E \rho$ (figure adapted from [21]).

understood as a diffusive process with the correlation length, l_{corr}, as the characteristic step size, we expect transport to increase with l_{corr}. A gradient in the fluid velocity will stretch, deform, and ultimately break up turbulent eddies, as shown in fig. 1-2. This leads to less cross-field energy transport and higher confinement times.

Relaxation of the Troyon limit

Additionally, toroidal velocity has been shown to stabilize MHD modes. In particular, in the presence of a resistive vacuum vessel, rotation can stabilize the ideal kink and resistive tearing instabilities. These modes are the reason for the Troyon limit (see eq. (1.5)). The mechanism by which rotation stabilizes MHD modes can be understood intuitively, by investigating how the magnetic field interacts with the vacuum vessel as the instability grows.

If a perfectly conducting vacuum vessel surrounds the plasma, the external kink mode, which leads to the Troyon limit, can be stabilized. This is because the magnetic field cannot diffuse through the wall and instead is compressed by any instability, providing stabilizing magnetic pressure. A resistive vacuum vessel does not completely trap the magnetic field, but can still allow the Troyon limit to be relaxed considerably. The resistive wall mode is constrained to grow no faster than

$$\tau_w \equiv \frac{\int dV B}{\int d\vec{S} \cdot \vec{\Gamma}_B}, \tag{1.9}$$

the magnetic field confinement time or the characteristic magnetic field vacuum vessel diffusion time. Here $\vec{\Gamma}_B$ refers to the flux of magnetic field. We can estimate this resistive time by substituting Ohm's law, $\vec{j} = \sigma_w \vec{E}$, into Ampere's law (ignoring the displacement current) to get

$$\vec{\nabla} \times \vec{B} = \mu_w \sigma_w \vec{E}, \tag{1.10}$$

where the vacuum vessel has magnetic permeability μ_w and conductivity σ_w. Then we take the curl and substitute Faraday's equation to give

$$\frac{\partial \vec{B}}{\partial t} = \frac{1}{\mu_w \sigma_w} \frac{\partial^2 \vec{B}}{\partial r^2} \tag{1.11}$$

in slab geometry. This is a diffusion equation with a diffusion constant of $D_w = \frac{1}{\mu_w \sigma_w}$. Now we can calculate the outwards radial magnetic flux to be $\Gamma_B \sim D_w \frac{\partial B}{\partial r} \sim D_w \frac{B}{d_w}$, where d_w is the wall thickness. This means that, with $\int d\vec{S} \cdot \vec{\Gamma}_B \sim 2\pi R_0 2\pi a_w \Gamma_B$ and $\int dV B \sim 2\pi R_0 \pi a_w^2 B$, we arrive at

$$\tau_w \sim \frac{1}{2} a_w \mu_w \sigma_w d_w, \tag{1.12}$$

in agreement with refs. [22] and [23].

If τ_w is longer than the duration of the plasma shot t_{shot}, the magnetic field will compress against the chamber wall and stabilize the plasma. Unfortunately, reactors are expected to have shots that last days, if not months. Moreover designing a vacuum vessel that can survive and function in a reactor environment is already at the limits of feasibility. Requiring that it also be highly conducting is likely insurmountable. For comparison, the DIII-D tokamak vacuum vessel has a resistive time of only $\tau_w \sim 5$ ms [24]. However, if the plasma is rotating fast enough and the instability rotates with it, the situation is dramatically changed. As the perturbation rotates, the magnetic field constantly has to diffuse through a new area of the vessel (see fig. 1-3). Then, the magnetic diffusion time τ_w must only be long compared to the rotation frequency $\Omega_\zeta \tau_w \gg 1$, where $\Omega_\zeta \equiv u_\zeta / R$ and u_ζ is the plasma toroidal fluid velocity. In other

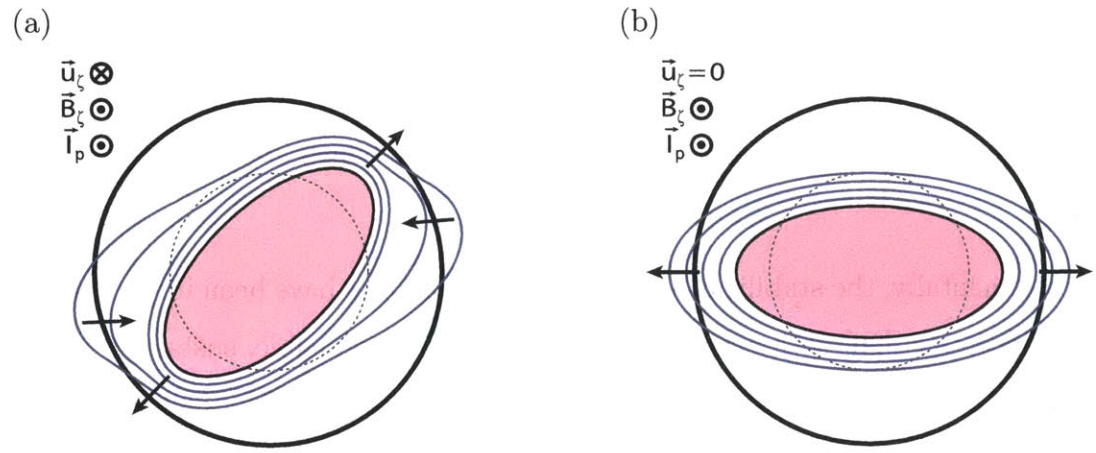

Figure 1-3: A cartoon of the poloidal cross-section of a tokamak plasma (pink) with an $m = 2$, $n = 1$ external kink mode (a) with and (b) without toroidal rotation. The equilibrium plasma shape (dotted, gray), the vacuum vessel (thick, black), magnetic surfaces (blue), and the velocity of points on the magnetic surfaces (arrows) are indicated.

words, plasma rotation begins to allow violation of the Troyon limit when $u_\zeta \gg \frac{R_0}{a_w} \frac{2}{\mu_w \sigma_w d_w}$.

This intuitive picture is too simple to capture the many subtleties and complications that arise in reality. The condition that $\Omega_\zeta \tau_w \gg 1$ is necessary, but not sufficient for complete stabilization. When this condition is satisfied resistive tearing modes are stabilized [22, 25], but ideal modes may not be [26]. Ideal modes are significantly more difficult to deal with. If an ideal instability is stable with a perfectly conducting wall, but unstable without any wall, the presence of a resistive wall will cause it to split into two modes. One is an external kink that can be stabilized with rotation because it moves with the plasma. The other is stationary, grows at the τ_w timescale, and is labeled a "resistive wall" mode [23]. Early investigation using simple cylindrical models concluded that rotation speeds less than the Alfven speed are unable to stabilize the resistive wall mode [27]. Recent, sophisticated models [28, 29] include effects such as such as finite aspect ratio, finite pressure, and trapped particle compressibility, which serve to increase plasma dissipation. They arrive at the more optimistic conclusion that slow plasma rotation, just a fraction of the sound speed, can fully suppress the resistive wall mode. However, this stabilization appears to be

fairly nuanced and depends on the specific model used. Stabilization may only occur when the wall is positioned within a particular range of distances from the plasma and there may be a maximum value of rotation above which stability is impossible [30, 31].

Experimentally, the stabilization of resistive wall modes have been investigated on DIII-D since 1995 [26] with ever improving results. Reproducible, sustained plasmas have been created that exceed the Troyon limit by a factor of two [32]. Other machines, such as NSTX [33] and TEXTOR [34], have observed similar behavior. Even a cross-machine comparison has been performed to determine scalings of the critical level of rotation required for stabilization [24]. These robust experimental results provide evidence that the nuanced conclusions obtained theoretically may be a consequence of the simplified models used. It seems that, with the abundance of dissipative mechanisms present in experiments, there is a broad stability window requiring only modest rotation.

1.1.4 Value of intrinsic rotation

Toroidal rotation can be generated in a number of ways. Neutral particle beams are frequently used to heat the plasma, but can also generate rotation if injected toroidally [35]. Similarly lower hybrid waves, primarily used to noninductively drive current, can induce rotation. Both of these methods represent an external injection of momentum, however they do not scale well to large devices. There is concern in the community that the external momentum injection on ITER will not induce enough rotation to stabilize the resistive wall mode. The situation in a future power plant would be even worse. An alternative is intrinsic rotation, which refers to rotation that is observed in the absence of external injection of momentum. This rotation comes for free, but it is poorly understood and experimental measurements reveal it to be rather small, generally less than a tenth of the plasma sound speed [36].

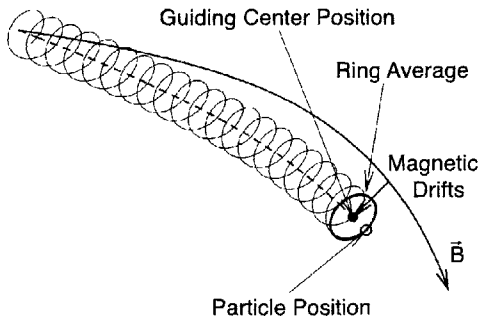

Figure 1-4: The ring average in gyrokinetics (figure adapted from ref. [37]).

1.2 Up-down asymmetry

Up-down asymmetry is essential to achieving fast rotation because, as will be discussed in Section 1.2.2, up-down symmetric tokamaks without external momentum injection are constrained to have no rotation to lowest order in ρ_*. Otherwise we might expect sonic rotation profiles that vary on the same scale as temperature profiles. To understand this constraint we first need to introduce gyrokinetics, the model for turbulent fluctuations.

1.2.1 Gyrokinetics

Gyrokinetics [38, 39, 40, 41] is a theoretical framework to study plasma behavior on perpendicular spatial scales comparable to the gyroradius ($k_\perp \rho_i \sim 1$) and timescales much slower than the particle cyclotron frequencies ($\omega \ll \Omega_i \ll \Omega_e$). These particular scales have been experimentally shown to be appropriate for modeling turbulence [42]. Fundamentally, the gyrokinetic model assumes the plasma is strongly magnetized ($\rho_i/l_p = \rho_* \ll 1$, where l_p is the characteristic size of the plasma) and the behavior of interest has low frequencies ($\omega \ll \Omega_i$). Also, we must expand the distribution function, $f_s = f_{s0} + f_{s1} + \ldots$, and assume the perturbation is small compared to the background ($f_{s1} \ll f_{s0}$) [37]. For tokamak plasmas, poloidal and toroidal periodicity of particle orbits requires the lowest order distribution function to be a Maxwellian

($f_{s0} = F_{Ms}$). Here

$$F_{Ms} \equiv n_s \left(\frac{m_s}{2\pi T_s}\right)^{3/2} \exp\left(-\frac{m_s\left(\vec{v}-\vec{u}_s\right)^2}{2T_s}\right) \tag{1.13}$$

is the Maxwellian distribution function, n_s and T_s are the density and temperature of species s, and m_s is the particle mass. In this thesis, we are interested in the momentum redistribution that occurs in an initially stationary plasma. Consequently, we will take $\vec{u}_s$, the mean plasma flow, to be small in order to determine the momentum flux in the absence of rotation.

We will start with the electrostatic Fokker-Plank equation,

$$\frac{\partial f_s}{\partial t} + \vec{v}\cdot\vec{\nabla} f_s + \frac{Z_s e}{m_s}\left(-\vec{\nabla}\phi + \frac{\vec{v}\times\vec{B}}{c}\right)\cdot\vec{\nabla}_v f_s = \sum_{s'} C_{ss'}, \tag{1.14}$$

and quasineutrality equation,

$$\sum_s Z_s \int d^3v f_s = 0, \tag{1.15}$$

written assuming weak electromagnetic effects and background potential. Here Z_s is the charge number, e is the charge of the proton, ϕ is the scalar electric potential, c is the speed of light, and $\sum_{s'} C_{ss'}$ is the collision operator. Both equations can both be expanded order by order in ρ_* and simplified. In doing so, we change real-space coordinates to the guiding center position

$$\vec{R}_{gc} \equiv \vec{r}_p + \frac{\vec{w}\times\hat{b}}{\Omega_s}, \tag{1.16}$$

specified by the poloidal flux, ψ, a poloidal angle, θ, and

$$\alpha \equiv \zeta - I(\psi)\int_0^\theta\Big|_\psi d\theta'\left(R^2\vec{B}\cdot\vec{\nabla}\theta\right)^{-1}, \tag{1.17}$$

which parameterizes the direction perpendicular to the magnetic field line, but still within the flux surface. We also change velocity-space coordinates to the parallel

velocity, $w_{||}$, the magnetic moment, $\mu \equiv \frac{m_s w_\perp^2}{2B}$, and the gyrophase angle,

$$\varphi \equiv \arctan\left(\frac{\left(\vec{w}\times\hat{b}\right)\cdot\vec{\nabla}\psi}{\vec{w}\cdot\vec{\nabla}\psi}\right). \tag{1.18}$$

Here $\vec{w} = \vec{v} - \vec{u}_s$ is the particle velocity in the frame rotating with the plasma, but since we have taken $\vec{u}_s = 0$, $\vec{w}$ is the same as $\vec{v}$. We make use of the substitution

$$\bar{h}_s\left(\vec{R}_{gc}, w_{||}, \mu, t\right) \equiv f_{s1} + \frac{Z_s e\phi}{T_s} F_{Ms} \tag{1.19}$$

and average over the gyrophase angle. Instead of gyrating charged particles, our equations now govern the evolution of charged rings with a guiding position (see fig. 1-4). Because of the strong anisotropy introduced by the magnetic field, the perpendicular scale of the turbulence is much smaller than the parallel variation. Furthermore, two of our previous assumptions, $k_\perp \rho_i \sim 1$ and $\rho_i \ll l_p$, show that the perpendicular turbulence length scale is smaller than any background radial gradients, allowing us to Fourier analyze using

$$\bar{h}_s = \sum_{k_\psi, k_\alpha} h_s\left(k_\psi, k_\alpha\right) \exp\left(ik_\psi\psi + ik_\alpha\alpha\right). \tag{1.20}$$

This produces the Fourier-analyzed gyrokinetic equation in μ and $w_{||}$ velocity variables, [1],

$$\begin{aligned}
&\frac{\partial h_s}{\partial t} + w_{||}\hat{b}\cdot\vec{\nabla}\theta\left.\frac{\partial h_s}{\partial\theta}\right|_{w_{||},\mu} + i\left(k_\psi v_{ds\psi} + k_\alpha v_{ds\alpha}\right)h_s \\
&\quad + a_{s||}\left.\frac{\partial h_s}{\partial w_{||}}\right|_{\theta,\mu} - \sum_{s'}\langle C_{ss'}^{(l)}\rangle_\varphi + \left\{\langle\phi\rangle_\varphi, h_s\right\} \\
&\quad = \frac{Z_s e F_{Ms}}{T_s}\frac{\partial\langle\phi\rangle_\varphi}{\partial t} - v_{\phi s\psi}F_{Ms}\left[\frac{1}{n_s}\frac{\partial n_s}{\partial\psi} + \left(\frac{m_s w^2}{2T_s} - \frac{3}{2}\right)\frac{1}{T_s}\frac{\partial T_s}{\partial\psi}\right],
\end{aligned} \tag{1.21}$$

and the Fourier-analyzed quasineutrality equation,

$$\sum_s 2\pi Z_s B \int dw_{||} \int d\mu J_0 \left(\frac{k_\perp \sqrt{2\mu B}}{\Omega_s} \right) h_s = \sum_s \frac{Z_s^2 e n_s}{T_s} \phi, \tag{1.22}$$

where $J_0(\ldots)$ is the zeroth order Bessel function of the first kind. The guiding center particle drift velocity

$$\vec{v}_{ds} = \frac{\mu}{\Omega_s} \hat{b} \times \vec{\nabla} B + \frac{w_{||}}{\Omega_s} \hat{b} \times \left(\hat{b} \cdot \vec{\nabla} \hat{b} \right) \tag{1.23}$$

is split up into

$$v_{ds\psi} \equiv \vec{v}_{ds} \cdot \vec{\nabla} \psi = - \frac{I \left(w_{||}^2 + \mu B \right)}{\Omega_s B} \hat{b} \cdot \vec{\nabla} \theta \frac{\partial B}{\partial \theta} \tag{1.24}$$

and

$$v_{ds\alpha} \equiv \vec{v}_{ds} \cdot \vec{\nabla} \alpha = - \frac{w_{||}^2 + \mu B}{\Omega_s} \left[\frac{\partial B}{\partial \psi} - \frac{\partial B}{\partial \theta} \frac{\hat{b} \cdot \left(\vec{\nabla} \theta \times \vec{\nabla} \alpha \right)}{B} \right] - \frac{4\pi w_{||}^2}{B \Omega_s} \frac{\partial p}{\partial \psi}. \tag{1.25}$$

The acceleration parallel to the magnetic field line is given by

$$a_{s||} = -\mu \left(\hat{b} \cdot \vec{\nabla} \theta \right) \frac{\partial B}{\partial \theta}, \tag{1.26}$$

$\langle \cdots \rangle_\varphi$ denotes an average over the gyromotion holding $\vec{R}_{gc}$ fixed. Importantly,

$$\{ \langle \phi \rangle_\varphi, h_s \} \equiv c \sum_{k'_\psi, k'_\alpha} \left(k'_\psi k_\alpha - k_\psi k'_\alpha \right) \langle \phi \rangle_\varphi \left(k'_\psi, k'_\alpha \right) h_s \left(k_\psi - k'_\psi, k_\alpha - k'_\alpha \right) \tag{1.27}$$

is the nonlinear term that represents the $\vec{E} \times \vec{B}$ motion of the fluctuations, where

$$\langle \phi \rangle_\varphi = J_0 \left(\frac{k_\perp \sqrt{2\mu B}}{\Omega_s} \right) \phi \tag{1.28}$$

is the gyroaveraged potential and the perpendicular wavenumber can be written as

$$k_\perp = \sqrt{k_\psi^2 \left|\vec{\nabla}\psi\right|^2 + 2k_\psi k_\alpha \vec{\nabla}\psi \cdot \vec{\nabla}\alpha + k_\alpha^2 \left|\vec{\nabla}\alpha\right|^2}. \tag{1.29}$$

Finally,

$$v_{\phi s\psi} \equiv ik_\alpha c\langle\phi\rangle_\varphi \tag{1.30}$$

is the turbulent $\vec{E}\times\vec{B}$ drift normal to the flux surface.

Solving the gyrokinetic and quasineutrality equations, given in eqs. (1.21) and (1.22), for h_s and ϕ allows us to calculate the turbulent fluxes of particles, momentum, and energy given by

$$\Gamma_{tot} = \sum_s \sum_{k_\psi,k_\alpha} \left\langle \int \left(\vec{v}_\phi \cdot \vec{\nabla}\psi\right) h_s \left(k_\phi, k_\alpha, \psi, \theta, \zeta, w_{||}, \mu\right) d^3v \right\rangle_\psi, \tag{1.31}$$

$$\Pi_{\zeta tot} = \sum_s \sum_{k_\psi,k_\alpha} \left\langle Rm_s \int \vec{w}\cdot\hat{e}_\zeta \left(\vec{v}_\phi \cdot \vec{\nabla}\psi\right) h_s \left(k_\phi, k_\alpha, \psi, \theta, \zeta, w_{||}, \mu\right) d^3v \right\rangle_\psi, \tag{1.32}$$

$$Q_{tot} = \sum_s \sum_{k_\psi,k_\alpha} \left\langle \frac{m_s}{2} \int w^2 \left(\vec{v}_\phi \cdot \vec{\nabla}\psi\right) h_s \left(k_\phi, k_\alpha, \psi, \theta, \zeta, w_{||}, \mu\right) d^3v \right\rangle_\psi \tag{1.33}$$

respectively, where $\langle\ldots\rangle_\psi \equiv \left(\frac{dV}{d\psi}\right)^{-1} \int_0^{2\pi} d\theta \int_0^{2\pi} d\zeta \frac{(\ldots)}{|\vec{B}\cdot\vec{\nabla}\theta|}$ denotes the flux surface average and $\vec{v}_\phi \equiv -\frac{i\vec{k}\phi\times\vec{B}}{B^2}$ is the Fourier transformed turbulent $\vec{E}\times\vec{B}$ velocity evaluated at $-k_\psi$ and $-k_\alpha$. The momentum flux tells us how strongly a particular tokamak configuration will redistribute momentum to create nonzero rotation from an initially stationary plasma.

1.2.2 Symmetry argument

In 2011, Parra *et al.* [1] and Sugama *et al.* [43] demonstrated a symmetry in the gyrokinetic equation for up-down symmetric tokamaks that has important consequences for momentum transport. Under the $\left(k_\psi, k_\alpha, \theta, w_{||}, \mu\right) \to \left(-k_\psi, k_\alpha, -\theta, -w_{||}, \mu\right)$ coordinate system transformation, the gyrokinetic equation (see eq. (1.21)) is odd. This

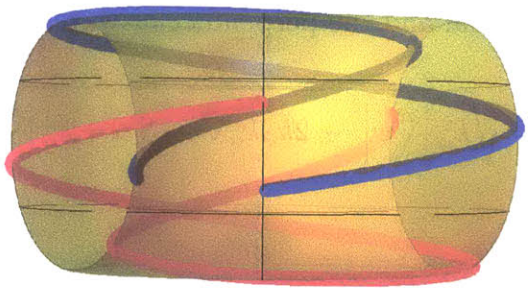

Figure 1-5: An up-down symmetric tokamak with the trajectories of two particles (red, blue) traveling in opposite directions along magnetic field lines on the same flux surface (yellow).

proves that for any set of solutions $h_s\left(k_\psi, k_\alpha, \theta, w_{||}, \mu\right)$ and $\phi\left(k_\psi, k_\alpha, \theta\right)$, there exists another set of solutions $-h_s\left(-k_\psi, k_\alpha, -\theta, -w_{||}, \mu\right)$ and $-\phi\left(-k_\psi, k_\alpha, -\theta\right)$. However, each of these solution sets is only valid for a particular initial condition. To determine the contribution of these solutions to the flux of toroidal angular momentum, we can inspect eq. (1.32). In addition to $w_{||} \rightarrow -w_{||}$ and $h_s \rightarrow -h_s$, under the transformation $\vec{v}_\phi \rightarrow -\vec{v}_\phi$, since ϕ changes sign. Therefore, the second solution, $-h_s\left(-k_\psi, k_\alpha, -\theta, -w_{||}, \mu\right)$ and $-\phi\left(-k_\psi, k_\alpha, -\theta\right)$, generates a momentum flux which exactly cancels the flux from the original solution, $h_s\left(k_\psi, k_\alpha, \theta, w_{||}, \mu\right)$ and $\phi\left(k_\psi, k_\alpha, \theta\right)$. Because the tokamak turbulence is chaotic, after a sufficiently long time (called the turbulent decorrelation time), the system samples all possible initial conditions. Hence, eventually, both solutions will arise and cancel any net momentum flux. As a result, this symmetry implies a vanishing time-averaged momentum transport.

Intuitively, we can understand this using fig. 1-5. For every blue particle traveling in one direction along a field line, there is a red particle traveling in the opposite direction along its mirror symmetric field line that exactly cancels any contribution the blue particle may have to the overall flux surface momentum flux. The two particles do not necessarily travel synchronously, but will cause canceling momentum fluxes within a turbulent decorrelation time.

Symmetry breaking mechanisms

To lowest order in ρ_*, there are three mechanisms that can break this symmetry of the gyrokinetic equation [44]. First, significant preexisting average parallel velocity

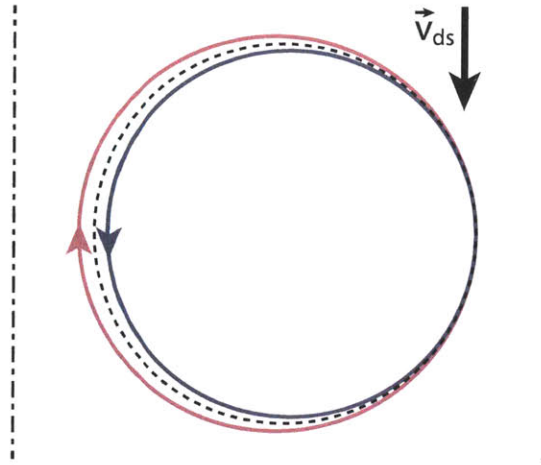

Figure 1-6: Particles traveling in opposite directions along a magnetic field line drift in opposite directions due to magnetic drifts $\vec{v}_{ds}$.

invalidates the argument because there would be a different number of particles traveling in each direction, so some would not have a canceling pair. Second, the presence of large rotation shear changes the nature of the turbulence in the inner versus the outer side of the flux surface of interest. This means that particles drifting off the flux surface in opposing radial directions (as the blue and red particles do in fig. 1-5 due to magnetic drifts) will see different turbulence and their paths will be affected asymmetrically. Third, up-down asymmetry in the tokamak will mean that, for example, the red and blue particles in fig. 1-7 experience the magnetic field topology and, hence, turbulent fluctuations in a different order as they travel in opposing directions. There are also higher order effects in ρ_* like diamagnetic flows, poloidal variation of turbulence, and radial profile variation that break the symmetry [45]. However, the exclusive focus of this work will be the consequences of up-down asymmetry.

1.2.3 Previous work

The most relevant research into intrinsic rotation in up-down asymmetric devices was published in 2009 by Camenen *et al.* [2, 46]. It investigates the turbulent momentum flux distribution in a diverted plasma geometry using a quasilinear local turbulent gyrokinetic code, GKW [47], to simulate a global equilibrium generated with the

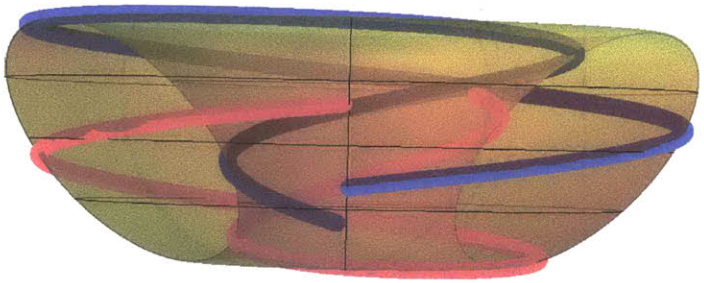

Figure 1-7: An up-down asymmetric tokamak with the trajectories of two particles (red, blue) traveling in opposite directions along magnetic field lines on the same flux surface (yellow).

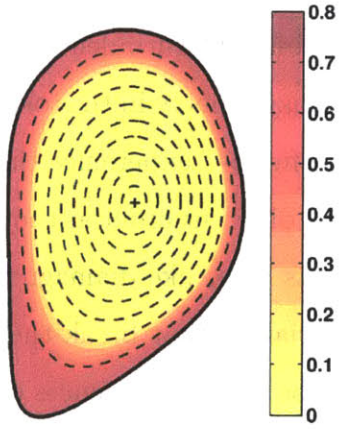

Figure 1-8: A quasilinear estimate of the maximum sustainable value of $-\frac{R^2}{v_{thi}}\frac{\partial \Omega_\zeta}{\partial r}$. The dashed lines indicate the flux surfaces labeled by $\rho = 0.1$ to 0.9, with steps of 0.1. Positive values indicate a radial outward flux of momentum in the direction of $\vec{B}$ (figure from ref. [2]).

Grad-Shafranov code CHEASE [48]. As expected, we see in fig. 1-8 that the more asymmetric flux surfaces, located near the edge, are able to support a larger gradient in rotation. This work will use nonlinear simulations to produce better estimates of rotation and look at a wider range of geometries to achieve the highest levels of rotation possible.

Chapter 2

Up-down asymmetric MHD equilibrium

Since we are ultimately interested in achieving high levels of intrinsic rotation in fusion devices, we should start by identifying practical up-down asymmetric configurations. To do this, we will use the ideal MHD model [49] to find stable geometries that maximize up-down asymmetry. Since external Poloidal Field (PF) coils set the shape of the outermost closed flux surface, it is a free parameter. However, we must determine if up-down asymmetry introduced at the edge effectively propagates through the plasma to the magnetic axis.

2.1 Radial penetration of up-down asymmetry

To determine how the flux surface shape changes within the tokamak, we begin by writing the Grad-Shafranov equation

$$R^2\vec{\nabla}\cdot\left(\frac{\vec{\nabla}\psi}{R^2}\right) = -\mu_0 R^2\frac{dp}{d\psi} - \frac{1}{2}\frac{d}{d\psi}\left(I^2\right), \tag{2.1}$$

where $I \equiv RB_\zeta$ and p are free flux functions to be specified in this calculation. We note that $\vec{B} = I\vec{\nabla}\zeta + \vec{B}_p$, where $\vec{B}_p = \vec{\nabla}\zeta\times\vec{\nabla}\psi$ is the poloidal magnetic field. Though there has been much work on general analytic solutions to the Grad-Shafranov equation

[50], we will only need approximate solutions to several specific cases to develop our intuition. Thus, we take the orderings in the inverse aspect ratio, $\epsilon \equiv \frac{a}{R_0} \ll 1$, typical for an ohmically heated tokamak [51]

$$\frac{B_p}{B_\zeta} \sim \epsilon, \quad \frac{2\mu_0 p}{B_\zeta} \sim \epsilon^2. \tag{2.2}$$

Next we must expand $\psi = \psi_0 + \psi_1 + \ldots$, $I = I_0 + I_1 + I_2 + I_3 + \ldots$, and $p = p_2 + p_3 + \ldots$, where each subscript indicates the quantity's order in ϵ. We also let $\psi_0 \sim aR_0B_p$ and $R = R_0 + R_1$, where $R_1 = r\cos(\theta)$ and θ is measured from the outboard midplane. Consequently, to $O(\epsilon^{-1}B_0)$, eq. (2.1) becomes

$$-\frac{d}{d\psi_0}(I_0 I_1) = 0. \tag{2.3}$$

Because $I_0 = R_0B_0$, this shows that I_1 is a constant. We are free to absorb it into I_0 and set $I_1 = 0$. Using this fact, the $O(B_0)$ Grad-Shafranov equation is

$$\frac{1}{r}\frac{\partial}{\partial r}\left(r\frac{\partial \psi_0}{\partial r}\right) + \frac{1}{r^2}\frac{\partial^2 \psi_0}{\partial \theta^2} = -\mu_0 R_0^2 \frac{dp_2}{d\psi_0} - I_0 \frac{dI_2}{d\psi_0} \tag{2.4}$$

and the $O(\epsilon B_0)$ Grad-Shafranov equation is

$$\frac{1}{r}\frac{\partial}{\partial r}\left(r\frac{\partial \psi_1}{\partial r}\right) + \frac{1}{r^2}\frac{\partial^2 \psi_1}{\partial \theta^2} = \psi_1 \frac{d^2}{d\psi_0^2}\left(-\mu_0 R_0^2 p_2 - I_0 I_2\right) - 2\mu_0 R_0 R_1 \frac{dp_2}{d\psi_0} + \frac{1}{R_0}\vec{\nabla} R_1 \cdot \vec{\nabla}\psi_0. \tag{2.5}$$

We note that the absence of a factor of 2 in the numerator of the last term is a consequence of the R contained within the cylindrical divergence.

2.1.1 Solutions to the $O(B_0)$ Grad-Shafranov equation

The homogeneous portion of eq. (2.4) is solved by cylindrical harmonics. Furthermore, since p and I are free parameters, we can choose them to get simple forms for the inhomogeneous part and still illuminate the physics of the problem. Using Ampere's law and $\vec{B} = I\vec{\nabla}\zeta + \vec{\nabla}\zeta \times \vec{\nabla}\psi$, one can show that the right side

$-\mu_0 R^2 \frac{dp}{d\psi} - \frac{1}{2}\frac{d}{d\psi}(I^2) = \mu_0 j_\zeta R$ is related to the toroidal current. So we will choose to study a constant toroidal current profile $\mu_0 j_\zeta R_0 = A$, a linear hollow profile $\mu_0 j_\zeta R_0 = A_h + A'_h \psi_0$, and a linear peaked profile $\mu_0 j_\zeta R_0 = A_c - A'_c \psi_0$, where A, A_h, A'_h, A_c, and A'_c are positive constants of our choosing (see fig. 2-1). Then, eq. (2.4) becomes

$$\frac{1}{r}\frac{\partial}{\partial r}\left(r\frac{\partial \psi_0}{\partial r}\right) + \frac{1}{r^2}\frac{\partial^2 \psi_0}{\partial \theta^2} = A, \tag{2.6}$$

$$\frac{1}{r}\frac{\partial}{\partial r}\left(r\frac{\partial \psi_0}{\partial r}\right) + \frac{1}{r^2}\frac{\partial^2 \psi_0}{\partial \theta^2} = A_h + A'_h \psi_0, \tag{2.7}$$

$$\frac{1}{r}\frac{\partial}{\partial r}\left(r\frac{\partial \psi_0}{\partial r}\right) + \frac{1}{r^2}\frac{\partial^2 \psi_0}{\partial \theta^2} = A_c - A'_c \psi_0 \tag{2.8}$$

for each case respectively. These equations are solved by

$$\psi_0(r,\theta) = \frac{A}{4}r^2 + \sum_{m=0}^{\infty} r^m \left(C_m \cos(m\theta) + D_m \sin(m\theta)\right), \tag{2.9}$$

$$\psi_0(r,\theta) = \frac{A_h}{A'_h}\left(I_0\left(\sqrt{A'_h}r\right) - 1\right) + \sum_{m=0}^{\infty} I_m\left(\sqrt{A'_h}r\right)\left(C_{hm}\cos(m\theta) + D_{hm}\sin(m\theta)\right), \tag{2.10}$$

$$\psi_0(r,\theta) = -\frac{A_c}{A'_c}\left(J_0\left(\sqrt{A'_c}r\right) - 1\right) + \sum_{m=0}^{\infty} J_m\left(\sqrt{A'_c}r\right)\left(C_{cm}\cos(m\theta) + D_{cm}\sin(m\theta)\right), \tag{2.11}$$

respectively. Here m is the poloidal mode number, J_m is the m^{th} Bessel function of the first kind, I_m is the m^{th} modified Bessel function of the first kind. C_m, D_m, C_{hm}, D_{hm}, C_{cm}, and D_{cm} are Fourier harmonic coefficients determined by the boundary condition at the plasma edge.

From studying the plots in fig. 2-2 we can obtain the results of this calculation. First of all, the $m = 2$ mode roughly corresponds to plasma elongation, the $m = 3$ mode to triangularity, the $m = 4$ mode to squareness, and so on. Also, we observe that the flux surfaces near the magnetic axis in all the $m = 3$ cases are circular. This can be confirmed by taking the limit of eqs. (2.9), (2.10), and (2.11) as $r \to 0$. For example, the constant current case becomes $\frac{A}{4}r^2 + r^3\left(C_3\cos(3\theta) + D_3\sin(3\theta)\right) \to \frac{A}{4}r^2$, which

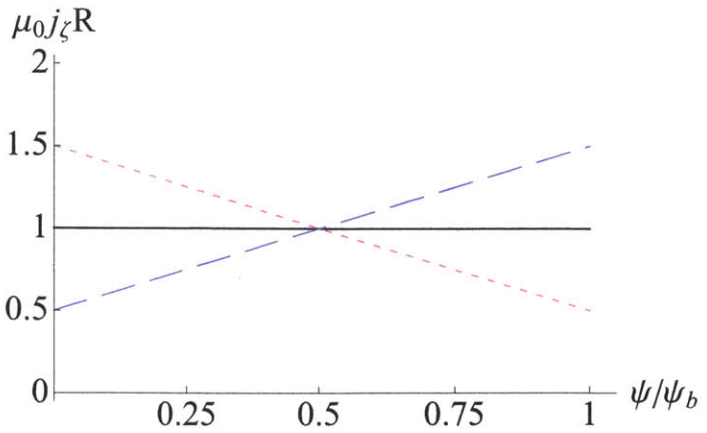

Figure 2-1: Normalized radial profiles of the plasma current used to produce the constant (black, solid), linear hollow (blue, dashed), and linear peaked (red, dotted) flux surface shapes.

has no dependence on θ. In these cases, the tokamak is only up-down asymmetric near the plasma edge. This effect only gets more pronounced with higher m modes. Therefore, if we want to make the tokamak as asymmetric as possible, we should use low m modes. However, for all three cases, the $m = 1$ mode does not introduce any asymmetry into the flux surface shape, it is purely a translation. This means the $m = 2$ mode, which introduces elongation, is the optimal choice.

For the constant current pure $m = 2$ mode case, one can use trigonometric identities and rearrange the solution

$$\psi_0(r,\theta) = \frac{A}{4}r^2 + r^2\left(C_2\cos(2\theta) + D_2\sin(2\theta)\right) \tag{2.12}$$

to show that the flux surfaces are exactly elliptical. Furthermore, one can translate the Fourier coefficients to the elongation,

$$\kappa(\psi_0) = \kappa_b \equiv \sqrt{\frac{\frac{A}{4} + \sqrt{C_2^2 + D_2^2}}{\frac{A}{4} - \sqrt{C_2^2 + D_2^2}}}, \tag{2.13}$$

the tilt angle of the elongation (see fig. 3-2a),

$$\theta_\kappa(\psi_0) = \theta_{\kappa b} \equiv -\frac{1}{2}\arctan\left(\frac{D_2}{C_2}\right), \tag{2.14}$$

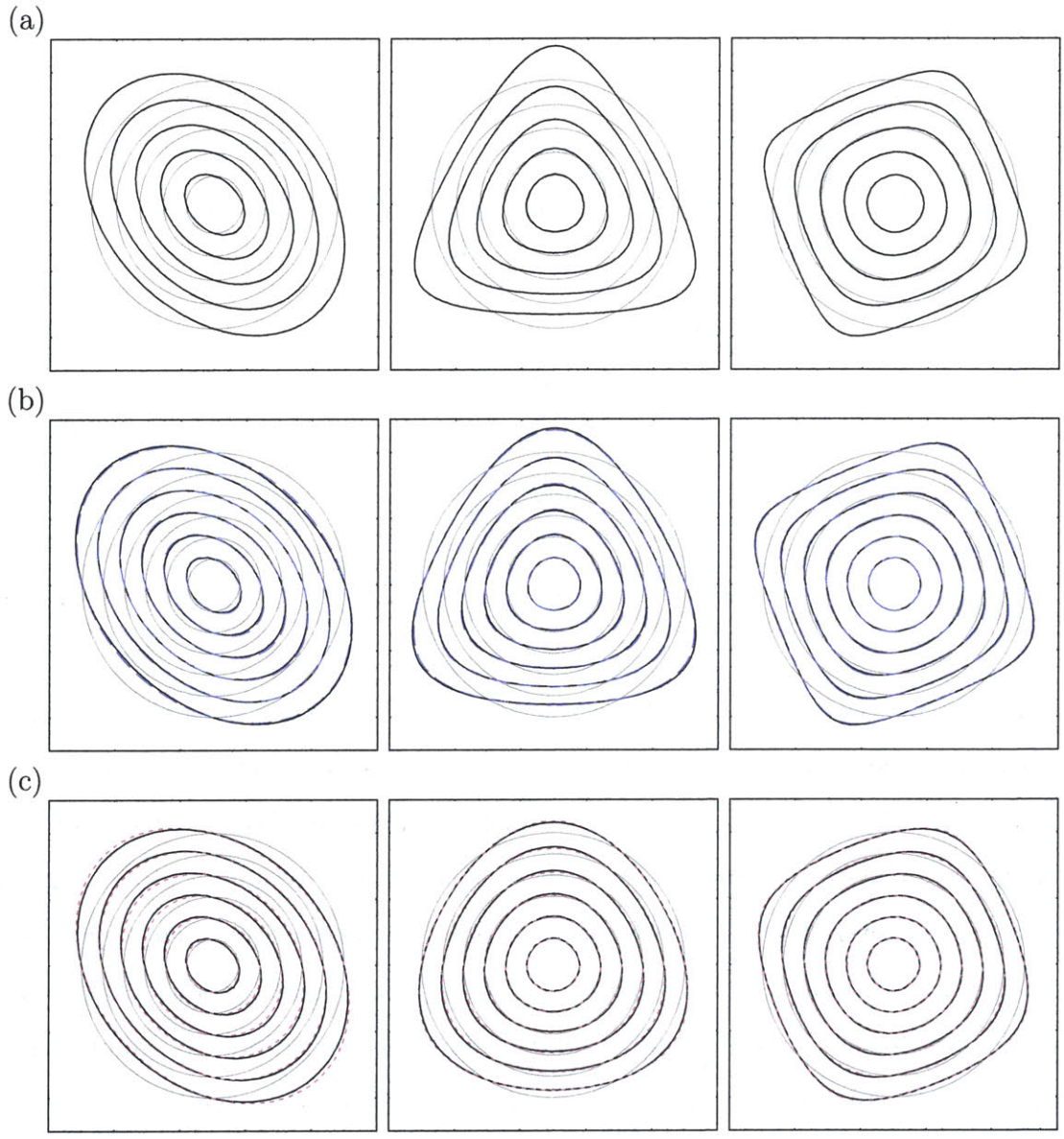

Figure 2-2: Example ψ_0 contours with pure $m = 2$, $m = 3$, and $m = 4$ outer boundary conditions respectively for the (a) constant (black, solid), (b) linear hollow (blue, dashed), and (c) linear peaked (red, dotted) current profiles shown in fig. 2-1. Circular (gray, solid) and constant current (black, solid) flux surfaces are shown for comparison.

and the minor radius of the flux surface,

$$r_\psi(\psi_0) \equiv a\rho(\psi_0) = \sqrt{\frac{\psi_0}{\frac{A}{4} + \sqrt{C_2^2 + D_2^2}}}. \tag{2.15}$$

It should be mentioned that the tilt angle of the ellipse, θ_κ, is defined to be a left-handed rotation with respect to $\hat{e}_\zeta$ (see fig. 3-2a), whereas $\hat{e}_\theta$ is in the right-handed direction (see fig. 1-1). These definitions give rise to the negative sign appearing in eq. (2.14). We can invert these relationships to find

$$\psi_0(r_\psi) = \frac{\mu_0 j_\zeta R_0}{2} \frac{\kappa_b^2}{\kappa_b^2 + 1} r_\psi^2, \tag{2.16}$$

$$A = \mu_0 j_\zeta R_0, \tag{2.17}$$

$$C_2 = \frac{\mu_0 j_\zeta R_0}{4} \frac{\kappa_b^2 - 1}{\kappa_b^2 + 1} \cos(2\theta_{\kappa b}), \tag{2.18}$$

$$D_2 = -\frac{\mu_0 j_\zeta R_0}{4} \frac{\kappa_b^2 - 1}{\kappa_b^2 + 1} \sin(2\theta_{\kappa b}). \tag{2.19}$$

Crucially, we see in eqs. (2.13) and (2.14) that the elongation and elongation tilt angle are independent of the radial coordinate. This means that, for a constant current profile, the elongation and elongation tilt at the plasma boundary, κ_b and $\theta_{\kappa b}$, will uniformly penetrate throughout the plasma. We can also numerically calculate elongation at different flux surfaces for the two other current distributions to produce fig. 2-3. The important trend to notice is that hollow current profiles exaggerate elongation for flux surfaces near the magnetic axis, while peaked profiles tend to limit elongation to the plasma edge. In order to demonstrate this point, the hollow current flux surface boundary condition for fig. 2-2b was chosen to be more circular than the constant current flux surfaces at the edge. Nevertheless, we see that it is more strongly shaped than the constant current surfaces near the magnetic axis. On the other hand, the peaked flux surface boundary condition in fig. 2-2c was chosen to be more shaped at the edge and we see the opposite trend. The flux surfaces become more circular than in the constant current case near the axis.

There are three general points that are illuminated by the specific cases in this

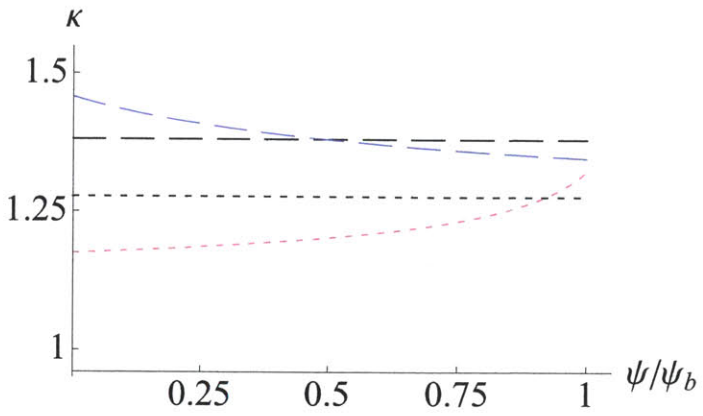

Figure 2-3: Plasma elongation from fig. 2-2b (dashed) for the constant (black) and linear hollow (blue) current profiles as well as fig. 2-2c (dotted) for the constant (black) and linear peaked (red) current profiles.

calculation. First, external PF coils only exert direct control over the flux surface shape at the plasma-vacuum boundary. Second, low order Fourier harmonics, specifically elongation, penetrate to the core most effectively. Higher order modes will only cause up-down asymmetry near the plasma edge. Lastly, a hollow toroidal current profile will more readily permit asymmetry to penetrate into the plasma core and can even amplify the asymmetry applied to the boundary. From this analysis, we identify tilted elliptical flux surfaces as the most promising geometry to create a significantly up-down asymmetric tokamak and maximize intrinsic rotation.

2.1.2 Solutions to the $O(\epsilon B_0)$ Grad-Shafranov equation

Again, we will choose simple forms for the free parameters to simplify the problem. We will solve the constant toroidal current profile case from the previous section to the next order. Specifically $-\mu_0 R_0^2 \frac{dp}{d\psi} = A_p$ and $-\frac{1}{2}\frac{d}{d\psi}(I^2) = A_m$, where A_p and A_m are positive constants and $A_p + A_m = A$. Substituting these forms, eq. (2.5), the $O(\epsilon B_0)$ Grad-Shafranov equation, becomes

$$\frac{1}{r}\frac{\partial}{\partial r}\left(r\frac{\partial \psi_1}{\partial r}\right) + \frac{1}{r^2}\frac{\partial^2 \psi_1}{\partial \theta^2} = 2A_p \frac{r}{R_{0b}}\cos(\theta) + \frac{\cos(\theta)}{R_{0b}}\frac{\partial \psi_0}{\partial r} - \frac{\sin(\theta)}{R_{0b}}\frac{1}{r}\frac{\partial \psi_0}{\partial \theta}, \qquad (2.20)$$

where R_{0b} is a free parameter which indicates the major radial location of the center of the boundary flux surface. After substituting eq. (2.9), we can be verify the solution to be

$$\psi_1(r,\theta) = \frac{A+4A_p}{16R_{0b}} r^3 \cos(\theta) + \frac{1}{4R_{0b}} \sum_{m=0}^{\infty} r^{m+1} \left(C_m \cos((m-1)\theta) + D_m \sin((m-1)\theta)\right) + \sum_{m=0}^{\infty} r^m \left(C'_m \cos(m\theta) + D'_m \sin(m\theta)\right), \tag{2.21}$$

where C'_m and D'_m are determined by the boundary conditions. For the pure $m = 2$, elliptical boundary condition studied in the previous section, the solution is given by

$$\psi_1(r,\theta) = \frac{A+4A_p}{16R_{0b}} r^3 \cos(\theta) + \frac{1}{4R_{0b}} r^3 \left(C_2 \cos(\theta) + D_2 \sin(\theta)\right) + r^3 \left(C'_3 \cos(3\theta) + D'_3 \sin(3\theta)\right) + r\left(C'_1 \cos(\theta) + D'_1 \sin(\theta)\right). \tag{2.22}$$

We have determined these coefficients by applying the condition that $\psi_1(r,\theta)$ is constant along the boundary flux surface. Using eq. (2.16), this is specified by

$$\psi_{0b} \equiv \psi_0(a) = \frac{A}{2} \frac{\kappa_b^2}{\kappa_b^2+1} a^2 = \frac{A}{4} r^2 + r^2 \left(C_2 \cos(2\theta) + D_2 \sin(2\theta)\right). \tag{2.23}$$

Next, we transform the coordinate system from polar to Cartesian using $X = r\cos(\theta)$ and $Y = r\sin(\theta)$. Then, we rotate the system by $\theta_{\kappa b}$ using $X = X'\cos(\theta_{\kappa b}) + Y'\sin(\theta_{\kappa b})$ and $Y = -X'\sin(\theta_{\kappa b}) + Y'\cos(\theta_{\kappa b})$. This aligns the axes with the major and minor radii of the elliptical boundary flux surface. Next, we substitute in the formula for the elliptical boundary $(X'/a)^2 + (Y'/b)^2 = 1$ to eliminate all instances of X'^2 and Y'^2. This allows everything to be expressed in $m = 1$ and $m = 3$ harmonics.

After transforming back into polar coordinates and rotating the system back we find

$$C_3' = \frac{\kappa_b^2 - 1}{4R_{0b}} \left(C'_{unrot} \cos\left(3\theta_{\kappa b}\right) + D'_{unrot} \sin\left(3\theta_{\kappa b}\right) \right), \tag{2.24}$$

$$D_3' = \frac{\kappa_b^2 - 1}{4R_{0b}} \left(-C'_{unrot} \sin\left(3\theta_{\kappa b}\right) + D'_{unrot} \cos\left(3\theta_{\kappa b}\right) \right), \tag{2.25}$$

$$C_1' = -\frac{\kappa_b^2 a^2}{R_{0b}} \left(C'_{unrot} \cos\left(\theta_{\kappa b}\right) + D'_{unrot} \sin\left(\theta_{\kappa b}\right) \right), \tag{2.26}$$

$$D_1' = -\frac{\kappa_b^2 a^2}{R_{0b}} \left(-C'_{unrot} \sin\left(\theta_{\kappa b}\right) + D'_{unrot} \cos\left(\theta_{\kappa b}\right) \right), \tag{2.27}$$

where

$$C'_{unrot} \equiv \frac{\left(\frac{A}{4} + C_2 + A_p\right) \cos\left(\theta_{\kappa b}\right) - D_2 \sin\left(\theta_{\kappa b}\right)}{1 + 3\kappa_b^2}, \tag{2.28}$$

$$D'_{unrot} \equiv \frac{\left(\frac{A}{4} + C_2 + A_p\right) \sin\left(\theta_{\kappa b}\right) + D_2 \cos\left(\theta_{\kappa b}\right)}{3 + \kappa_b^2}. \tag{2.29}$$

Here the boundary parameters are tied to the Fourier coefficients by eqs. (2.13) through (2.15). The location of the magnetic axis can be found by solving

$$\left.\frac{\partial \psi_0}{\partial X}\right|_{X=X_{axis}, Y=Y_{axis}} + \left.\frac{\partial \psi_1}{\partial X}\right|_{X=0, Y=0} = 0 \tag{2.30}$$

and

$$\left.\frac{\partial \psi_0}{\partial Y}\right|_{X=X_{axis}, Y=Y_{axis}} + \left.\frac{\partial \psi_1}{\partial Y}\right|_{X=0, Y=0} = 0 \tag{2.31}$$

to get

$$X_{axis} = \frac{1}{2} \frac{D_2 D_1' - \left(\frac{A}{4} - C_2\right) C_1'}{\left(\frac{A}{4}\right)^2 - C_2^2 - D_2^2}, \tag{2.32}$$

$$Y_{axis} = \frac{1}{2} \frac{D_2 C_1' - \left(\frac{A}{4} + C_2\right) D_1'}{\left(\frac{A}{4}\right)^2 - C_2^2 - D_2^2}. \tag{2.33}$$

Examining the complete solution, plotted in fig. 2-4, we see finite aspect ratio effects. Specifically, the inner flux surfaces are pushed outwards by the plasma pressure, which is referred to as the Shafranov shift. This shift is contained within the

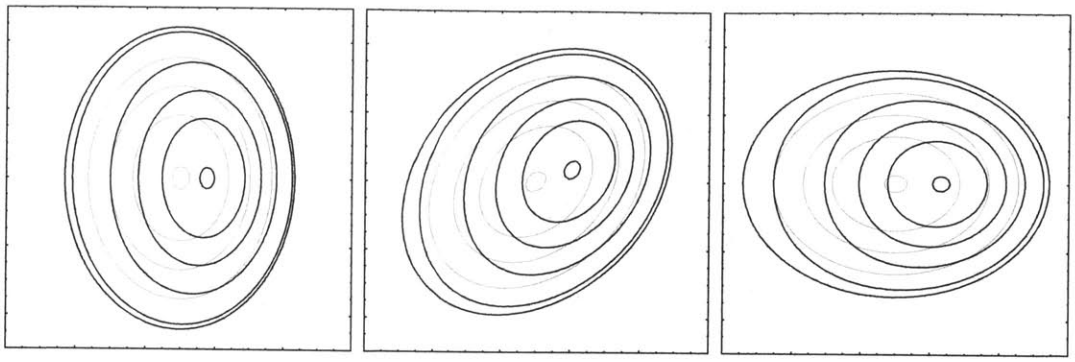

Figure 2-4: Contours of ψ_0 (gray, solid) together with their first order corrected contours, $\psi_0 + \psi_1$ (black, solid) for an elliptical boundary condition with $\theta_\kappa = \left\{0, \frac{\pi}{4}, \frac{\pi}{2}\right\}$.

$\cos(\theta)$ and $\sin(\theta)$ terms and does not necessarily occur at the same angle as the elongation. The $\cos(3\theta)$ and $\sin(3\theta)$ terms introduce triangularity with an angle of $\theta_\delta = -\frac{1}{3}\arctan\left(\frac{D_3'}{C_3'}\right)$, which becomes negligible in the limit that $r \to 0$. However, due to the Shafranov shift, in this coordinate system the magnetic axis is not located at $r = 0$. As the magnetic axis becomes closer to the plasma boundary, the effects of triangularity penetrate to the inner flux surfaces more effectively.

To get an idea of how the flux surfaces change from lowest to next order, we parameterize a flux surface as $\psi(r(\theta), \theta) = \psi_{val}$. Expanding both $\psi(r, \theta) = \psi_0(r, \theta) + \psi_1(r, \theta) + \ldots$ and $r(\theta) = r_0(\theta) + r_1(\theta) + \ldots$, the lowest order equation becomes $\psi_0(r_0(\theta), \theta) = \psi_{val}$, which we can solve for $r_0(\theta)$ using eq. (2.12). To next order we find $\psi_1(r_0(\theta), \theta) + r_1(\theta) \left.\frac{\partial \psi_0}{\partial r}\right|_{r=r_0(\theta)} = 0$, which leads to

$$r_1(\theta) = -\left(\left.\frac{\partial \psi_0}{\partial r}\right|_{r=r_0(\theta)}\right)^{-1} \psi_1(r_0(\theta), \theta). \tag{2.34}$$

This function gives the separation between the lowest and next order flux surfaces in the $\hat{e}_r$ direction and is shown in fig. 2-5. The average offset shows that each of the flux surfaces contract, relative to lowest order. The distinctive $m = 1$ component demonstrates that the Shafranov shift dominates the higher order, flux surface shaping effects. We see the finite aspect ratio effects do not strongly affect asymmetry propagation to the core.

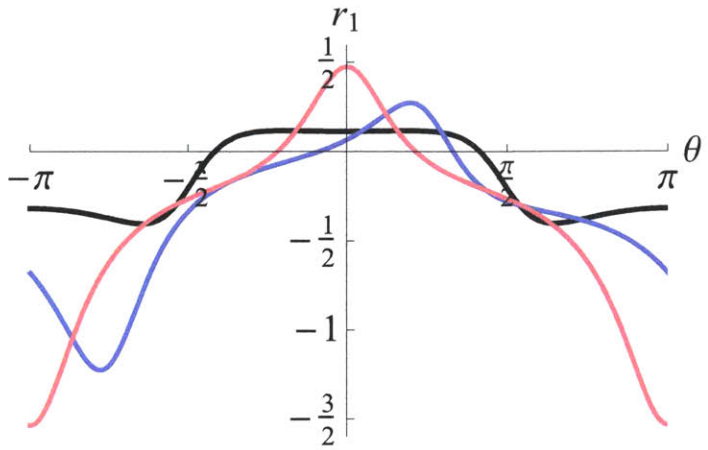

Figure 2-5: The displacement r_1 (see eq. (2.34)) between lowest order and next order flux surfaces at constant ψ_{val} for $\theta_\kappa = 0$ (black), $\theta_\kappa = \frac{\pi}{4}$ (blue), and $\theta_\kappa = \frac{\pi}{2}$ (red).

2.2 Creation and stability of elongated flux surfaces

In this section, we will first look at how PF coils are used to create a shaping field that gives the plasma elongation. Following fig. 2-6, we will find that a vertical field is necessary for equilibrium and a quadrupole field is needed for shaping. We will first calculate the strengths of the required fields and then investigate the consequences the shaping field has on plasma stability.

2.2.1 Creation of elongated flux surfaces

To produce fig. 2-6, we use a cylindrical model, ignoring the effects of toroidicity and representing the plasma current as an ideal wire. Without any external poloidal magnetic fields, the flux surfaces will be circular and the poloidal field will be a flux function. To create vertically elongated flux surfaces with say $\kappa = 2$, we must apply an external field that makes the poloidal field on the midplane a factor of 2 stronger than the poloidal field on the $R = R_0$ surface. This will stretch the flux surfaces in the vertical direction and compress them horizontally. Practically, this can be done by using PF coils to add the quadrupole magnetic field shown. The orientation of the quadrupole field determines if the plasma will be elongated vertically, horizontally, or

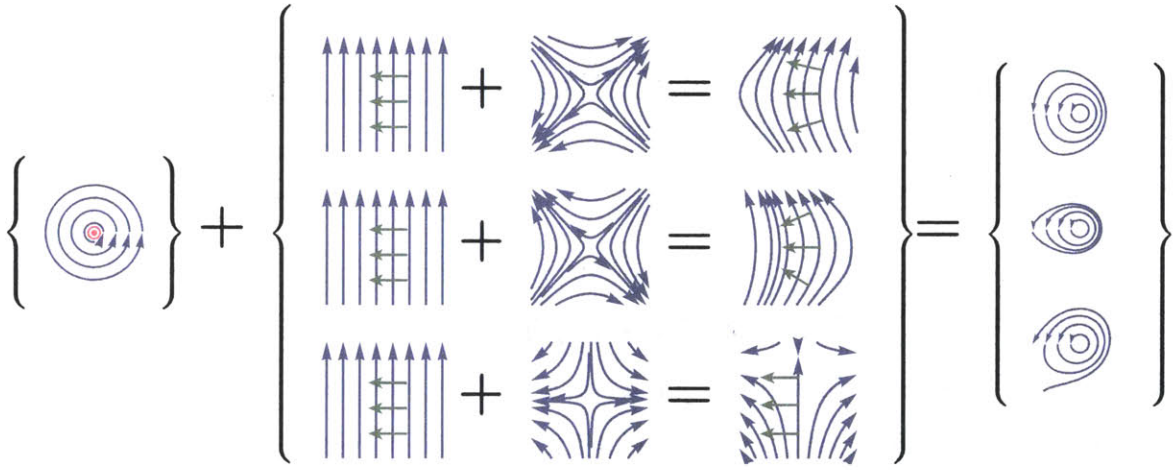

Figure 2-6: Illustrations of how vertically elongated, horizontally elongated, and tilted elongated flux surfaces (far right term) are created by the superposition of the fields generated by the plasma (far left term) and external coils (middle term). Here the plasma current is shown in red, blue represents magnetic field lines, and green shows the direction of the resulting $\vec{j} \times \vec{B}$ forces.

at an intermediate tilted angle. However, the quadrupole field introduces a curvature when combined with the vertical field. The $\vec{j} \times \vec{B}$ forces that arise from the curved external magnetic field have very different implications for plasma stability, depending on the tilt angle of the quadrupole field.

2.2.2 Equilibrium of elongated flux surfaces

The toroidal plasma geometry is fundamentally unstable to expansion in the major radial direction due to the so called tire tube, hoop, and $1/R$ forces [52]. To remedy this, vertical field coils must be added around the plasma. The plasma current, when crossed with this vertical field, produces a $\vec{j} \times \vec{B}$ force that counters the proclivity of the plasma to expand. In addition to the vertical field, a quadrupole field is needed to elongate the flux surfaces.

The necessary vertical and quadrupole fields can be calculated by generalizing a calculation done by Hakkarainen *et al.* [53] to treat tilted elliptical plasma cross-sections with a constant current distribution. The calculation takes as an input the total magnetic field within the plasma, $\vec{B}_{tot}$, obtainable from eqs. (2.12) and (2.22). We can then enforce that $\hat{n} \cdot \vec{B}_{tot} = 0$ and $\hat{t} \cdot \vec{B}_{tot} = \hat{t} \cdot \tilde{\vec{B}}_{tot}$ at the plasma boundary to determine the external field required to maintain the configuration in equilibrium. Here $\hat{n}$ is the surface normal unit vector, $\hat{t}$ is the surface tangent unit vector in the poloidal plane, and the tilde indicates a quantity outside the plasma, whereas quantities without a tilde are defined only inside the plasma. To make the mathematics tractable we will model the plasma as having a large aspect ratio ($\epsilon \ll 1$). We will also order the elongation as small ($\kappa_b - 1 \sim \epsilon$) to let the quadrupole and vertical fields compete.

Already having complete knowledge of the magnetic field inside the plasma from eqs. (2.12), (2.22), and

$$\vec{B}_{tot} = \frac{\hat{e}_\zeta \times \vec{\nabla}\psi}{R}, \tag{2.35}$$

we will begin calculating the total magnetic field outside the plasma, $\tilde{\vec{B}}_{tot}$. First, we

will write the field as

$$\vec{\tilde{B}}_{tot} = \vec{\tilde{B}}_{ext} + \vec{\tilde{B}}_w + \vec{\nabla}\tilde{\phi}, \tag{2.36}$$

where $\vec{\tilde{B}}_{ext}$ is the contribution from the external coils, $\vec{\tilde{B}}_w$ is the contribution from the plasma if it were a wire with current $I_p\hat{e}_\zeta$ located at $(R_{0b}, 0)$, and $\vec{\nabla}\tilde{\phi}$ is the correction that arises from plasma shaping and pressure effects. Making this distinction separates three different behaviors. The external flux is generated by coils at infinity and does not decay far from the tokamak. Its form is simple to guess from our understanding of the vertical and shaping fields. The wire flux is a standard result in electromagnetism and contains the divergent portion of the flux produced by the plasma current. After removing it, we can expect the error field decay to zero far from the tokamak. The magnetic fields $\vec{\tilde{B}}_{ext}$ and $\vec{\tilde{B}}_w$ are related to the poloidal fluxes through

$$\vec{\tilde{B}}_{ext} = \frac{\hat{e}_\zeta \times \vec{\nabla}\tilde{\psi}_{ext}}{R}, \tag{2.37}$$

$$\vec{\tilde{B}}_w = \frac{\hat{e}_\zeta \times \vec{\nabla}\tilde{\psi}_w}{R}. \tag{2.38}$$

In order to match the normal and tangential fields we must calculate the derivatives of the flux in both directions on the boundary.

Since we will eventually be matching to eqs. (2.12) and (2.22), we will parameterize the boundary in terms of the traditional r and θ coordinates as

$$R_b(\theta) = R_{0b} + r_b(\theta)\cos(\theta), \tag{2.39}$$

$$Z_b(\theta) = r_b(\theta)\sin(\theta), \tag{2.40}$$

where

$$r_b(\theta) = \frac{a\kappa_b}{\sqrt{\kappa_b^2\cos^2(\theta+\theta_{\kappa b}) + \sin^2(\theta+\theta_{\kappa b})}}. \tag{2.41}$$

We will immediately expand $r_b(\theta)$ in $\epsilon \ll 1$ as

$$r_b(\theta) = a\left(1 + \frac{\kappa_b - 1}{2}\left(1 - \cos\left(2\left(\theta + \theta_{\kappa b}\right)\right)\right)\right) + O\left(\epsilon^2\right). \tag{2.42}$$

for future use.

Calculation of $\tilde{\psi}_w$ from plasma parameters

The contribution to the poloidal flux from the wire, $\tilde{\psi}_w$, is already known [54, 55] to be

$$\tilde{\psi}_w = -\frac{\mu_0 I_p}{2\pi}\sqrt{RR_{0b}}\frac{\left(2 - k_{e0}^2\right)K_e\left(k_{e0}\right) - 2E_e\left(k_{e0}\right)}{k_{e0}}, \tag{2.43}$$

where $K_e(k_e) \equiv \int_0^{\pi/2} d\alpha^\dagger \left(1 - k_e^2 \sin^2\left(\alpha^\dagger\right)\right)^{-1/2}$ and $E_e(k_e) \equiv \int_0^{\pi/2} d\alpha^\dagger \sqrt{1 - k_e^2 \sin^2\left(\alpha^\dagger\right)}$ are the complete elliptic integrals of the first and second kinds, respectively. The argument of the elliptic integrals is defined to be $k_{e0}(R, Z) \equiv k_e(R, Z, R_{0b}, 0)$, where

$$k_e\left(R, Z, R^\dagger, Z^\dagger\right) \equiv \sqrt{\frac{4RR^\dagger}{\left(R + R^\dagger\right)^2 + \left(Z - Z^\dagger\right)^2}}. \tag{2.44}$$

We will now expand eq. (2.43) in $\epsilon \ll 1$ by first expanding

$$k_{e0}(r, \theta) = 1 - \frac{r^2}{8R_{0b}^2} + \frac{r^3}{8R_{0b}^3}\cos(\theta) + O\left(\epsilon^4\right). \tag{2.45}$$

We will define the next order k_{e0} as $k_{e0}^N \equiv \frac{r^2}{8R_{0b}^2} - \frac{r^3}{8R_{0b}^3}\cos(\theta)$, so we can expand the elliptic integrals as

$$K_e\left(k_{e0}\right) = \frac{1}{2}\ln\left(\frac{8}{k_{e0}^N}\right) + O\left(k_{e0}^N\right), \tag{2.46}$$

$$E_e\left(k_{e0}\right) = 1 + O\left(k_{e0}^N\right). \tag{2.47}$$

We choose to write $\tilde{\psi}_w$ on the plasma boundary as a Fourier series of the form

$$\tilde{\psi}_w^L(\theta) = \tilde{\psi}_{wC0}^L, \tag{2.48}$$

$$\tilde{\psi}_w^N(\theta) = \tilde{\psi}_{wC0}^N + \sum_{m=1}^{\infty} \tilde{\psi}_{wCm}^N \cos(m\theta) + \tilde{\psi}_{wSm}^N \sin(m\theta), \tag{2.49}$$

where the superscripts indicate lowest, L, or next, N, order and the subscripts indicate the Fourier harmonic type (sine, S, or cosine, C) and the number. We have neglected all lowest order terms apart from $m = 0$ because we can see from eq. (2.45) that $\tilde{\psi}_w^L$ will be independent of θ. Finally, we can directly expand eq. (2.43) to lowest and next order in ϵ to find the nonzero coefficients of

$$\frac{\tilde{\psi}_{wC0}^L}{aR_{0b}B_{pa}} = 2 - \ln\left(\frac{8}{\epsilon}\right), \tag{2.50}$$

$$\frac{\tilde{\psi}_{wC0}^N}{aR_{0b}B_{pa}} = \frac{\kappa_b - 1}{2}, \tag{2.51}$$

$$\frac{\tilde{\psi}_{wC1}^N}{aR_{0b}B_{pa}} = \frac{\epsilon}{2}\left(1 - \ln\left(\frac{8}{\epsilon}\right)\right), \tag{2.52}$$

$$\frac{\tilde{\psi}_{wC2}^N}{aR_{0b}B_{pa}} = -\frac{\kappa_b - 1}{2}\cos(2\theta_{\kappa b}), \tag{2.53}$$

$$\frac{\tilde{\psi}_{wS2}^N}{aR_{0b}B_{pa}} = \frac{\kappa_b - 1}{2}\sin(2\theta_{\kappa b}), \tag{2.54}$$

where $B_{pa} = \frac{\mu_0 I_p}{2\pi a}$ is the lowest order edge poloidal magnetic field. Here we see a nonzero $m = 1$ cosine term, which will eventually contribute to the Shafranov shift and the required vertical magnetic field for equilibrium. Similarly the $m = 2$ terms give the elongation and shaping magnetic field. These coefficients give all the necessary information to calculate the tangential derivative on the boundary, but not the normal derivative.

Calculation of $\tilde{\psi}'_w$ from plasma parameters

Repeating the same method, the normal derivative of $\tilde{\psi}_w$ on the plasma boundary can be constructed as

$$r_b \hat{n} \cdot \vec{\nabla} \tilde{\psi}_w^L (\theta) = \tilde{\psi}'^L_{wC0}, \tag{2.55}$$

$$r_b \hat{n} \cdot \vec{\nabla} \tilde{\psi}_w^N (\theta) = \tilde{\psi}'^N_{wC0} + \sum_{m=1}^{\infty} \tilde{\psi}'^N_{wCm} \cos(m\theta) + \tilde{\psi}'^N_{wSm} \sin(m\theta). \tag{2.56}$$

Calculating these coefficients requires the unit normal vector, which can be derived from the flux surface parameterization using

$$\hat{n} = \frac{\frac{dZ_b}{d\theta}\hat{e}_R - \frac{dR_b}{d\theta}\hat{e}_Z}{\sqrt{\left(\frac{dR_b}{d\theta}\right)^2 + \left(\frac{dZ_b}{d\theta}\right)^2}} \approx \hat{e}_r - \frac{1}{r_b}\frac{dr_b}{d\theta}\hat{e}_\theta. \tag{2.57}$$

This, together with eq. (2.41), can be used to expand the gradient of eq. (2.43) to find the nonzero coefficients to be

$$\frac{\tilde{\psi}'^L_{wC0}}{aR_{0b}B_{pa}} = 1, \tag{2.58}$$

$$\frac{\tilde{\psi}'^N_{wC1}}{aR_{0b}B_{pa}} = \frac{\epsilon}{2}\left(2 - \ln\left(\frac{8}{\epsilon}\right)\right). \tag{2.59}$$

This entirely specifies the contributions from the wire magnetic field.

Calculation of $\tilde{\phi}\left(\tilde{\phi}'\right)$

We now focus on $\vec{\nabla}\tilde{\phi}$, the magnetic field that corrects the errors from modeling the plasma as a wire. We can relate $\tilde{\phi}$ and its normal derivatives using Green's theorem

$$\tilde{\phi} = 2\oint_0^{2\pi} d\theta^\dagger \left[G(\theta, \theta^\dagger)\, r_b R_b \hat{n} \cdot \vec{\nabla}\tilde{\phi}(\theta^\dagger) - \tilde{\phi}(\theta^\dagger)\, r_b(\theta^\dagger)\, R_b(\theta^\dagger)\, \hat{n}(\theta^\dagger) \cdot \vec{\nabla}^\dagger G(\theta, \theta^\dagger)\right] \tag{2.60}$$

evaluated on the boundary. The free-space Green's function [56] in our coordinates is given by

$$G\left(R,Z,R',Z'\right)=\frac{1}{2\pi}\frac{k_eK_e\left(k_e\right)}{\sqrt{RR'}}, \tag{2.61}$$

where k_e is defined in eq. (2.44). Again, we will construct Fourier-analyzed forms for

$$\tilde{\phi}^L\left(\theta\right)=\tilde{\phi}^L_{C0}, \tag{2.62}$$

$$\tilde{\phi}^N\left(\theta\right)=\tilde{\phi}^N_{C0}+\sum_{m=1}^{\infty}\tilde{\phi}^N_{Cm}\cos\left(m\theta\right)+\tilde{\phi}^N_{Sm}\sin\left(m\theta\right) \tag{2.63}$$

and

$$r_bR_b\hat{n}\cdot\vec{\nabla}\tilde{\phi}^L\left(\theta\right)=R_{0b}\left(\tilde{\phi}'^L_{C0}\right), \tag{2.64}$$

$$r_bR_b\hat{n}\cdot\vec{\nabla}\tilde{\phi}^N\left(\theta\right)=R_{0b}\left(\tilde{\phi}'^N_{C0}+\sum_{m=1}^{\infty}\tilde{\phi}'^N_{Cm}\cos\left(m\theta\right)+\tilde{\phi}'^N_{Sm}\sin\left(m\theta\right)\right). \tag{2.65}$$

After inserting eqs. (2.61) through (2.65) into eq. (2.60), expanding in ϵ, and equating the different harmonics in θ we find

$$\tilde{\phi}^L_{C0}=-\ln\left(4\right)\tilde{\phi}'^L_{C0}. \tag{2.66}$$

to lowest order. To next order we find

$$\tilde{\phi}^N_{C0}=-\epsilon\ln\left(4\right)\tilde{\phi}'^N_{C0}+\epsilon\left(\frac{1}{4}+\ln\left(2\right)\right)\tilde{\phi}'^L_{C1}, \tag{2.67}$$

$$\tilde{\phi}^N_{C1}=2\epsilon\left(\frac{1}{4}+\ln\left(2\right)\right)\tilde{\phi}'^L_{C0}-\tilde{\phi}'^N_{C1}+\frac{\epsilon}{2}\tilde{\phi}'^L_{C2}, \tag{2.68}$$

$$\tilde{\phi}^N_{S1}=-\tilde{\phi}'^N_{S1}+\frac{\epsilon}{2}\tilde{\phi}'^L_{S2}, \tag{2.69}$$

$$\tilde{\phi}^N_{C2}=\frac{\epsilon}{2}\tilde{\phi}'^L_{C1}-\frac{1}{2}\tilde{\phi}'^N_{C2}+\frac{\epsilon}{4}\tilde{\phi}'^L_{C3}, \tag{2.70}$$

$$\tilde{\phi}^N_{S2}=\frac{\epsilon}{2}\tilde{\phi}'^L_{S1}-\frac{1}{2}\tilde{\phi}'^N_{S2}+\frac{\epsilon}{4}\tilde{\phi}'^L_{S3}. \tag{2.71}$$

Calculation of $\tilde{\phi}'\left(\tilde{\psi}_w, \tilde{B}_{ext}\right)$

Finally we have sufficient information to make use of the condition $\hat{n} \cdot \vec{\tilde{B}}_{tot} = 0$ at the plasma boundary. In our notation this condition is given by

$$r_b R_b \hat{n} \cdot \vec{\nabla} \tilde{\phi} = (\hat{n} \cdot \hat{e}_r) \left. \frac{\partial}{\partial \theta} \right|_{\psi} \left(\tilde{\psi}_{ext} + \tilde{\psi}_w \right). \tag{2.72}$$

The form of $r_b R_b \hat{n} \cdot \vec{\nabla} \tilde{\phi}$ has already been specified by eqs. (2.64) and (2.65), as has $\tilde{\psi}_w(\theta)$ by eqs. (2.48) and (2.49). The external field will be written everywhere outside the plasma using a multipole expansion as

$$\tilde{\psi}^L_{ext}(r, \theta) = 0, \tag{2.73}$$

$$\tilde{\psi}^N_{ext}(r, \theta) = R^2_{0b} \left(\sum_{m=1}^{\infty} \left(\frac{r}{R_{0b}} \right)^m \left(\tilde{B}^N_{extCm} \cos(m\theta) + \tilde{B}^N_{extSm} \sin(m\theta) \right) \right). \tag{2.74}$$

To lowest order in aspect ratio the external field is zero, because we assumed weak plasma shaping and we expect the necessary vertical field to be small.

For convenience we can rewrite the unit normal vector from eq. (2.57) as

$$\hat{n} = ((\hat{n} \cdot \hat{e}_R) \cos(\theta) + (\hat{n} \cdot \hat{e}_Z) \sin(\theta)) \hat{e}_r + (-(\hat{n} \cdot \hat{e}_R) \sin(\theta) + (\hat{n} \cdot \hat{e}_Z) \cos(\theta)) \hat{e}_\theta. \tag{2.75}$$

Expanding eq. (2.72) in powers of ϵ and equating harmonics we find

$$\tilde{\phi}'^L_{C0} = 0 \tag{2.76}$$

to lowest order in ϵ. The next order is more meaningful, giving nonzero coefficients

of

$$\tilde{\phi'}^N_{S1} = -\frac{1}{R_{0b}}\left(\tilde{\psi}^N_{wC1} + \epsilon^2 R^2_{0b}\tilde{B}^N_{extC1}\right), \tag{2.77}$$

$$\tilde{\phi'}^N_{C2} = \frac{2}{R_{0b}}\left(\tilde{\psi}^N_{wS2} + \epsilon^3 R^2_{0b}\tilde{B}^N_{extS2}\right), \tag{2.78}$$

$$\tilde{\phi'}^N_{S2} = -\frac{2}{R_{0b}}\left(\tilde{\psi}^N_{wC2} + \epsilon^3 R^2_{0b}\tilde{B}^N_{extC2}\right). \tag{2.79}$$

Calculation of $\tilde{B}_{ext}\left(\psi, \tilde{\psi'}_w, \tilde{\phi}\right)$

Lastly, we will match $\hat{t}\cdot\vec{B}_{tot} = \hat{t}\cdot\vec{\tilde{B}}_{tot}$ across the plasma boundary. This condition is given by

$$r\hat{n}\cdot\vec{\nabla}\psi = r\hat{n}\cdot\vec{\nabla}\tilde{\psi}_{ext} + r\hat{n}\cdot\vec{\nabla}\psi_w + (\hat{n}\cdot\hat{e}_r)\,R\left.\frac{\partial\tilde{\phi}}{\partial\theta}\right|_{\psi}, \tag{2.80}$$

where the second and last terms can be directly differentiated using eqs. (2.62), (2.63), (2.73), and (2.74). We have already prescribed a form for the third term in eqs. (2.55) and (2.56). The first term is the contribution from inside the plasma. We will use our solution for the constant current case, calculated to lowest order in Section 2.1.1 and next order in Section 2.1.2. In the lowest order solution we assumed that the toroidal current density, j_ζ, was constant. Additionally, in the next order derivation we assumed that the pressure gradient, $\frac{dp}{d\psi}$, was constant. The gradient we require for this derivation can be directly calculated from eqs. (2.12) and (2.22). However, we must remember to substitute the coefficients appearing in eqs. (2.17) through (2.19) and (2.24) through (2.29) to capture the proper dependencies on κ_b. Additionally, we must expand the toroidal current density, $j_\zeta = j^L_\zeta + j^N_\zeta$ in ϵ to cancel the contribution from eq. (2.58) that enters the next order $m = 0$ equation. After all the substitutions are made, we can expand eq. (2.80) in ϵ. The lowest order $m = 0$ equation determines the lowest order toroidal current density to be

$$j^L_\zeta = \frac{2B_{pa}}{\mu_0 a}. \tag{2.81}$$

This is consistent with $I_p = \pi a^2 j_\zeta$ and $B_{pa} = \frac{\mu_0 I_p}{2\pi a}$, which are accurate for the lowest order, circular flux surfaces. The next order $m = 0$ equation gives that

$$j_\zeta^N = -\left(\kappa_b - 1\right)\frac{2B_{pa}}{\mu_0 a}. \tag{2.82}$$

The $m = 1$ and $m = 2$ harmonics show the coefficients of the external magnetic field are

$$\tilde{B}_{extC1}^N = -\frac{1}{\epsilon^2 R_{0b}}\left(\tilde{\phi}_{S1}^N + \frac{\tilde{\psi}'^N_{wC1}}{R_{0b}} + \frac{\epsilon^3}{2}\mu_0 R_{0b}^3 \frac{dp}{d\psi} - \frac{\epsilon^3}{8}\mu_0 R_{0b}^2 j_\zeta^L\right), \tag{2.83}$$

$$\tilde{B}_{extS1}^N = \frac{1}{\epsilon^2 R_{0b}}\tilde{\phi}_{C1}^N, \tag{2.84}$$

$$\tilde{B}_{extC2}^N = -\frac{1}{\epsilon^3 R_{0b}}\tilde{\phi}_{S2}^N, \tag{2.85}$$

$$\tilde{B}_{extS2}^N = \frac{1}{\epsilon^3 R_{0b}}\tilde{\phi}_{C2}^N. \tag{2.86}$$

Calculation of $\tilde{B}_{ext}$ from plasma parameters

Putting together all of these results we can calculate $\tilde{B}_{ext}\left(\psi, \tilde{\psi}'_w, \tilde{\phi}\left(\tilde{\phi}'\left(\tilde{\psi}_w, \tilde{B}_{ext}\right)\right)\right)$, which only includes $\tilde{B}_{ext}$ and plasma parameters. Solving for $\tilde{B}_{ext}$, we find the external field necessary for equilibrium. These coefficients are

$$\tilde{B}_{extC1}^N = \frac{\epsilon B_{pa}}{2}\left(-\frac{a\mu_0 R_{0b}}{2B_{pa}}\frac{dp}{d\psi} - \frac{5}{4} + \ln\left(\frac{8}{\epsilon}\right)\right), \tag{2.87}$$

$$\tilde{B}_{extS1}^N = 0, \tag{2.88}$$

$$\tilde{B}_{extC2}^N = \frac{B_{pa}}{4}\left(\kappa_b - 1\right)\cos\left(2\theta_{\kappa b}\right), \tag{2.89}$$

$$\tilde{B}_{extS2}^N = -\frac{B_{pa}}{4}\left(\kappa_b - 1\right)\sin\left(2\theta_{\kappa b}\right). \tag{2.90}$$

We clearly can see the expected $m = 1$ cosine term, which represents the required vertical field for equilibrium, as well as the $m = 2$ elongation shaping terms.

Using eqs. (2.37) and (2.74) the required externally applied vertical field can be

shown to be

$$\vec{B}_{v0} = \frac{\mu_0 I_p}{4\pi R_{0b}} \left(-\frac{a\mu_0 R_{0b}}{2B_{pa}} \frac{dp}{d\psi} - \frac{5}{4} + \ln\left(\frac{8}{\epsilon}\right) \right) \hat{e}_Z. \tag{2.91}$$

The usual required vertical field [57] is given by

$$\vec{B}_{v0} = \frac{\mu_0 I_p}{4\pi R_{0b}} \left(\beta_p + \frac{l_i}{2} - \frac{3}{2} + \ln\left(\frac{8}{\epsilon}\right) \right) \hat{e}_Z, \tag{2.92}$$

where $l_i \equiv \frac{\langle B_p^2 \rangle_V}{B_{pa}^2}$ is the dimensionless internal inductance per unit length and $\beta_p \equiv \frac{2\mu_0 \langle p \rangle_V}{B_{pa}^2}$ is the poloidal beta. We can resolve the apparent discrepancies by taking into account the assumptions that went into our calculation. First of all, we assumed a constant toroidal current profile, which implies $l_i = 1/2$. We also assumed that the pressure gradient, $\frac{dp}{d\psi}$, was constant. After direct integration (with the boundary condition that $p(a) = 0$), we can use eq. (2.12) (with $C_2 = D_2 = 0$ because $\kappa_b = 1$ to lowest order). Then, substituting eq. (2.17), we arrive at a pressure distribution of

$$p(r) = \frac{\mu_0 j_\zeta R_{0b}}{4} \left(r^2 - a^2\right) \frac{dp}{d\psi}. \tag{2.93}$$

Using eq. (2.81) with the definition of the poloidal beta we see that

$$\beta_p = -\frac{a\mu_0 R_{0b}}{2B_{pa}} \frac{dp}{d\psi}. \tag{2.94}$$

Hence, we are in perfect agreement with the accepted value for the required vertical field for plasma equilibrium in the major radial direction.

Lastly, again using eqs. (2.37) and (2.74) with our external field coefficients, we see that the shaping field needed to create a weak elongation κ is

$$\begin{aligned} \vec{B}_{shape} = \frac{\mu_0 I_p}{4\pi a^2} (\kappa_b - 1) \Big(\big((R - R_{0b}) \sin(2\theta_{\kappa b}) + Z\cos(2\theta_{\kappa b}) \big) \hat{e}_R \\ + \big((R - R_{0b}) \cos(2\theta_{\kappa b}) - Z\sin(2\theta_{\kappa b}) \big) \hat{e}_Z \Big) \end{aligned} \tag{2.95}$$

and the total external field is given by

$$\vec{B}_{ext} = \vec{B}_{v0} + \vec{B}_{shape}. \tag{2.96}$$

2.2.3 Stability of elongated flux surfaces to axisymmetric modes

The addition of the quadrupole magnetic field has an unintended effect on plasma stability. The net external field, which previously was straight and vertical, becomes curved as shown in the first set of curly braces in fig. 2-6. For the case of vertical elongation, when the plasma is perturbed vertically the external field curvature will lead to a $\vec{j} \times \vec{B}$ force that drives further displacement.

Vertical elongation is common in current experiments. This instability is addressed using active feedback coil systems. However these feedback coils must be placed close to the plasma to achieve the necessary response time and the instability still ultimately limits the maximum vertical elongation. In fact, these vertical displacement events (VDEs) are intimately linked with disruptions [58] and have the potential to destroy the machine [59, 60]. This suggests that pushing vertical elongation may be a significant source of risk for disruption-intolerant devices such as ITER and future power plant reactors.

While horizontally elongated flux surfaces are vertically stable, they become less stable horizontally. This is because the strength of the vertical field applied must necessarily decrease with major radius in order to create horizontal elongation. However, we see in eq. (2.92) that a modest amount of horizontal elongation can still be stable because the required vertical field for equilibrium also decreases with major radius. A horizontally elongated flux surface is stable as long as the local slope of the required vertical field is more negative than the slope of the actual external field used to create the elongation. This requirement for stability can be expressed as

$$\frac{\partial}{\partial R_{0b}}\left(\hat{e}_z \cdot \vec{B}_{v0}\right) \leq \frac{\partial}{\partial R}\left(\hat{e}_z \cdot \vec{B}_{ext}\right). \tag{2.97}$$

However, to calculate these derivatives we must know how the plasma parameters in eq. (2.92) respond to plasma displacement. In this derivation we will assume the plasma responds adiabatically and that the poloidal and toroidal fluxes are conserved. Additionally, we will assume that the plasma current profile shape (but not necessarily I_p) stays constant. Furthermore, we will assume that the external coils that generate the field in eq. (2.96) are unaffected by the plasma motion. This is not entirely true, especially if the tokamak has an iron core. Tilted flux surfaces are less intuitive than the case of vertical elongation and must be treated formally. We will estimate stability for the constant toroidal current density case by using the external magnetic field calculated in the previous section.

Fundamentally, just as equilibrium is given by

$$\vec{F}_{tot} \equiv \sum_i \vec{F}_i = \vec{F}_p + \vec{F}_{ext} = \vec{F}_p + \vec{I}_p \times \vec{B}_{ext} = 0, \tag{2.98}$$

stability is governed by

$$\vec{\nabla}\vec{F}_{tot} = \vec{\nabla}\left(\sum_i \vec{F}_i\right) = \vec{\nabla}\left(\vec{F}_p + \vec{F}_{ext}\right) = \vec{\nabla}\left(\vec{F}_p + \vec{I}_p \times \vec{B}_{ext}\right) \leq 0, \tag{2.99}$$

evaluated at $R = R_{0b}$ and $Z = 0$. Here

$$\vec{F}_p = -\vec{I}_p \times \vec{B}_v = \frac{\mu_0 I_p^2}{4\pi R}\left(\beta_p + \frac{l_i}{2} - \frac{3}{2} + \ln\left(\frac{8R}{a}\right)\right)\hat{e}_R \tag{2.100}$$

is the force the plasma exerts in the major radial direction due to the tire tube, hoop, and $1/R$ forces, which can be inferred from eq. (2.92). If any of the eigenvalues of the matrix appearing in eq. (2.99) are positive the system is unstable. In our two dimensional system the determinant of this matrix can be calculated to give the two eigenvalues,

$$\lambda_\pm = \frac{1}{2}\left(\frac{\partial F_{totR}}{\partial R} + \frac{\partial F_{totZ}}{\partial Z} \pm \sqrt{\left(\frac{\partial F_{totR}}{\partial R} - \frac{\partial F_{totZ}}{\partial Z}\right)^2 + 4\frac{\partial F_{totR}}{\partial Z}\frac{\partial F_{totZ}}{\partial R}}\right). \tag{2.101}$$

We will select the positive sign, since it will always be the more limiting case for stability. By nondimensionalizing the eigenvalue, we can define the decay index (also called the marginal force index for stability),

$$n_c \equiv -\frac{1}{2}\frac{R_{0b}}{F_{p0}}\left(\frac{\partial F_{totR}}{\partial R}+\frac{\partial F_{totZ}}{\partial Z}+\sqrt{\left(\frac{\partial F_{totR}}{\partial R}-\frac{\partial F_{totZ}}{\partial Z}\right)^2+4\frac{\partial F_{totR}}{\partial Z}\frac{\partial F_{totZ}}{\partial R}}\right) \tag{2.102}$$

where $\vec{F}_{p0} \equiv \vec{F}_p\Big|_{R=R_{0b},Z=0}$ and all derivatives are evaluated at the equilibrium position. The condition for stability to displacements in all directions becomes

$$n_c \geq 0. \tag{2.103}$$

We note that, in the limit that $\kappa \to 1$, we find $\frac{\partial}{\partial Z} = 0$ and $\vec{B}_{ext} = \vec{B}_{v0}$. Then, the two eigenvalues become 0 (indicating neutral vertical stability) and the familiar major radial decay index [61] of $-\frac{R_{0b}}{B_{v0}}\frac{\partial B_{vZ}}{\partial R}\Big|_{R=R_{0b},Z=0}$, where $\vec{B}_v \equiv \frac{1}{I_p^2}\vec{I}_p \times \vec{F}_p$. Note that $\vec{B}_v$ is the required vertical field at the perturbed position, whereas $\vec{B}_{v0}$ is the physical field that exists to maintain the plasma when it is at its equilibrium position.

We need to calculate all of the forces on the plasma and how they vary in the R and Z directions. We need the form of the external magnetic field, which was calculated in the previous section and is given by eqs. (2.92), (2.95), and (2.96). This field is appropriate to tilted elliptical flux surfaces in a plasma with constant pressure and current profiles (see the left plot of fig. 2-2a). Therefore the total external force field, $\vec{F}_{ext} = \vec{I}_p \times \vec{B}_{ext}$, is given by

$$\vec{F}_{ext} = \vec{I}_p \times \vec{B}_{v0} + \frac{\mu_0 I_p^2}{4\pi a^2}(\kappa_b - 1)\left(-\left((R-R_0)\cos(2\theta_{\kappa b}) - Z\sin(2\theta_{\kappa b})\right)\hat{e}_R \right.$$
$$\left. + \left((R-R_0)\sin(2\theta_{\kappa b}) + Z\cos(2\theta_{\kappa b})\right)\hat{e}_Z\right), \tag{2.104}$$

where $\vec{I_p} = I_p \hat{e}_\zeta$. We can calculate all of the required normalized derivatives to be

$$\frac{R_0}{F_{p0}}\frac{\partial F_{extR}}{\partial R} = -\frac{1}{\epsilon^2}\left(\ln\left(\frac{8}{\epsilon}\right) - \frac{3}{2} + \frac{l_i}{2} + \beta_p\right)^{-1}(\kappa_b - 1)\cos\left(2\theta_{\kappa b}\right) - \frac{R_0}{F_{p0}}\left.\frac{\partial I_p}{\partial R}\right|_\psi B_{v0}, \tag{2.105}$$

$$\frac{R_0}{F_{p0}}\frac{\partial F_{extR}}{\partial Z} = \frac{1}{\epsilon^2}\left(\ln\left(\frac{8}{\epsilon}\right) - \frac{3}{2} + \frac{l_i}{2} + \beta_p\right)^{-1}(\kappa_b - 1)\sin\left(2\theta_{\kappa b}\right), \tag{2.106}$$

$$\frac{R_0}{F_{p0}}\frac{\partial F_{extZ}}{\partial R} = \frac{1}{\epsilon^2}\left(\ln\left(\frac{8}{\epsilon}\right) - \frac{3}{2} + \frac{l_i}{2} + \beta_p\right)^{-1}(\kappa_b - 1)\sin\left(2\theta_{\kappa b}\right), \tag{2.107}$$

$$\frac{R_0}{F_{p0}}\frac{\partial F_{extZ}}{\partial Z} = \frac{1}{\epsilon^2}\left(\ln\left(\frac{8}{\epsilon}\right) - \frac{3}{2} + \frac{l_i}{2} + \beta_p\right)^{-1}(\kappa_b - 1)\cos\left(2\theta_{\kappa b}\right), \tag{2.108}$$

evaluated at $(R_{0b}, 0)$. This assumes that the external fields are constant during the perturbation of the plasma.

We also need the contributions from the plasma forces. However, since $\vec{F_p}$ does not depend on Z and has no Z component we find that

$$\frac{R_0}{F_{p0}}\frac{\partial F_{pR}}{\partial Z} = \frac{R_0}{F_{p0}}\frac{\partial F_{pZ}}{\partial R} = \frac{R_0}{F_{p0}}\frac{\partial F_{pZ}}{\partial Z} = 0. \tag{2.109}$$

To calculate $\frac{\partial F_{pR}}{\partial R}$ we follow an unpublished calculation by I.H. Hutchinson. First we will write F_{pR} in terms of the plasma inductance $L = L_i + L_e$, distinguishing the contributions from inside and outside the plasma. By using $E_m = \frac{1}{2}LI_p^2$ and integrating for the stored magnetic energy, $E_m = \int dV\left(\frac{B_p^2}{2\mu_0}\right)$, over the plasma region, the internal inductance can be calculated to be $L_i = \mu_0 R\frac{l_i}{2}$. Repeating the process for L_e over the vacuum region, the external inductance can be calculated to be $L_e = \mu_0 R\left(\ln\left(\frac{8R}{a}\right) - 2\right)$. The total inductance is then

$$L = \mu_0 R\left(\ln\left(\frac{8R}{a}\right) - 2 + \frac{l_i}{2}\right). \tag{2.110}$$

We would now like to find the derivative of L, but we do not know how the minor radius changes as the plasma is perturbed about the equilibrium in the major radial direction. To calculate this we will assume conservation of toroidal flux

$\chi \equiv \frac{1}{2\pi}\int_0^{2\pi} d\theta \int_0^a dr\,(rB_\zeta(R)) = \frac{\pi a^2}{2\pi} B_\zeta(R)$ to lowest order in aspect ratio. Since $B_\zeta(R) \propto 1/R$, we find that $a^2 \propto R$. Assuming that the current profile (and therefore l_i) does not change with the perturbation we find

$$\left.\frac{\partial L}{\partial R}\right|_\psi = \mu_0 \left(\ln\left(\frac{8R}{a}\right) - \frac{3}{2} + \frac{l_i}{2}\right). \tag{2.111}$$

This means, referring to eq. (2.100), we can write the radial force as

$$F_{pR} = \frac{\mu_0 I_p^2}{4\pi R}\left(\left.\frac{\partial L}{\partial R}\right|_\psi + \beta_p\right)\hat{e}_R. \tag{2.112}$$

Taking the derivative we find

$$\frac{\partial F_{pR}}{\partial R} = F_p\left(-\frac{1}{R_0} + \frac{1}{I_p}\left.\frac{\partial I_p}{\partial R}\right|_\psi + \left(\left.\frac{\partial L}{\partial R}\right|_\psi + \mu_0\beta_p\right)^{-1}\left(\left.\frac{d^2L}{dR^2}\right|_\psi + \mu_0\left.\frac{\partial \beta_p}{\partial R}\right|_\psi\right)\right) + \left.\frac{\partial I_p}{\partial R}\right|_\psi B_{v0}. \tag{2.113}$$

The second derivative of the inductance can be calculated directly from eq. (2.111) (remembering that $a^2 \propto R$) as

$$\left.\frac{\partial^2 L}{\partial R^2}\right|_\psi = \frac{\mu_0}{2R}. \tag{2.114}$$

Earlier we assumed that the external fields are constant during the plasma perturbation, so we may say $B_{ext}(R, R') = B_{ext}(R')$, where R is the location of the plasma and R' is an integration variable. Using conservation of poloidal flux, remembering to factor in the effect of the external field, we can write

$$\psi = LI_p - 2\pi\int_0^R dR'\,(R'B_{ext}(R')) \tag{2.115}$$

to find

$$\frac{\partial \psi}{\partial R} = \frac{\partial}{\partial R}\left(LI_p - 2\pi\int_0^R dR'\,(R'B_{ext}(R'))\right) = 0. \tag{2.116}$$

Rearranging, we find that

$$\left.\frac{\partial I_p}{\partial R}\right|_\psi = \frac{1}{L}\left(2\pi R B_{ext} - \left.\frac{\partial L}{\partial R}\right|_\psi I_p\right). \tag{2.117}$$

To determine how the perturbation modifies β_p we will assume the plasma is an ideal gas undergoing an adiabatic change, meaning pV^{γ_c} is constant, where γ_c is the ratio of specific heats. Taking $\gamma_c = 5/3$ and remembering that $a^2 \propto R$, we deduce that $p \propto R^{-2\gamma_c} = R^{-10/3}$ [62]. Since $\beta_p = \frac{8\pi^2 a^2 \langle p\rangle_V}{\mu_0 I_p^2}$ we arrive at

$$\left.\frac{\partial \beta_p}{\partial R}\right|_\psi = -\frac{\beta_p}{R}\left(\frac{7}{3} + 2\frac{R}{I_p}\left.\frac{\partial I_p}{\partial R}\right|_\psi\right). \tag{2.118}$$

Combining eqs. (2.110), (2.111), (2.113) (2.114), (2.117), and (2.118) yields

$$\begin{aligned}\frac{R_0}{F_{p0}}\frac{\partial F_{pR}}{\partial R} = \frac{R_0}{F_{p0}}\left.\frac{\partial I_p}{\partial R}\right|_\psi B_{v0} - 1 - \frac{-\frac{1}{2}+\frac{7}{3}\beta_p}{\ln\left(\frac{8}{\epsilon}\right)-\frac{3}{2}+\frac{l_i}{2}+\beta_p} \\ - \frac{\left(\ln\left(\frac{8}{\epsilon}\right)-\frac{3}{2}+\frac{l_i}{2}-\beta_p\right)^2}{2\left(\ln\left(\frac{8}{\epsilon}\right)-\frac{3}{2}+\frac{l_i}{2}+\beta_p\right)\left(\ln\left(\frac{8}{\epsilon}\right)-2+\frac{l_i}{2}\right)}.\end{aligned} \tag{2.119}$$

The final form of the decay index, using eqs. (2.105) through (2.108) and (2.119), is given by eq. (2.102) and

$$\begin{aligned}\frac{R_0}{F_{p0}}\frac{\partial F_{totR}}{\partial R} = -\frac{1}{\epsilon^2}\left(\ln\left(\frac{8}{\epsilon}\right)-\frac{3}{2}+\frac{l_i}{2}+\beta_p\right)^{-1}(\kappa_b-1)\cos\left(2\theta_{\kappa b}\right) \\ - 1 - \frac{-\frac{1}{2}+\frac{7}{3}\beta_p}{\ln\left(\frac{8}{\epsilon}\right)-\frac{3}{2}+\frac{l_i}{2}+\beta_p} \\ - \frac{\left(\ln\left(\frac{8}{\epsilon}\right)-\frac{3}{2}+\frac{l_i}{2}-\beta_p\right)^2}{2\left(\ln\left(\frac{8}{\epsilon}\right)-\frac{3}{2}+\frac{l_i}{2}+\beta_p\right)\left(\ln\left(\frac{8}{\epsilon}\right)-2+\frac{l_i}{2}\right)},\end{aligned} \tag{2.120}$$

$$\frac{R_0}{F_{p0}}\frac{\partial F_{totR}}{\partial Z} = \frac{1}{\epsilon^2}\left(\ln\left(\frac{8}{\epsilon}\right)-\frac{3}{2}+\frac{l_i}{2}+\beta_p\right)^{-1}(\kappa_b-1)\sin\left(2\theta_{\kappa b}\right), \tag{2.121}$$

$$\frac{R_0}{F_{p0}}\frac{\partial F_{totZ}}{\partial R} = \frac{1}{\epsilon^2}\left(\ln\left(\frac{8}{\epsilon}\right)-\frac{3}{2}+\frac{l_i}{2}+\beta_p\right)^{-1}(\kappa_b-1)\sin\left(2\theta_{\kappa b}\right), \tag{2.122}$$

$$\frac{R_0}{F_{p0}}\frac{\partial F_{totZ}}{\partial Z} = \frac{1}{\epsilon^2}\left(\ln\left(\frac{8}{\epsilon}\right)-\frac{3}{2}+\frac{l_i}{2}+\beta_p\right)^{-1}(\kappa_b-1)\cos\left(2\theta_{\kappa b}\right). \tag{2.123}$$

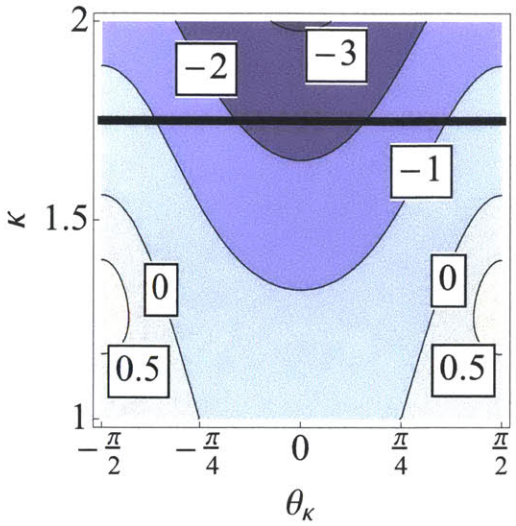

Figure 2-7: Contours of the decay index, n_c, (which must be greater than 0 for stability) at $\epsilon = 1/3$, $l_i = 1/2$, and $\beta_p = 1$, with the elongation of ITER [5] (thick, black) indicated for reference.

We note that in the large aspect ratio limit with $\kappa_b = 1$, this solution produces the traditionally accepted decay index for radial stability, $\lambda_+ = \frac{3}{2}$ [61]. It only depends on κ_b, $\theta_{\kappa b}$, ϵ, β_p, and l_i and is plotted for example parameters in fig. 2-7. We see that, for horizontal elongation, the plasma will encounter a restoring force with vertical displacement, but be less stable horizontally. However, this opens up a stability window because tokamaks have some natural stability to radial displacements because the tire tube and hoop forces weaken with major radius. Nevertheless, for strong horizontal elongation this natural stability can be overwhelmed. We also see that vertically elongated flux surfaces are inherently unstable. This is due to the curvature of the external magnetic field shown in fig. 2-6. Importantly, tilted flux surfaces are simply intermediates between these two extreme cases.

Chapter 3

GS2 [63]

GS2 is a local δf gyrokinetic code that self-consistently calculates turbulent transport in tokamak or stellarator geometries. First we will present a brief overview of GS2 and detail how we specify the geometry for a local equilibrium. Then we will describe the modifications that were necessary to properly model up-down asymmetric configurations. Lastly, we will recount the test cases that were used to confirm the functionality of the modified code.

3.1 Code overview

Fundamentally GS2 solves the gyrokinetic and quasineutrality equations in a domain following a single field line on a single flux surface. Along the field line the domain extends along the scale of the machine, while in the perpendicular directions it only spans several ion gyroradii (see fig. 3-1). GS2 can be run either linearly or nonlinearly for a single or many modes. It is appropriate for determining transport due to turbulent instabilities, such as the ion temperature gradient and trapped electron modes. The effects of finite beta, flow, and flow shear may be included, but were ignored in this work. It can also include collisional effects, but collisions were only used to verify they had little effect on the results.

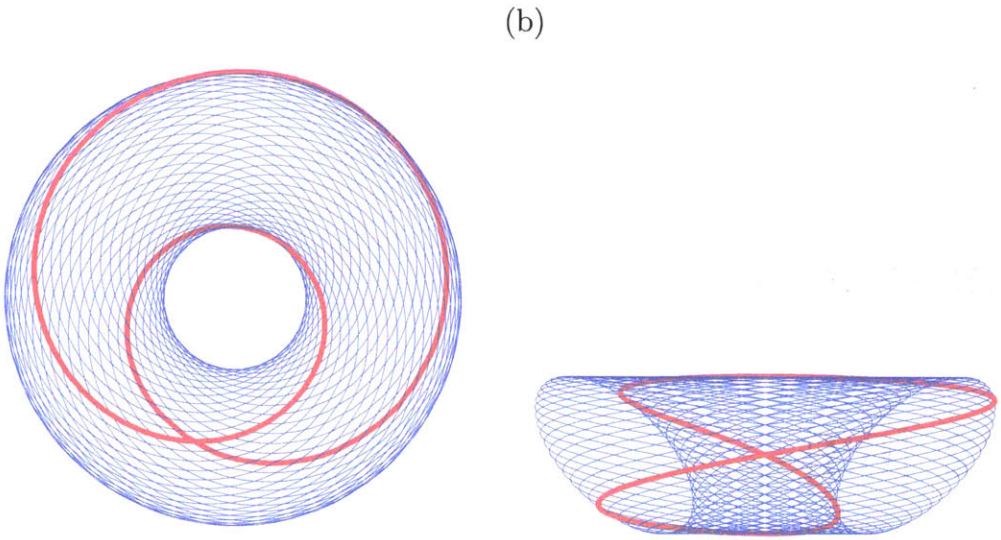

Figure 3-1: Magnetic field lines (blue) from the $q = 2$ flux surface of an example tilted elliptical tokamak with a GS2 flux tube simulation domain (red) viewed from (a) above and (b) the side.

3.1.1 Miller geometry [64]

GS2 allows several different ways of specifying the physical geometry of the simulation. It is able to import numerically generated output from many equilibrium codes such as EFIT [65], TOQ [66, 67], and JSOLVER [68]. The user also has the option of directly specifying the geometry in the input file using either the s-α model [69] or the Miller equilibrium model. This work exclusively uses Miller equilibrium for specifying the simulation geometry (a sample nonlinear input file is included in Appendix C). Many of the conventions and definitions GS2 employs depend on the method of geometry specification. Thus, significant portions of this chapter may only be valid when using Miller geometry.

The traditional Miller equilibrium model is specified by the seven parameters and two normalization parameters listed in table 3.1. Normalization parameters are not specified to the model, but they must be kept consistent between input parameters and when connecting output back to reality. The GS2 implementation of Miller geometry, on the other hand, is specified by nine parameters and two normalization parameters. The extra parameters, R_{geo} and l_r, are redundant and are only present for convenience [70]. The major radial location R_{geo} allows the user to specify the

Quantity	Miller Parameter	GS2 Parameter	GS2 Variable
Minor radius*	ρ	$r_{\psi N} \equiv r_\psi / l_r$	`rhoc`
Ref. magnetic field*†	B_0	B_r	
Major radius	R_0/ρ	$R_{0N} \equiv R_0 / l_r$	`Rmaj`
Shafranov shift	$\frac{1}{\rho}\frac{dR_0}{d\rho}$	$\frac{dR_{0N}}{dr_{\psi N}}$	`shift`
Safety factor	q	q	`qinp`
Magnetic shear	$\frac{dq}{d\rho}$	$\hat{s} \equiv \frac{r_{\psi N}}{q}\frac{dq}{dr_{\psi N}}$	`s_hat_input`
Elongation	κ	κ	`akappa`
Elongation derivative	$\frac{d\kappa}{d\rho}$	$\frac{d\kappa}{dr_{\psi N}}$	`akappri`
Triangularity	δ_M	$\delta \equiv \sin^{-1}(\delta_M)$	`tri`
Triangularity derivative	$\frac{d\delta_M}{d\rho}$	$\frac{d\delta}{dr_{\psi N}}$	`tripri`
Pressure derivative	$\frac{dp}{d\rho}$	$\frac{\beta_T}{p}\frac{dp}{dr_{\psi N}}$	`beta_prime_input`
Magnetic field ref. point		R_{geo}	`R_geo`
Ref. macroscopic length†		l_r	

Table 3.1: Miller and GS2 geometry input parameters, where * denotes a Miller normalization parameter and † denotes a GS2 normalization parameter.

reference magnetic field at any major radial position, instead of forcing the reference magnetic field to be at R_0. The reference length l_r allows the user to use any arbitrary length, such as a meter, to normalize the macroscopic lengths in the simulation, rather than forcing the reference length to be the minor radius. Also, note the quantity r_ψ is a flux function and is used to specify the flux surface, not the traditional radius of circular flux surfaces.

These input parameters are used to create the flux surface of interest and two additional flux surfaces on either side. From this GS2 constructs radial gradients that are used to calculate the poloidal magnetic field. Then, the two additional flux surfaces and all information about the flux surface radial variation is discarded. Finally, using the poloidal field, all radial variation is calculated by ensuring that the Grad-Shafranov equation is locally satisfied [64].

3.1.2 Normalizations

A common source of confusion regarding GS2 arises from the conventions it uses to normalize quantities (see table 3.2). The number of quantities that GS2 accepts as input and prints to output is enormous. This section will primarily discuss those

pertinent to this work.

The reference temperature, used to normalize all temperatures, and the reference thermal velocity are related by $v_{thr} \equiv \sqrt{\frac{2T_r}{m_r}}$. This means the process of normalizing equations frequently creates factors of $\sqrt{2}$ that other normalizations do not have. Also, since the velocity space coordinate normalizations are species dependent, factors of $\sqrt{\frac{T_s}{T_r}}$ and $\sqrt{\frac{m_s}{m_r}}$ can be created. The x and y wavenumbers used in GS2 are related to the ψ and α wavenumbers appearing the gyrokinetic equation as

$$k_\psi \equiv \frac{q}{r_{\psi N}} \frac{k_x}{l_r B_r}, \tag{3.1}$$

$$k_\alpha \equiv \frac{d\psi_N}{dr_{\psi N}} l_r k_y. \tag{3.2}$$

Generally, parameters are normalized to be roughly $O(1)$, so many must be scaled up by $\rho_r \equiv \frac{v_{thr}}{\Omega_r}$, where $\Omega_r \equiv \frac{Z_r e B_r}{m_r}$. The reference temperature, density, and mass are completely arbitrary and left to the user. When using adiabatic electrons, the reference charge is taken to be the elementary charge, otherwise Z_r is also left to the user. The reference magnetic field magnitude is defined as $B_r \equiv \frac{I(\psi)}{R_{geo}}$ on the flux surface of interest. The reference macroscopic length, l_r, is not necessarily the minor radius, but is any arbitrary length, similar to T_r, n_r, and m_r. Lastly, all fluxes are normalized to their gyroBohm values (Γ_{gBr}, Π_{gBr}, and Q_{gBr}), as detailed in Appendix B.

3.2 Code modifications

GS2 needed to be modified to simulate the up-down asymmetric configurations that were investigated in this work. First of all, new input parameters had to be added to the Miller geometry package to allow for a more general geometry specification. Also, for reasons of computation efficiency, several numerical derivatives assumed the up-down symmetry of flux surfaces and the calculation of these numerical derivatives had to be modified. Lastly, in its treatment of trapped particles, GS2 assumed that the poloidal location of the maximum magnetic field was at $\pm\pi$, which is not necessarily

Name	Definition	GS2 Variable
Mass	$m_{Ns} \equiv m_s/m_r$	`mass`
Temperature	$T_{Ns} \equiv T_s/T_r$	`temp`
Charge	$Z_{Ns} \equiv Z_s/Z_r$	`z`
Thermal velocity	$v_{thNs} \equiv v_{ths}/v_{thr} = \sqrt{T_{Ns}/m_{Ns}}$	`stm`
Equilibrium dist. fn.	$F_{MNs} \equiv (v_{ths}^3/n_s)\, F_{Ms}$	
Nonadiabatic dist. fn.	$h_{Ns} \equiv (l_r/\rho_r)\,(1/F_{Ms})\, h_s$	
Complementary dist. fn.	$g_{Ns} \equiv (l_r/\rho_r)\,(1/F_{Ms})\, g_s$	`g`
Perturbed electric potential	$\phi_N \equiv (l_r/\rho_r)\,(e/T_r)\,\phi$	`phi`
Time	$t_N \equiv (v_{thr}/l_r)\, t$	`time`
Parallel velocity	$w_{\|\|N} \equiv w_{\|\|}/v_{ths}$	`vpa`
Perp. velocity squared	$w_{\perp N}^2 \equiv w_\perp^2/v_{ths}^2$	`vperp2`
Radial perp. coordinate	$x_N \equiv x/\rho_r$	
Poloidal perp. coordinate	$y_N \equiv y/\rho_r$	
Parallel wavenumber	$k_{\|\|N} \equiv l_r k_{\|\|}$	
Major radial coordinate	$R_N \equiv R/l_r$	`Rpos`
Vertical coordinate	$Z_N \equiv Z/l_r$	`Zpos`
Radial perp. wavenumber	$k_{xN} \equiv \rho_r k_x$	`akx`
Poloidal perp. wavenumber	$k_{yN} \equiv \rho_r k_y$	`aky`
Magnetic field magnitude	$B_N \equiv B/B_r$	`bmag`
Magnetic flux	$\psi_N \equiv \psi/\,(l_r^2 B_r)$	
Current	$I_N \equiv I/\,(l_r B_r)$	
Flow	$u_{\zeta N} \equiv \frac{u_\zeta}{v_{thr}} = \frac{R\Omega_\zeta}{v_{thr}}$	
Angular flow	$\Omega_{\zeta N} \equiv (l_r/v_{thr})\,\Omega_\zeta = u_{\zeta N}/R_N$	`mach`
Angular flow shear	$\gamma_{EN} \equiv (a/v_{thr})\,\gamma_E = \frac{r_{\psi N}}{q}\frac{d\Omega_{\zeta N}}{dr_{\psi N}}$	`g_exb`
Energy	$\mathscr{E}_N \equiv \mathscr{E}/T_s$	`energy`
Magnetic moment	$\mu_N \equiv \frac{1}{2}\,(B_r/T_s)\,\mu$	
Lambda	$\lambda_N \equiv \mu_N/\mathscr{E}_N$	`l`
Density	$n_{Ns} \equiv n_s/n_r$	`dens`
Temperature gradient	$1/L_{TNs} \equiv l_r/L_{Ts} = -\frac{l_r}{T_s}\frac{\partial T_s}{\partial r_\psi}$	`tprim`
Density gradient	$1/L_{nNs} \equiv l_r/L_{ns} = -\frac{l_r}{n_s}\frac{\partial n_s}{\partial r_\psi}$	`fprim`
Mode angular frequency	$\omega_N \equiv (l_r/v_{thr})\,\mathrm{Real}\,[\omega]$	`omega`
Mode growth rate	$\gamma_N \equiv (l_r/v_{thr})\,\mathrm{Imag}\,[\omega]$	`omega`
Particle flux	$\Gamma_{Ns} \equiv \Gamma_s/\Gamma_{gBr}$	`part_fluxes`
Angular momentum flux	$\Pi_{Ns} \equiv \Pi_s/\Pi_{gBr}$	`mom_fluxes`
Heat flux	$Q_{Ns} \equiv Q_s/Q_{gBr}$	`heat_fluxes`

Table 3.2: GS2 normalized quantities and their corresponding variable names within the code (table adapted from ref. [20]).

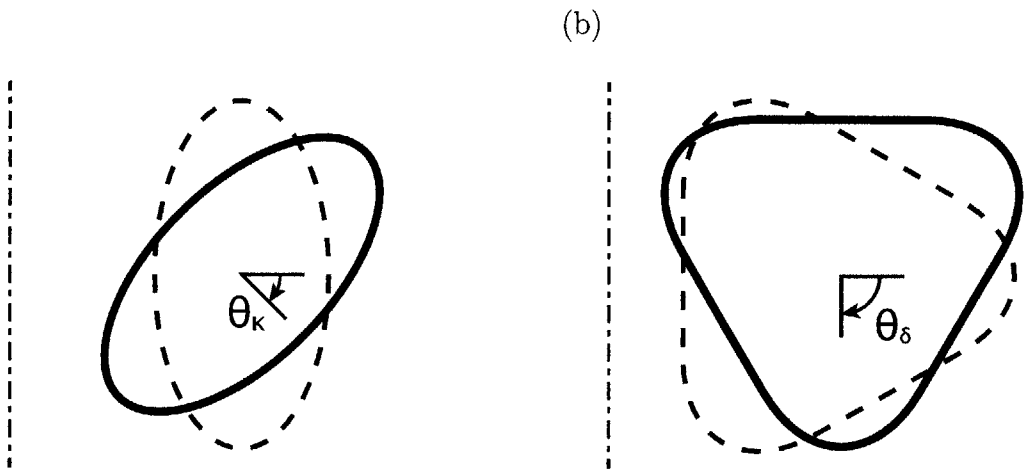

Figure 3-2: Definition of the (a) elongation tilt angle, θ_κ, and (b) triangularity tilt angle, θ_δ, parameters.

Name	Definition	GS2 Variable
Elongation tilt angle	θ_κ	`thetak`
Elongation tilt angle derivative	$\frac{d\theta_\kappa}{dr_{\psi N}}$	`thetakp`
Triangularity tilt angle	θ_δ	`thetad`
Triangularity tilt angle derivative	$\frac{d\theta_\delta}{dr_{\psi N}}$	`thetadp`

Table 3.3: New GS2 input quantities and their corresponding variable names.

the case for up-down asymmetric flux surfaces.

3.2.1 Geometry specification

Originally, GS2 Miller geometry input allowed for flux surface elongation and triangularity, but was not general enough to allow for tilted shapes. To support modeling up-down asymmetry four additional input parameters were added, given in table 3.3. The elongation tilt angle and the triangularity tilt angle, shown in fig. 3-2, both have intuitively obvious definitions and can be varied independently. This allows significant additional flexibility in modeling unusual geometries, such as tilted comet-shaped flux surfaces [71].

The Miller equilibrium flux surface shape specification is given in the source file

`leq.f90`. Formerly, the flux surfaces were defined by

$$R_N^{old}\left(r_{\psi N},\vartheta\right)=R_{0N}\left(r_{\psi N}\right)+r_{\psi N}\cos\left(\vartheta+\delta\left(r_{\psi N}\right)\sin\left(\vartheta-\frac{\pi}{2}a_{sym}\right)\right), \tag{3.3}$$

$$Z_N^{old}\left(r_{\psi N},\vartheta\right)=r_{\psi N}\kappa\left(r_{\psi N}\right)\sin\left(\vartheta\right). \tag{3.4}$$

Note the appearance of the parameter a_{sym}, which has not yet been mentioned. The actual GS2 implementation includes two parameters, `asym` and `asympri`, which appear in the equations and create a divertor-like up-down asymmetric geometry. However, because of issues concerning numerical differentiation (see Section 3.2.2) and the location of the maximum magnetic field (see Section 3.2.3), simulations including a nonzero a_{sym} never functioned properly. The angle ϑ is distinguished from the angle θ, used in Chapter 2, because it is not the usual cylindrical poloidal angle. From eqs. (3.3) and (3.4), the two neighboring flux surfaces were created using a Taylor expansion about the flux surface of interest $r_{\psi N}$. The definition of the neighboring flux surfaces is what necessitates providing input for the Shafranov shift, elongation derivative, and triangularity derivative.

The new, more general specification is done by adding each of the shaping effects in and rotating the appropriate angle. The new definition is

$$\vartheta'\equiv\vartheta+\vartheta_{shift}, \tag{3.5}$$

$$R_c\left(r_{\psi N},\vartheta\right)\equiv r_{\psi N}\cos\left(\vartheta'+\theta_\kappa\left(r_{\psi N}\right)-\theta_\delta\left(r_{\psi N}\right)\right), \tag{3.6}$$

$$Z_c\left(r_{\psi N},\vartheta\right)\equiv r_{\psi N}\sin\left(\vartheta'+\theta_\kappa\left(r_{\psi N}\right)-\theta_\delta\left(r_{\psi N}\right)\right), \tag{3.7}$$

$$R_\kappa\left(r_{\psi N},\vartheta\right)\equiv R_c\left(r_{\psi N},\vartheta\right), \tag{3.8}$$

$$Z_\kappa\left(r_{\psi N},\vartheta\right)\equiv Z_c\left(r_{\psi N},\vartheta\right)+\left(\kappa\left(r_{\psi N}\right)-1\right)r_{\psi N}\sin\left(\vartheta'+\theta_\kappa\left(r_{\psi N}\right)-\theta_\delta\left(r_{\psi N}\right)\right), \tag{3.9}$$

$$R_{\kappa}^{tilt}\left(r_{\psi N},\vartheta\right) \equiv R_{\kappa}\left(r_{\psi N},\vartheta\right)\cos\left(\theta_{\kappa}\left(r_{\psi N}\right)-\theta_{\delta}\left(r_{\psi N}\right)\right) + Z_{\kappa}\left(r_{\psi N},\vartheta\right)\sin\left(\theta_{\kappa}\left(r_{\psi N}\right)-\theta_{\delta}\left(r_{\psi N}\right)\right), \tag{3.10}$$

$$Z_{\kappa}^{tilt}\left(r_{\psi N},\vartheta\right) \equiv Z_{\kappa}\left(r_{\psi N},\vartheta\right)\cos\left(\theta_{\kappa}\left(r_{\psi N}\right)-\theta_{\delta}\left(r_{\psi N}\right)\right) - R_{\kappa}\left(r_{\psi N},\vartheta\right)\sin\left(\theta_{\kappa}\left(r_{\psi N}\right)-\theta_{\delta}\left(r_{\psi N}\right)\right), \tag{3.11}$$

$$R_{\delta}\left(r_{\psi N},\vartheta\right) \equiv R_{\kappa}^{tilt}\left(r_{\psi N},\vartheta\right) + r_{\psi N}\left[\cos\left(\vartheta' + \delta\sin\left(\vartheta'\right)\right) - \cos\left(\vartheta'\right)\right], \tag{3.12}$$

$$Z_{\delta}\left(r_{\psi N},\vartheta\right) \equiv Z_{\kappa}^{tilt}\left(r_{\psi N},\vartheta\right), \tag{3.13}$$

$$R_{\delta}^{tilt}\left(r_{\psi N},\vartheta\right) \equiv R_{\delta}\left(r_{\psi N},\vartheta\right)\cos\left(\theta_{\delta}\left(r_{\psi N}\right)\right) + Z_{\delta}\left(r_{\psi N},\vartheta\right)\sin\left(\theta_{\delta}\left(r_{\psi N}\right)\right), \tag{3.14}$$

$$Z_{\delta}^{tilt}\left(r_{\psi N},\vartheta\right) \equiv Z_{\delta}\left(r_{\psi N},\vartheta\right)\cos\left(\theta_{\delta}\left(r_{\psi N}\right)\right) - R_{\delta}\left(r_{\psi N},\vartheta\right)\sin\left(\theta_{\delta}\left(r_{\psi N}\right)\right), \tag{3.15}$$

$$R_{N}^{new}\left(r_{\psi N},\vartheta\right) = R_{0N}\left(r_{\psi N}\right) + R_{\delta}^{tilt}\left(r_{\psi N},\vartheta\right), \tag{3.16}$$

$$Z_{N}^{new}\left(r_{\psi N},\vartheta\right) = Z_{\delta}^{tilt}\left(r_{\psi N},\vartheta\right). \tag{3.17}$$

Fig. 3-3 shows each step of this geometry specification process. Note that $\delta \in \left(-\frac{\pi}{2},\frac{\pi}{2}\right)$, as indicated by the definition in table 3.1. If δ is specified outside this range the flux surface cross-section can develop singular points. As before, calculating the poloidal magnetic field still requires the radial derivatives of the input parameters appearing in the flux surface specification. The translation of ϑ by $\theta_{\kappa}\left(r_{\psi N}\right)-\theta_{\delta}\left(r_{\psi N}\right)$ only serves to get the proper phase between the effects of elongation and triangularity. The ϑ_{shift} parameter ultimately determines the location of $\vartheta = 0$ and will be discussed in Section 3.2.3. In this thesis, all radial derivatives appearing in tables 3.1 and 3.3, excepting the magnetic shear, are set to zero.

3.2.2 Numerical differentiation

Within the `leq.f90` source file there are several numerical derivatives taken using the parameterized flux surfaces. Originally, these derivatives were taken over the $\vartheta \in [0,\pi]$ domain and later copied, with the proper symmetry, to the $\vartheta \in (0,-\pi]$ domain. For

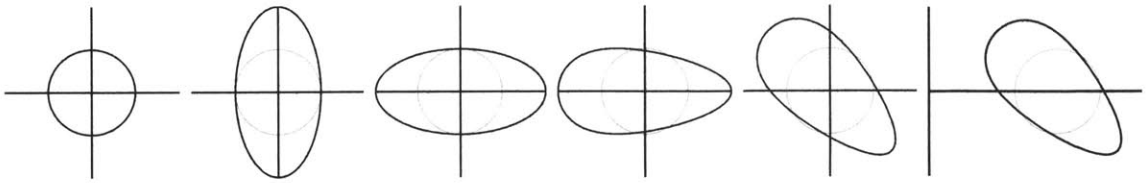

Figure 3-3: Demonstration of each stage of the iterative method (eqs. (3.6) through (3.17)) to specify geometry with $R_{0N} = 3$, $r_{\psi N} = 1$, $\kappa = 2$, $\delta = 0.7$, $\theta_\kappa = \frac{3}{4}\pi$, and $\theta_\delta = \frac{1}{4}\pi$.

modeling up-down asymmetric geometries, these subroutines were converted to use the $\vartheta \in [-\pi, \pi]$ domain throughout the entire algorithm.

3.2.3 Treatment of bounce points

A more subtle issue stems from GS2's treatment of trapped particles. The gridder is a particularly dense and unintelligible portion of the code that is contained in `gridgen4mod.f90`. It is responsible for taking the input geometry and discretizing the spatial and velocity dimensions. The poloidal and velocity grids are structured so that particles have velocities such that they only ever bounce at grid points and not between grid points. To do this, the gridder assumes that the location of the maximum total magnetic field is at $\vartheta = \pm\pi$. However, this is not automatically the case for up-down asymmetric configurations.

Rather than attempt to understand and modify the inner workings of the gridder, the definition of ϑ was translated by the quantity $\vartheta_{shift} \equiv \pm\pi - \vartheta_{B_{max}}$, where $\vartheta_{B_{max}}$ is the location of the maximum of B in the flux surface. Therefore, the assumption is always satisfied. However, the location of the maximum magnetic field, $\vartheta_{B_{max}}$, in a general flux surface with separately tilted elongation and triangularity is not analytic. So, for the sake of convenience, this was implemented in GS2 as a two step process. First, the geometry is discretized and $B(\vartheta)$ is calculated with $\vartheta_{shift} = 0$, as was already the case. Then the code searches through all the values of ϑ and finds $\vartheta_{B_{max}}$. If $\vartheta_{B_{max}} = \pm\pi$, the code moves forwards. Otherwise, ϑ_{shift} is set accordingly and the initialization routine is started from the beginning a second time.

3.3 Code benchmarking

Several different tests were used to verify that the modifications to GS2 introduced no errors and that no further modifications were necessary to properly treat up-down asymmetry. First, a collisionless linear analytic solution to the gyrokinetic equation (with $k_\alpha = 0$) was found and compared to GS2 output. Also, the new input parameters added to the code allow a physical geometry to be specified in different ways. These different specifications were tested to ensure that they produced equivalent results. Lastly, all effects of the system geometry appear in the gyrokinetic as eight individual coefficients. Several of these were calculated independently and compared against those calculated within GS2.

3.3.1 Stationary mode test

The stationary mode test case is a comparison between the conclusions of an analytic calculation and GS2 results. The analytic calculation starts with the Fourier analyzed gyrokinetic equation (see eq. (1.21)). Now we choose to focus on modes with $k_\alpha = 0$ and ignore collisions. These two conditions can be enforced in GS2 by setting `aky` $= 0$ and `collision_model` $=$ `'none'`. Next, we postulate that time-independent solutions for h_s and ϕ exist and seek them by letting $\frac{\partial}{\partial t} = 0$. These simplifications, along with changing velocity space variables $\left(w_{||}, \mu, \varphi\right) \rightarrow \left(\mathscr{E}, \mu, \varphi\right)$, gives

$$w_{||} \left.\frac{\partial h_s}{\partial \vartheta}\right|_{\mathscr{E},\mu} = i\frac{k_\psi I}{\Omega_s B}\left(w_{||}^2 + \mu B\right)\frac{\partial B}{\partial \vartheta} h_s. \tag{3.18}$$

Solving for the nonadiabatic distribution function we find that

$$h_s\left(k_\psi, \vartheta, \mathscr{E}, \mu\right) = h_{s0}\left(k_\psi, \mathscr{E}, \mu\right) \exp\left(-i\frac{k_\psi w_{||}}{\Omega_s} I\right), \tag{3.19}$$

where we choose the integration constant to be $h_{s0} = Z_s \frac{\rho_r}{l_r} F_{Ms}$. The factor of Z_s is added for numerical reasons that will be discussed later and $\frac{\rho_r}{l_r} F_{Ms}$ is chosen for proper normalization according to table 3.2. Now we substitute this result into the quasineutrality equation, given by eq. (1.22). Solving for the perturbed electric

potential, using the identity

$$J_0(z) = \frac{1}{2\pi} \oint_0^{2\pi} d\varphi \exp(iz\sin\varphi) \tag{3.20}$$

and the change of integration variables $(w_{||}, \mu, \varphi) \rightarrow (w_{||}, w_x, w_y)$, we find

$$\phi = \left(\sum_s \frac{Z_s^2 e n_s}{T_s} \right)^{-1} \frac{\rho_r}{l_r} \sum_s n_s Z_s^2 \exp\left(-\frac{1}{2} \frac{k_\psi^2}{\Omega_s^2} R^2 B^2 \frac{T_s}{m_s} \right). \tag{3.21}$$

Now we can use the normalizations of table 3.2 and the definition of the complementary distribution function

$$g_s \equiv h_s - \frac{Z_s e}{T_s} J_0\left(\frac{k_\perp \sqrt{2\mu B}}{\Omega_s} \right) \phi F_{Ms}, \tag{3.22}$$

the distribution function that GS2 actually manipulates internally, to find

$$\begin{aligned} g_{Ns} = {} & Z_{Ns} \exp\left(-i \frac{q}{\rho} k_{xN} w_{||N} R_{geoN} \frac{\sqrt{m_{Ns} T_{Ns}}}{Z_{Ns} B_N} \right) \\ & - \frac{Z_{Ns}}{T_{Ns}} J_0\left(k_{\perp N} w_{\perp N} \frac{\sqrt{m_{Ns} T_{Ns}}}{Z_{Ns} B_N} \right) \phi_N \end{aligned} \tag{3.23}$$

and

$$\phi_N = \left(\sum_j \frac{Z_{Nj}^2 n_{Nj}}{T_{Nj}} \right)^{-1} \sum_k n_{Nk} Z_{Nk}^2 \exp\left(-\frac{1}{4} \frac{q^2}{\rho^2} k_{xN}^2 R_N^2 \frac{m_{Nk} T_{Nk}}{Z_{Ns}^2} \right). \tag{3.24}$$

Therefore if we initialize the distribution function to eq. (3.23), we expect the calculated potential at every grid point in ϑ to match eq. (3.24) and neither quantity to change in time. To quantify the time independence, at each poloidal grid point, we first calculate the fractional error between eq. (3.24) and the calculated potential distribution after 500 GS2 time steps of $0.1\frac{l_r}{v_{thr}}$. From the fractional error at every ϑ grid point, the standard deviation, σ_{err}, is calculated, producing a single number that indicates if a given GS2 run is treating geometrical effects correctly.

Initially, the factor of Z_s was not included in the integration constant of eq. (3.19),

causing the summations over species in eq. (3.24) to become a differences between the ion and electron terms. Depending on the argument of the exponent, this caused numerical errors to dominate and prevented all distribution functions from maintaining a stationary state. Introducing the factor of Z_s into the integration constant of eq. (3.19) keeps this cancellation from occurring and makes the problem better conditioned.

A total of 70 simulations were run for the test, consisting of five groups of seven simulations for both the original and updated versions of the code. All simulations were performed at very high spatial (`ntheta` $= 128$) and velocity space (`negrid` $= 32$, `ngauss` $= 10$) resolution and were shaped variants of the Cyclone base case geometry given in table 4.1. The Cyclone base case is the standard geometry used in tokamak simulations [3] and is modeled after a particular DIII-D shot. The a_{sym} parameter (discussed in Section 3.2.1) was used to create improperly treated up-down asymmetry in the original code as a control for the test. Within each group of seven simulations, the only difference was the radial wavenumber, $k_{xN} \in \{0.1, 0.3, 0.5, 0.7, 0.9, 1.1, 1.3\}$.

The five groups of simulations performed with the original source code consisted of a circular cross-section and four triangular shapes with $\delta = 0.7$ and $a_{sym} \in \{0.0, 0.4, 0.7, 1.0\}$. Therefore, three of these groups are up-down asymmetric and should fail to maintain the stationary state.

The five groups of simulations performed with the updated source code include a circular cross-section and four elongated shapes with $\kappa = 2$ and $\theta_\kappa \in \left\{0, \frac{\pi}{6}, \frac{\pi}{3}, \frac{\pi}{2}\right\}$. Therefore, two of these groups are up-down asymmetric, but, because of the updates, all should still maintain the stationary state.

The results, summarized in fig. 3-4, were as expected. Fig. 3-4a shows that the two codes produce nearly identical results for identical circular flux surfaces. Fig. 3-4b shows a clear separation between the results of improperly treated up-down asymmetric runs using the original source code and all other runs. The up-down asymmetric runs using the updated version of the code have very similar error to the up-down symmetric runs. Furthermore, fig. 3-5 shows that the improperly treated

(a)

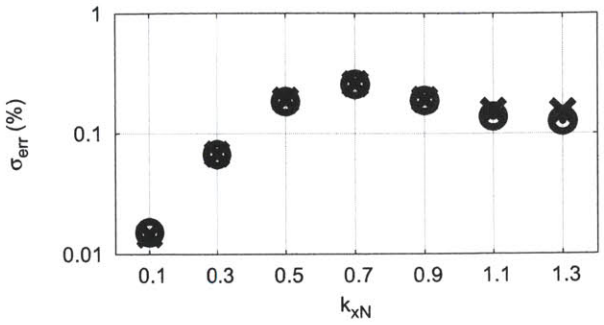

(b)

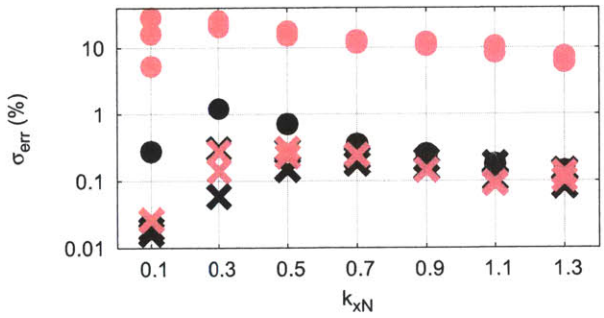

Figure 3-4: Stationary state test case error for both up-down symmetric (black) and up-down asymmetric (red) configurations performed using the original source code (circles) and the updated source code (crosses) for (a) circular flux surfaces or (b) shaped flux surfaces.

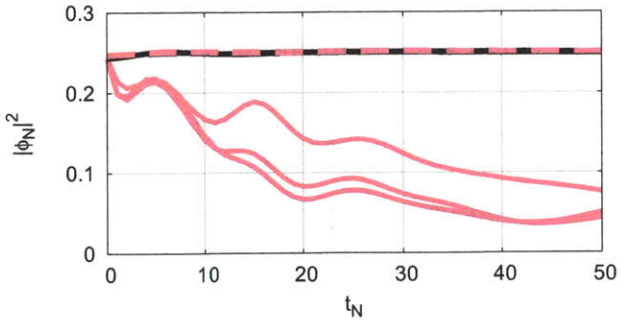

Figure 3-5: The potential amplitude with time for both up-down symmetric (black) and up-down asymmetric (red) configurations performed using the original source code (solid) and the updated source code (dotted). Only the test cases with $k_{xN} = 0.7$ are shown.

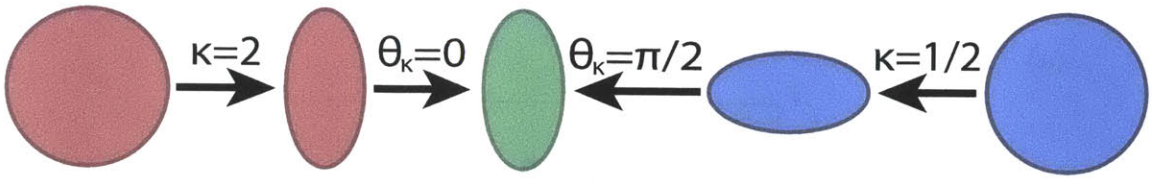

Figure 3-6: An example of two different GS2 specifications of the same physical geometry.

up-down asymmetric cases converge to different steady-state solutions than all of the other cases.

3.3.2 Duplicate geometry test

As illustrated in fig. 3-6 , the addition of the tilt parameters allows for multiple ways to specify the same physical geometry. Both these manners of specification should produce the same results. However, getting this test to work requires a comprehensive understanding of GS2's normalizations of input and output parameters. Given an arbitrary elongated configuration with no triangularity (indicated by a subscript 1), we can produce a physically identical configuration (indicated by a subscript 2) with a different GS2 specification using

$$\texttt{akappa}_2 = \frac{1}{\texttt{akappa}_1}, \tag{3.25}$$

$$\texttt{thetak}_2 = \texttt{thetak}_1 + \frac{\pi}{2}, \tag{3.26}$$

$$\texttt{tprim}_2 = \frac{1}{\texttt{akappa}_1}\texttt{tprim}_1, \tag{3.27}$$

$$\texttt{fprim}_2 = \frac{1}{\texttt{akappa}_1}\texttt{fprim}_1, \tag{3.28}$$

$$\texttt{akx}_2 = \texttt{akappa}_1\texttt{akx}_1, \tag{3.29}$$

$$\texttt{aky}_2 = \texttt{akappa}_1\texttt{aky}_1, \tag{3.30}$$

$$\texttt{gds22}_2 = (\texttt{akappa}_1)^2\,\texttt{gds22}_1, \tag{3.31}$$

$$\texttt{gds21}_2 = (\texttt{akappa}_1)^2\,\texttt{gds21}_1, \tag{3.32}$$

$$\texttt{gds2}_2 = (\texttt{akappa}_1)^2\,\texttt{gds2}_1 \tag{3.33}$$

where $\texttt{gds22} \equiv \left(\frac{dq_s}{dr_{\psi N}}\right)^2 \left|\vec{\nabla}_N \psi_N\right|^2$, $\texttt{gds21} \equiv \frac{dq_s}{dr_{\psi N}} \frac{d\psi_N}{dr_{\psi N}} \vec{\nabla}_N \psi_N \cdot \vec{\nabla}_N \alpha$, and $\texttt{gds2} \equiv \left(\frac{d\psi_N}{dr_{\psi N}}\right)^2 \left|\vec{\nabla}_N \alpha\right|^2$ are GS2 outputs. The factors of $\texttt{akappa}_1$ arise in eqs. (3.27) through (3.33) because GS2 chooses $\left|\vec{\nabla}\psi\right|$ at the midplane of the ellipse before rotation to normalize quantities such as k_ψ and k_α. The value of $\left|\vec{\nabla}\psi\right|$ used for normalizations is different for the two configurations. An analogous transformation exists for triangular flux surfaces with no elongation, given by

$$\texttt{tri}_2 = -\texttt{tri}_1, \tag{3.34}$$

$$\texttt{thetad}_2 = \texttt{thetad}_1 + \pi, \tag{3.35}$$

$$\texttt{tprim}_2 = \texttt{tprim}_1, \tag{3.36}$$

$$\texttt{fprim}_2 = \texttt{fprim}_1, \tag{3.37}$$

$$\texttt{akx}_2 = \texttt{akx}_1, \tag{3.38}$$

$$\texttt{aky}_2 = \texttt{aky}_1, \tag{3.39}$$

$$\texttt{gds22}_2 = \texttt{gds22}_1, \tag{3.40}$$

$$\texttt{gds21}_2 = \texttt{gds21}_1, \tag{3.41}$$

$$\texttt{gds2}_2 = \texttt{gds2}_1. \tag{3.42}$$

Two elongated cases, one unrotated and one rotated, were run linearly for $k_x = 0$ and $k_y \neq 0$ in order to test a parameter space missed by the stationary state test (where $k_y = 0$). As expected, fig. 3-7 shows that these two configurations both produce identical geometric coefficients as well as converge to the same linear growth rate and mode shape.

Also, elongated test cases were run for a large number of nonlinearly interacting modes. Because of the fluctuating nature of nonlinear runs we only expect the two results to behave identically in the statistical sense. We can see in fig. 3-8 that the heat fluxes are identical through the linear growth phase (up to $t_N \sim 20$). Afterwards, during the nonlinear saturation, we see the results diverge, but still saturate at the same level, when averaged in time.

(a)

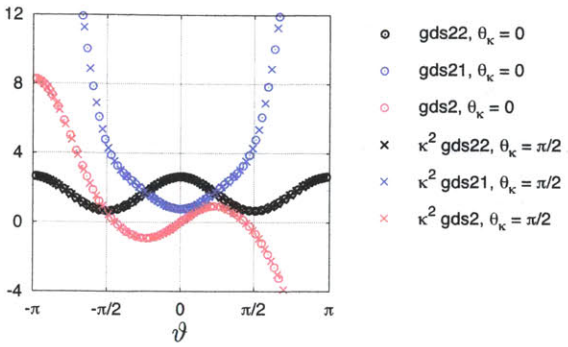

(b)

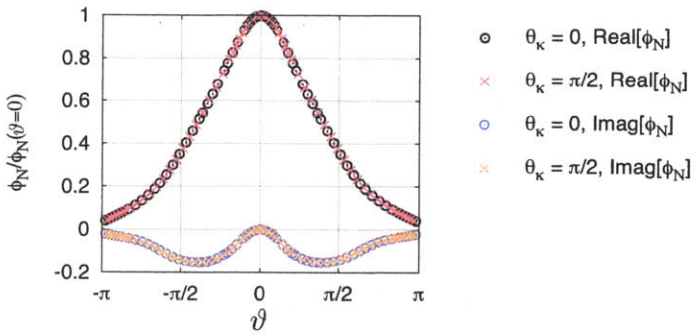

Figure 3-7: Comparison of (a) geometric coefficients and (b) potential for the two geometric specifications with $\omega_N = 0.2727 + 0.2907i$ for $\theta_\kappa = 0$ and $\omega_N = 0.2727 + 0.2908i$ for $\theta_\kappa = \pi/2$.

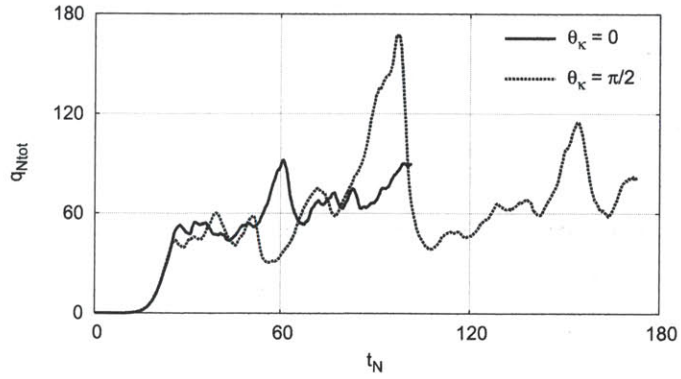

Figure 3-8: Comparison of total heat flux for the two geometric specifications.

3.3.3 Geometric coefficient test

Lastly, all effects of the system geometry appear in the equations governing gyrokinetics (eqs. (1.21) through (1.30)) as eight individual coefficients: B, $\frac{\partial B}{\partial \vartheta}$, $\frac{\partial B}{\partial \psi}$, $\hat{b} \cdot \vec{\nabla}\vartheta$, $\hat{b} \cdot \left(\vec{\nabla}\vartheta \times \vec{\nabla}\alpha\right)$, $\left|\vec{\nabla}\psi\right|^2$, $\vec{\nabla}\psi \cdot \vec{\nabla}\alpha$, and $\left|\vec{\nabla}\alpha\right|^2$. The final test performed was to verify that the geometric coefficients were correct for up-down asymmetric configurations. A numerical calculation, completely independent of GS2, was performed which found the coefficients using the Miller equilibrium model. Fig. 3-9 shows excellent agreement between the four coefficients that were compared.

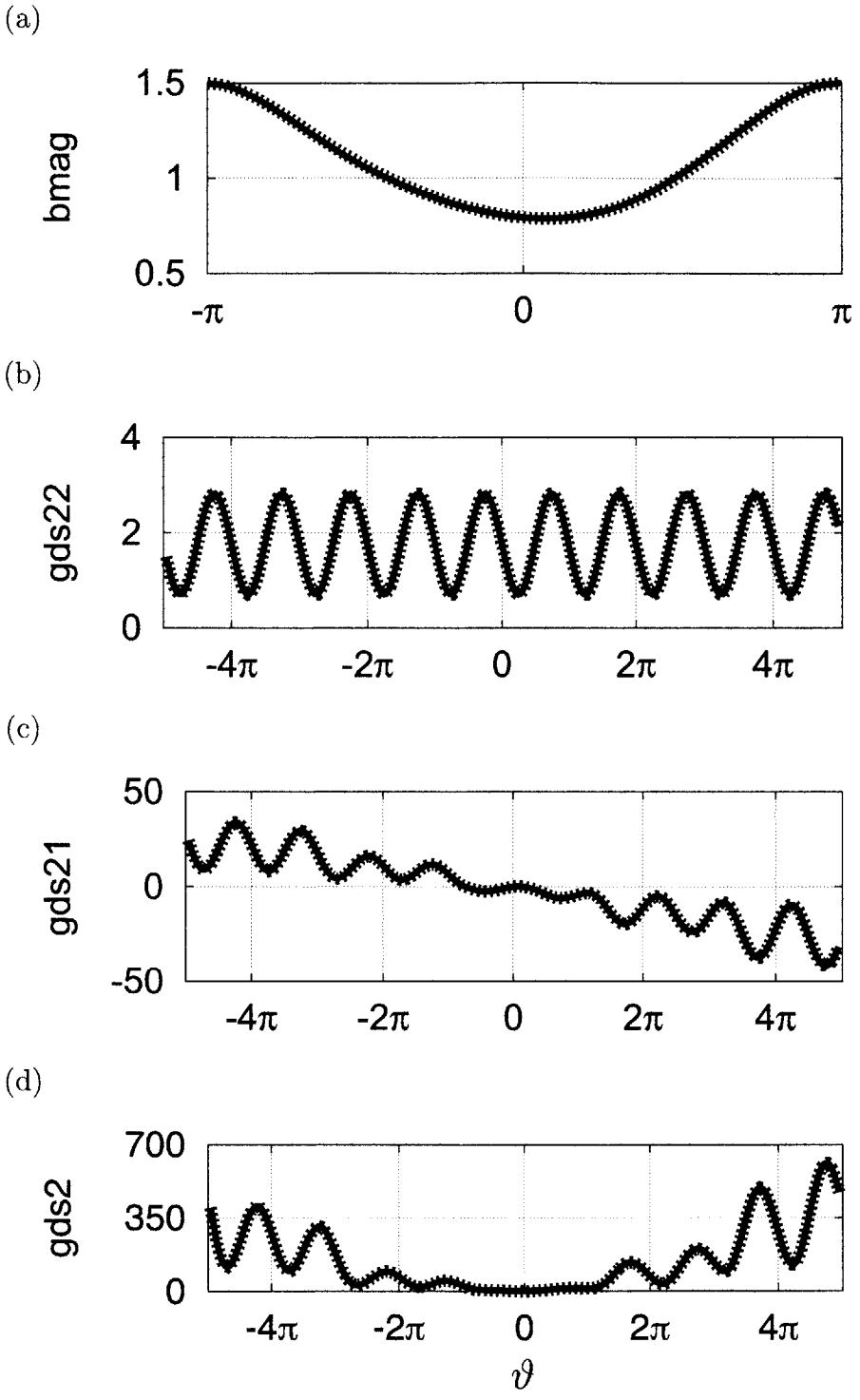

Figure 3-9: Geometrical coefficients output by GS2 (solid) and an independent numerical calculation (dotted) for elongated flux surfaces with $\theta_\kappa = \frac{\pi}{6}$.

Chapter 4

Energy transport

Modifying the poloidal cross-section affects nearly every aspect of tokamak performance, not just the level of intrinsic rotation. In fact, the viability of a tilted elliptical tokamak as a reactor ultimately depends on energy confinement properties. For this reason, we will investigate how turbulent energy transport and reactor design limits are affected by elongation tilt in several different geometries, which are all variants of the Cyclone base case. Furthermore, we will see that the precise manner by which the flux surfaces are rotated is important. The different elliptical shapes and plasma parameters (geometries) used are given in table 4.1 and the different ways to rotate these elliptical flux surfaces (transformations) used are given in table 4.2.

First we will describe the GS2 simulations performed and present the results. Importantly we will see that in some cases elongation tilt can dramatically reduce turbulent energy transport. Then we will look at how several different local parame-

Cyclone case name	$r_{\psi N}$	R_{0N}	q	$\hat{s}$	$1/L_{TNs}$	$1/L_{nNs}$	κ	δ
Base [3]	0.54	3	1.4	0.8	2.3	0.733	1	0
Elongated	0.54	3	1.4	0.8	2.3	0.733	2	0
Elongated Extreme	0.54	3	1.4	0.8	3.45	0.733	2	0
Optimized Elongated	1	3	1.4	0.8	2.5	0.733	2	0
Triangular Extreme	1	3	1.4	0.8	3.5	1	1	0.7

Table 4.1: Normalized unrotated input parameters for the geometry of each Cyclone base case variant, all with $m_{Ni} = 1$, $m_{Ne} = 2.7 \times 10^{-4}$, $T_{Ns} = 1$ and $n_{Ns} = 1$, where $s \in \{i, e\}$.

Transformation name	R	B	L_{Ts}	L_{ns}	Size
Simplistic	R_{0N}	B_{0N}	$L_{TNs}(r_{min})$	$L_{nNs}(r_{min})$	$r_{\psi N}$
Sophisticated	R_{minN}	$B_{\zeta N}(R_{minN})$	$L_{TNs}(R_{maxN})$	$L_{nNs}(R_{maxN})$	$r_{\psi N}$
Realistic	R_{minN}	$B_{\zeta N}(R_{minN})$	$L_{TNs}(r_{min})$	$L_{nNs}(r_{min})$	$r_{\psi N}$
Constant-cost	R_{minN}	$B_{\zeta N}(R_{minN})$	$L_{TNs}(r_{min})$	$L_{nNs}(r_{min})$	V_N

Table 4.2: Summary of the parameters kept fixed during different transformations used to compare tilted elliptical configurations, where $s \in \{i, e\}$ and $V_N = 2\pi R_{0N}\pi r_{\psi N}^2 \kappa$.

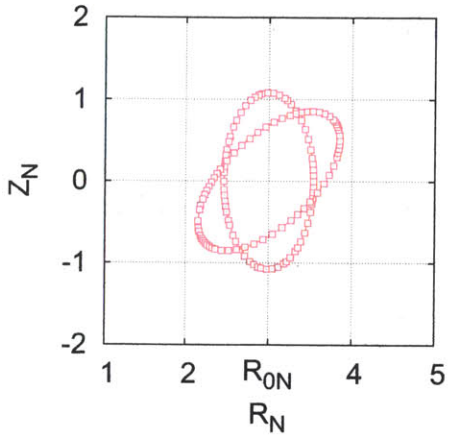

Figure 4-1: Elongated Cyclone base case at $\theta_\kappa = \{0, \frac{\pi}{4}\}$ with the Simplistic transformation.

ters change with elongation tilt to see if any have a clear connection with the observed suppression of turbulence. Finally we will evaluate the implications for the reactor viability of tilted elliptical tokamaks.

4.1 Nonlinear simulations

In this section we will discuss three sets of nonlinear simulations: the Elongated geometry with the Simplistic transformation (see fig. 4-1), the Elongated Extreme geometry with the Simplistic transformation (see fig. 4-3), and the Optimized Elongated geometry with the Sophisticated transformation (see fig. 4-6).

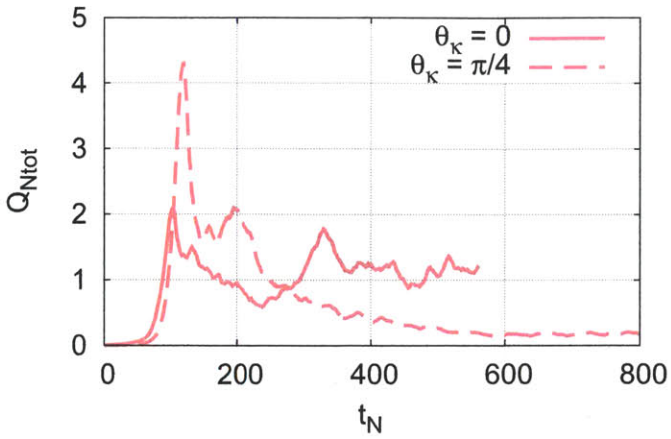

Figure 4-2: Total nonlinear heat flux time trace for the Elongated Cyclone base case with the Simplistic transformation.

4.1.1 Elongated geometry with the Simplistic transformation

Fundamentally, when we compare the relative merits of different tokamak configurations, we want cost to be invariant. However, it is unclear how to translate cost into the global parameters appearing in tokamak design limits, let alone the local flux surface parameters that GS2 requires. If we take the GS2 input file for the Elongated cyclone base case geometry and change only the parameter `thetak` from 0 to $\frac{\pi}{4}$ we produce the two configurations appearing in fig. 4-1. This transformation implicitly holds the major radius, the on-axis magnetic field, and the background gradients at the pre-rotation midplane (i.e. the location of the minimum minor radial position, r_{min}) constant as the ellipse is rotated. This seems to be a fairly good method because it keeps the total plasma volume constant as well as the peak temperatures and densities (if we extrapolate the gradients to the magnetic axis). However it alters the amount of available space on the inboard side for structure and increases the required on-coil magnetic field. The required on-coil magnetic field increases because B_0 is fixed and the distance between R_0 and R_{min} increases with elongation rotation.

The transformation also has an unexpected and fairly drastic effect on turbulence. Fig. 4-2 shows that rotation by $\frac{\pi}{4}$ suppresses the turbulent transport of energy by a factor of 10! We suspect this may be because, near the regions of high poloidal curva-

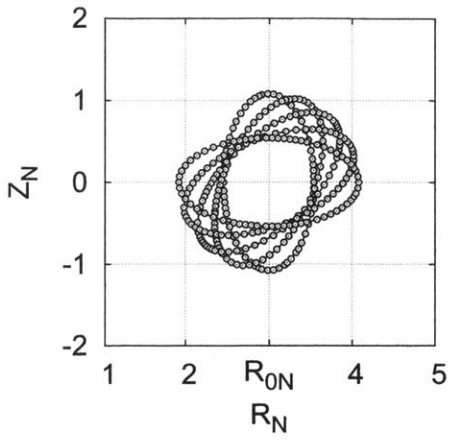

Figure 4-3: Elongated Extreme Cyclone base case at $\theta_\kappa = \{0, \frac{\pi}{8}, \frac{\pi}{4}, \frac{3\pi}{8}, \frac{\pi}{2}\}$ with the Simplistic transformation.

ture, the poloidal magnetic field weakens and the flux surfaces become spaced further apart. Tilting the elongation weakens the background gradients near the location of the strongest turbulence drive (near the point of maximum R). Additionally, tilting the flux surfaces has stabilizing consequences that arise from the value of the magnetic field curvature at the location of the mode. These influences will be discussed in more depth later in this chapter.

4.1.2 Elongated Extreme geometry with the Simplistic transformation

We suspected the apparent stabilization in fig. 4-2 might skew momentum flux results, so the geometry was repeated with a 50% increase in the background temperature gradient. This produced the Elongated Extreme geometry in fig. 4-3. We see from fig. 4-4 these simulations did not display turbulent stabilization with elongation rotation. It seems that this stabilizing effect vanishes with stronger gradients. Linear simulations, shown in fig. 4-5, agree with this result. However, at this point it is unclear whether typical experimental values for the temperature gradient lie in the parameter space that sees turbulent stabilization from tilt and how this effect changes with elongation. Nevertheless, the factor of 10 reduction in energy transport

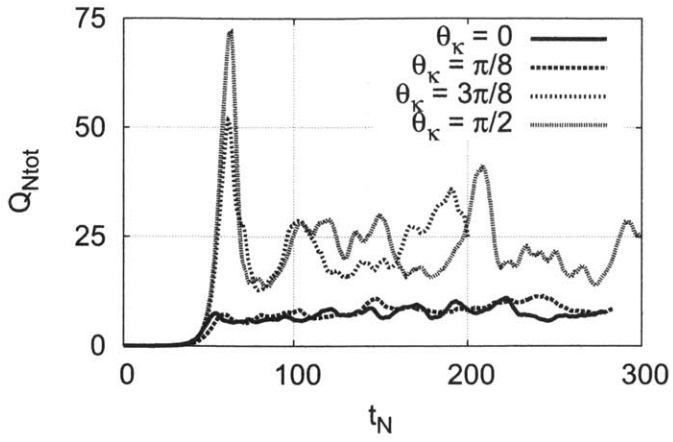

Figure 4-4: Total nonlinear heat flux time trace for the Elongated Extreme Cyclone base case with the Simplistic transformation.

demonstrated in the two simulations in fig. 4-1 compels confirmation and further investigation.

4.1.3 Optimized Elongated geometry with the Sophisticated transformation

To reduce the reactor volume (which reduces cost) and achieve higher Troyon-limited power (see eq. (1.8)) it is generally desirable to minimize R_0. However, the amount of necessary inboard space is dictated by technological limits, such as the required volumes of coil support structure, breeding blanket, and neutron shielding. Therefore R_{min}, the minimum distance of the flux surface from the axis of symmetry, should be considered the fixed parameter, not R_0. Also, the maximum allowable on-coil magnetic field is a material property of the magnet conductor and directly influences the magnet stresses. The choice of conductor material and amount of necessary magnet structure dramatically affects cost, which should stay fixed between designs. For this reason $B_\zeta\,(R_{min})$, the maximum on-coil magnetic field, should be fixed.

Therefore, in order to more closely approximate constant cost, a more realistic comparison fixes R_{min} and $B_\zeta\,(R_{min})$. In order to fix $B_\zeta\,(R_{min})$, the reference magnetic field B_r was adjusted for each rotated simulation such that $B_\zeta\,(R=3) = 1$.

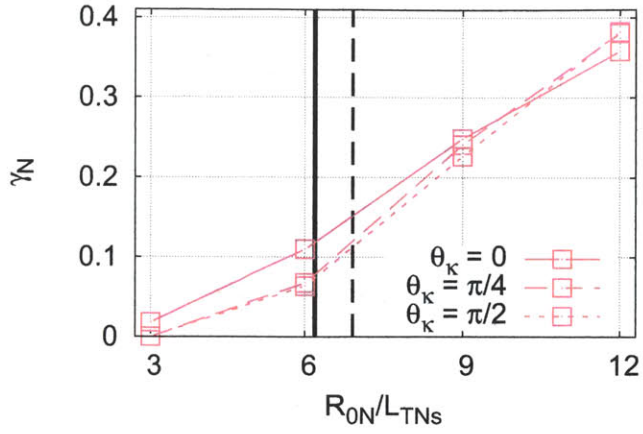

Figure 4-5: Largest turbulent mode linear growth rate for the elongated Cyclone base case parameters with the Simplistic transformation, where the vertical lines indicate an approximate midplane-averaged value for ITER [5] and Alcator C-Mod [72] (solid, black), plus the DIII-D Cyclone base case value (dotted, black).

Previously, the geometry of fig. 4-1 kept the global gradients constant, such that in a full reactor the peak temperature and density would be fixed. Instead we will attempt to keep the local turbulent drive constant by fixing the temperature gradient at the point we expect the mode to live, specifically R_{max}. Fixing R_{min}, $B_\zeta\left(R_{min}\right)$, and the gradients at R_{max} between different rotated geometries defines the Sophisticated transformation. Also, in these simulations (see fig. 4-6), we chose an outer flux surface in order to increase the effective aspect ratio and try to optimize for stronger momentum flux.

Fig. 4-7 calculates the time-averaged heat flux results for all of the above geometries. The time-average is given by $\langle \ldots \rangle_t \equiv \frac{1}{t_{corr}} \int_{t_0}^{t_0+t_{corr}} dt \left(\ldots\right)$, where t_{corr} is the turbulent correlation time. We see from the blue markers that fixing the local gradients at R_{max} to keep the turbulent drive constant was inappropriate because the heat flux now increases very strongly with tilt angle. In hindsight, this is unsurprising because the tokamak simulated in the $\theta_\kappa = \frac{\pi}{2}$ case would have twice the on-axis temperature of the unrotated case.

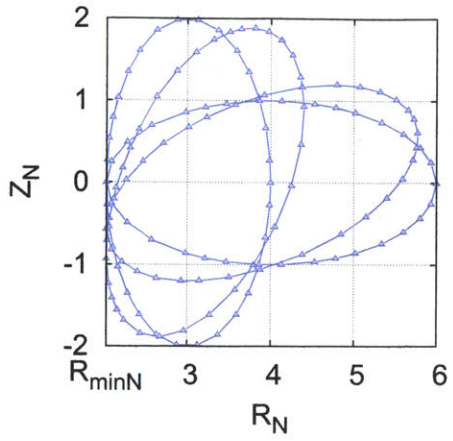

Figure 4-6: Optimized Elongated Cyclone base case at $\theta_\kappa = \{0, \frac{\pi}{8}, \frac{3\pi}{8}, \frac{\pi}{2}\}$ with the Sophisticated transformation.

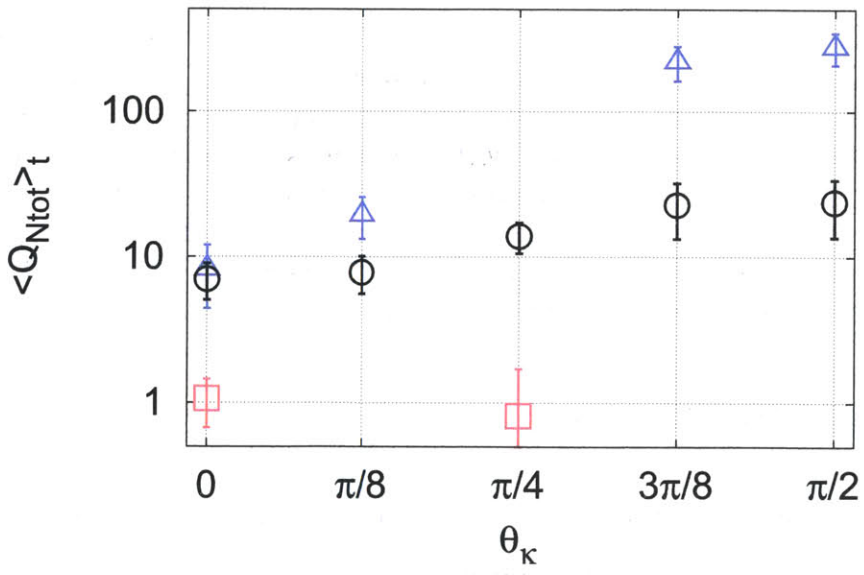

Figure 4-7: Time-averaged total nonlinear heat flux for the Elongated geometry with Simplistic transformation (red, squares), Elongated Extreme geometry with Simplistic transformation (black, circles), and Optimized Elongated geometry with Sophisticated transformation (blue, triangles).

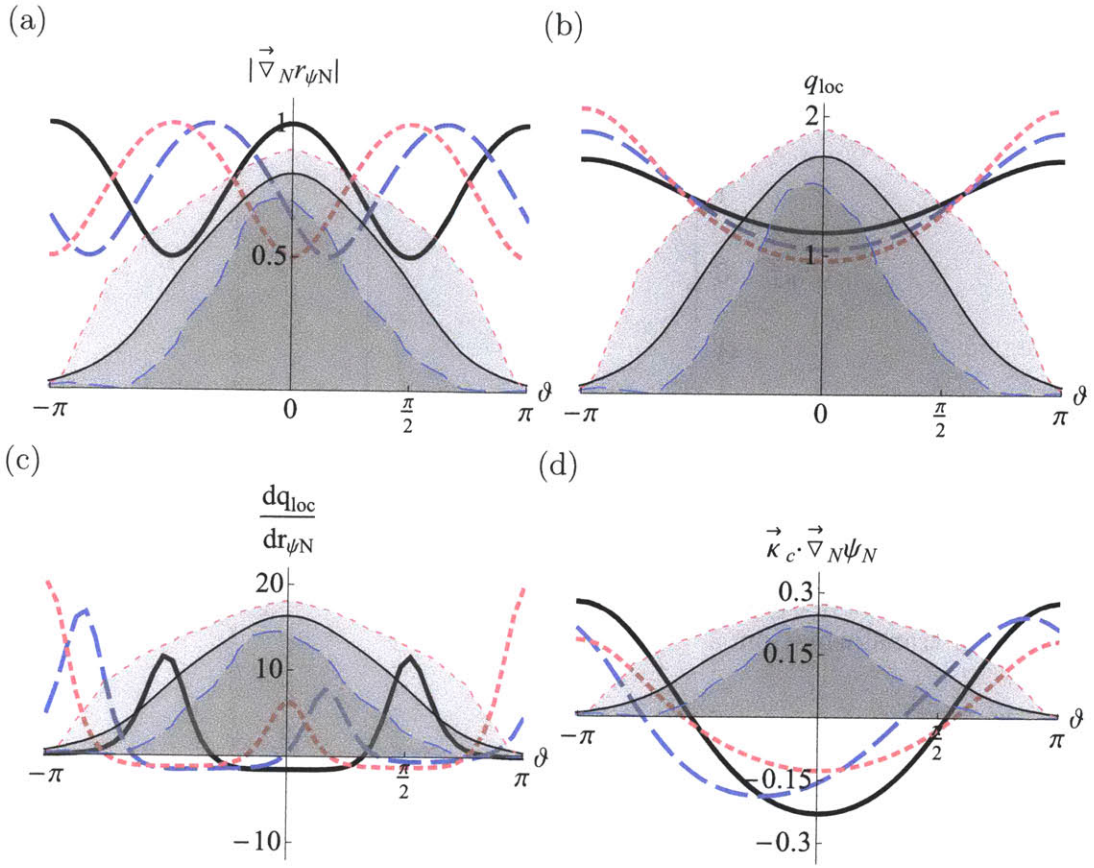

Figure 4-8: (a) the radial gradient in the flux surface label $r_{\psi N}$, (b) the local value of the safety factor, (c) the derivative of the local safety factor in the direction normal to the flux surface, and (d) the magnitude of the good magnetic field curvature for the elongated Cyclone base case geometry with the Simplistic transformation and $\theta_\kappa = 0$ (black, solid), $\theta_\kappa = \frac{\pi}{4}$ (blue, dashed), and $\theta_\kappa = \frac{\pi}{2}$ (red, dotted), where ϑ has been translated such that $\vartheta_{B_{max}} = \pm\pi$. The filled curves are identical between the four plots (except for a scaling factor) and show the shape and location of $|\phi_N|^2$ obtained from linear simulations performed for each of the three values of θ_κ.

4.2 Local quantities

Fig. 4-8 shows four local parameters, calculated using the Miller equilibrium model, that could be responsible for the trends in figs. 4-2, 4-5, and 4-7. For now we focus on the linear results in fig. 4-5. An explanation for the nonlinear results, shown in figs. 4-2 and 4-7, is left for future work. In all plots, because of the ϑ translation discussed in Section 3.2.3, we expect that the mode will live near $\vartheta = 0$. From fig. 4-8a we see that the flux surface spacing is dominated by the effects of flux surface shaping. A vertically elongated flux surface positions the mode exactly where the flux

surfaces are most compressed and, hence, the gradients are steepest. We see that, in the $\theta_\kappa = \pi/4$ case, the mode seems drawn to the region of steeper gradients. This suggests that that the local flux surface spacing may be partially responsible for the observed stabilizing effect.

Fig. 4-8b shows that the local safety factor, $q_{loc} \equiv \frac{I(\psi)}{R^2 \vec{B} \cdot \vec{\nabla} \vartheta}$, which we define analogously to the global safety factor, $q \equiv \frac{1}{2\pi} \oint\big|_\psi d\vartheta \left(\frac{I(\psi)}{R^2 \vec{B} \cdot \vec{\nabla} \vartheta} \right)$. It is dominated by the $1/R$ dependence of the toroidal magnetic field. Hence, since the vertical ellipse minimizes the range of a given flux surface in R, it has the least variation. On the other hand, the behavior of the local magnetic shear, shown in fig. 4-8c, is dominated by shaping effects. We see that the shear sharply peaks in the regions of high poloidal curvature and that elongation tilt locates this peak closer to the mode location.

Lastly fig. 4-8d shows that the magnetic curvature is good on the inboard side of the tokamak and bad on the outboard as expected. However, the rotated configurations have weaker bad curvature around $\vartheta = 0$, where we expect the mode to live. In the $\theta_\kappa = \pi/4$ case, we see the mode is drawn towards the region of bad curvature. In the $\theta_\kappa = \pi/2$ case, we see the mode spreads out further in response to the wider and shallower bad curvature well. The response of the mode to magnetic curvature suggests that it causes the observed turbulence suppression, however it still does not explain why elongation tilt is destabilizing at higher temperature gradients (see fig. 4-4).

4.3 Reactor prospects

From this analysis, it is not clear that the traditional upright, vertically elongated tokamak cross-section is necessarily optimal. However, it does makes sense why, before the advent of kinetic simulations, vertical elongation would be found to be the most promising.

As shown in Section 1.1.2, the circular cross-section is the shape that, at constant cross-sectional area, minimizes the safety factor. This is the worst case from the perspective of maximizing the efficiency of plasma confinement, according to

the Troyon limit (see eq. (1.5)). To determine the exact fusion power scalings for the constant-cost transformation (see table 4.2), we solve for P_f, ϑ_{min}, R_{0N}, B_{0N}, and a in $V_N = 2\pi R_{0N}\pi a^2\kappa$, $B_{\zeta N}(R_{minN}) = B_{0N}\frac{R_{0N}}{R_{minN}}$, $R_{minN} = R_N^{new}(a,\vartheta_{min})$, $\left.\frac{\partial R_N^{new}}{\partial\vartheta}\right|_{r_\psi=a,\vartheta=\vartheta_{min}} = 0$, and eq. (1.8), where $R_N^{new}(r_\psi,\theta)$ is given by eq. (3.16) and ϑ_{min} is the location of the minimum major radial position. Fig. 4-9 shows that vertical and horizontal elongation have very different effects on the safety factor and the maximum, Troyon-limited fusion power (assuming that the Troyon limit applies to horizontal and tilted elongation).

Taking the limit of $\kappa \to \infty$, we see that fusion power only scales with horizontal elongation as $\kappa^{2/3}$, whereas it scales with vertical elongation as κ^3. When vertical elongation is increased, both B_0 and R_0 stay fixed. However, when horizontal elongation is changed, in order to maintain constant on-coil magnetic field the device major radius must increase, which decreases the on-axis magnetic field. Both these effects cause the scaling of safety factor $q \sim \frac{r}{R_0}\frac{B_0}{B_p}$ with κ to weaken. At constant R_{min}, as $\kappa \to \infty$, we know that $R_0 \propto a\kappa$. For constant volume, $a \propto (R_0\kappa)^{-1/2}$ meaning that $R_0 \propto \kappa^{1/3}$. Since, at constant R_{min} and $B_\zeta(R_{min})$, $B_0 \propto R_0^{-1}$, eq. (1.8) implies that $P_f \propto \kappa^{2/3}$. This is a compelling argument for choosing vertically elongated tokamak flux surfaces over horizontal.

However, in Section 2.2.3, we showed that it is reasonable to think tilted flux surfaces can support higher elongations than vertically elongated surfaces. This can be estimated by numerically inverting the function $n_c(\kappa,\theta_\kappa)$, which appears in fig. 2-7. This gives $\kappa(n_c,\theta_\kappa)$, which can be substituted into the function displayed in fig. 4-9 to find $P_f(\kappa(n_c,\theta_\kappa),\theta_\kappa)$. The result, given in fig. 4-10, shows that, at the stability index of ITER, $n_c = -2.3$, a tilt of $\pi/8$ only decreases the Troyon-limited fusion power by 20%. However, this is admittedly a crude estimation as the analysis of fig. 4-9 was done with the Constant-cost transformation whereas fig. 2-7 used the Simplistic transformation. We also see that the ITER operating point ($\kappa = 1.75$, $\theta_\kappa = 0$) has a Troyon-limited fusion power of only 400 MW, instead of the nominal 500 MW. This apparent shortfall is because we are not using the proper major/minor radius or magnetic field for ITER.

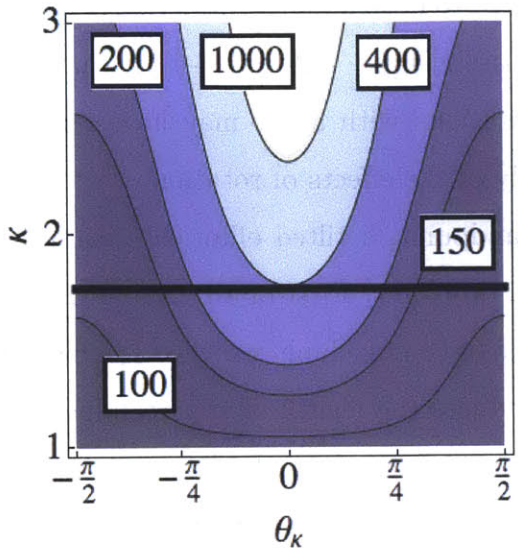

Figure 4-9: Contours of the total Troyon-limited fusion power (in MW) at fixed $R_{min} = 2$ m, $B_\zeta(R_{min}) = 9$ T, and $V = 12\pi^2$ m^3 assuming flat density and temperature profiles, with the elongation of ITER [5] (thick, black) indicated for reference.

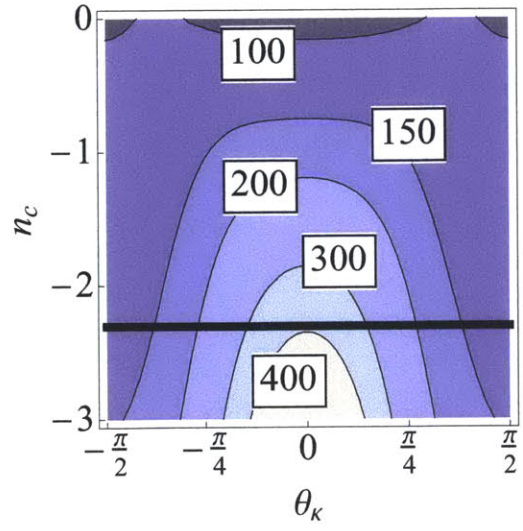

Figure 4-10: Contours of the total Troyon-limited fusion power (in MW) at for a tokamak with $R_0 \approx 3$ m, $a \approx 1$ m, $B_0 \approx 6$ T, assuming flat density and temperature profiles, with the stability index of ITER [5] (thick, black) indicated for reference.

Also, as we will see in Chapter 5, a tilt of $\frac{\pi}{8}$ seems optimal for maximizing core rotation, which is expected to both allow for violation of the Troyon limit and suppress turbulent transport. Lastly, figs. 4-2 and 4-5 give nonlinear and linear evidence suggesting that configurations with a tilt may have less inherent turbulent energy transport, independently of the effects of rotation.

From a practical standpoint, a tilted elliptical tokamak eases many of the most limiting tokamak design problems. First of all, having tilted TF coils allows for more space in the inboard side of the machine, which is the most space-constrained region of any design. It also reduces the length of superconducting tape that must operate at the maximum on-coil magnetic field. In fact, at constant peak on-coil magnetic field, the average on-coil magnetic field is lower because the average R position of the coil decreases, likely easing stress limits. However, the stress limits may prove more challenging because the forces on the magnets are now asymmetric. Furthermore, we now have the added option of placing the divertor near the outboard tip of the ellipse. This increases its major radial position and, hence, the surface area which reduces power handling requirements. However, this may be undesirable, because placing the x-point on the outboard side can lead to stronger ballooning modes [73].

Chapter 5

Momentum transport

GS2 only simulates a field line on a single flux surface and outputs turbulent fluxes. Without a transport solver, such as TRINITY [70], and many GS2 runs it is impossible to construct a rotation profile. However, we can use the GS2 turbulent fluxes to estimate the velocity gradients that would be possible in our geometries. We find that, with steeper temperature gradients, an initially stationary plasma can reorganize more momentum and achieve faster rotation. Also, these velocity gradients, estimated from GS2 output, can be compared with an experimental study that looked at the connection between up-down asymmetry and intrinsic rotation.

5.1 Velocity gradient estimation from GS2 output

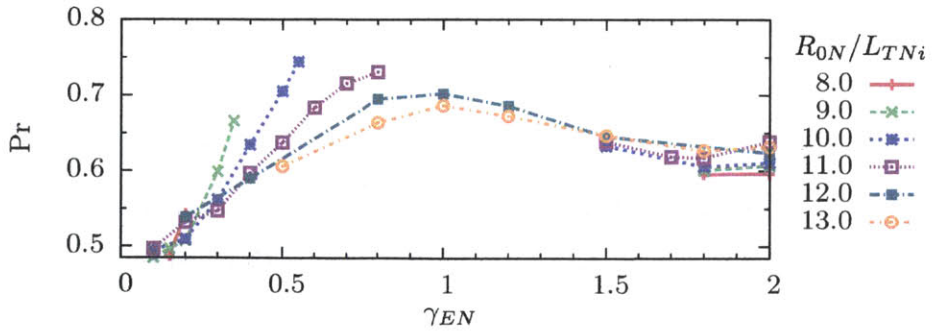

Figure 5-1: The insensitivity of the Prandtl number to the background flow shear and ion temperature gradient (figure from ref. [20]).

To estimate the velocity gradient we assume that Fick's first law of diffusion applies to the radial transport of rotation and temperature, to write

$$\langle \Pi_{\zeta s} \rangle_t \approx -D_{\Pi s} R_0^2 n_s m_s \left\langle \frac{\partial \Omega_{\zeta s}}{\partial r_\psi} \right\rangle_t + \langle \Pi_{\zeta s}^{ud} \rangle_t = 0 \tag{5.1}$$

and

$$\langle Q_s \rangle_t \approx -D_{Qs} n_s \left\langle \frac{\partial T_s}{\partial r_\psi} \right\rangle_t . \tag{5.2}$$

Here $\Pi_{\zeta s}^{ud}$ is the momentum flux due to the symmetry breaking of up-down asymmetry. This quantity is what we have calculated with GS2 by setting $\Omega_\zeta = 0$ and choosing up-down asymmetric configurations. In order to set the total momentum flux to zero, we have assumed that, after averaging over the turbulent timescale, the profile is in steady-state and there is no external momentum input. Crucially, we note from fig. 5-1 that the turbulent Prandtl number $Pr_s \equiv \frac{D_{\Pi s}}{D_{Qs}} \approx 0.55$ is approximately constant across tokamak parameters [20]. This can be used to relate eqs. (5.1) and (5.2) giving the nondimensionalized form

$$\frac{R_{0N}^2 n_{Ns} m_{Ns} \left\langle \frac{\partial \Omega_{\zeta Ns}}{\partial r_{\psi N}} \right\rangle_t}{n_{Ns} \left\langle \frac{\partial T_{Ns}}{\partial r_{\psi N}} \right\rangle_t} \approx \frac{1}{Pr_s} \frac{\langle \Pi_{\zeta Ns}^{ud} \rangle_t}{\langle Q_{Ns} \rangle_t}, \tag{5.3}$$

which can be approximated as

$$\frac{\left\langle \frac{\partial u_{\zeta Ns}}{\partial r_{\psi N}} \right\rangle_t}{\left\langle \frac{\partial T_{Ns}}{\partial r_{\psi N}} \right\rangle_t} \approx \left(\frac{1}{m_{Ns} R_{0N} Pr_s} \right) \frac{\langle \Pi_{\zeta Ns}^{ud} \rangle_t}{\langle Q_{Ns} \rangle_t}. \tag{5.4}$$

Since, to lowest order in $\sqrt{\frac{m_e}{m_i}}$, the electrons carry no momentum, the ion term, $\langle \Pi_{\zeta Ns}^{ud} \rangle_t / \langle Q_{Ns} \rangle_t$, is the relevant parameter for our analysis. This means that for all simulations performed in this work (see table 4.1), the estimated ratio of velocity and

temperature gradients is given by

$$\frac{\left\langle \frac{\partial u_{\zeta Ns}}{\partial r_{\psi N}} \right\rangle_t}{\left\langle \frac{\partial T_{Ns}}{\partial r_{\psi N}} \right\rangle_t} \approx 0.61 \frac{\left\langle \Pi^{ud}_{\zeta Ns} \right\rangle_t}{\langle Q_{Ns} \rangle_t}. \tag{5.5}$$

5.2 Elliptical geometry

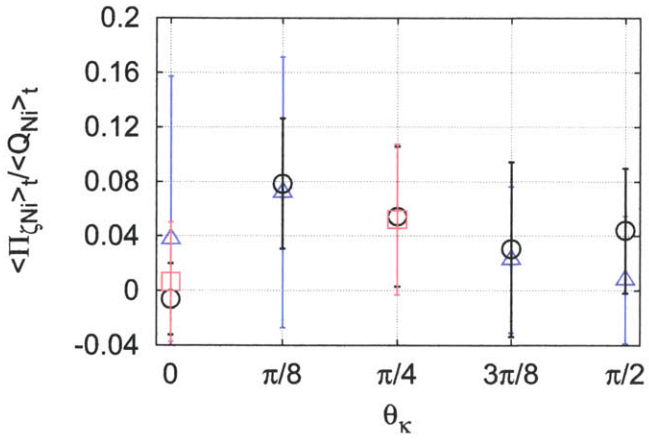

Figure 5-2: Time-averaged ratio of ion angular momentum and heat fluxes for the geometries and transformations of figs. 4-1 (red, squares), 4-3 (black, circles), and 4-6 (blue, triangles).

Fig. 5-2 shows the nonlinear momentum flux results for the three geometries and transformations detailed in Chapter 5. Quantitatively, we see very similar behavior despite the differences in input parameters. This suggests that $\left\langle \Pi^{ud}_{\zeta Ni} \right\rangle_t / \langle Q_{Ni} \rangle_t$ is relatively insensitive to the background gradients and aspect ratio. We know that the momentum flux must eventually go to zero as $\epsilon \to 0$ because the geometry loses any reference by which to define up-down asymmetry, but the simulations do not seem to be close to this limit.

We see that the up-down symmetric cases at $\theta_\kappa \in \left\{0, \frac{\pi}{2}\right\}$ have a vanishing momentum to heat flux ratio, while the peak of the curve is around 0.08 and occurs at $\theta_\kappa = \frac{\pi}{8}$. This implies that the normalized velocity gradient would be about 5% the normalized temperature gradient (see eq. (5.5)). It may seem intuitive that the peak should occur at $\frac{\pi}{4}$, halfway between the two up-down symmetric cases. However, since

vertical and horizontal elongation have very different effects on plasma turbulence, there is no reason to expect the curve to be symmetric about $\frac{\pi}{4}$.

5.3 Triangular geometry

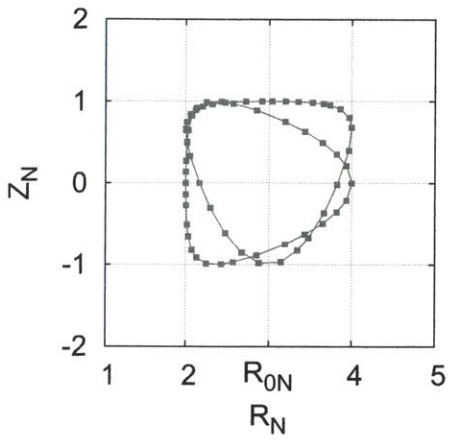

Figure 5-3: Triangular Extreme Cyclone base case (see table 4.1) at $\theta_\kappa = \left\{0, \frac{\pi}{2}\right\}$ with the Simplistic transformation.

Since the elliptical geometry showed such consistent momentum flux results across a range of input parameters, a triangular geometry was also simulated (see fig. 5-3). As shown in Chapter 2, triangularity has trouble penetrating to the magnetic axis in order to achieve up-down asymmetric flux surfaces throughout the plasma. As such, these simulations were not about advocating triangularity as a practical means to achieve high levels of intrinsic rotation. Rather, they were about showing that the magnitude momentum fluxes observed are characteristic of up-down asymmetry in general and are not a consequence of some peculiarity of elongated flux surfaces.

We see in fig. 5-4 that the triangular flux surfaces caused even less momentum transport than the elongated surfaces. It is important to note that the $\theta_\delta = 0$ simulation is up-down symmetric, while the $\theta_\delta = \frac{\pi}{2}$ simulation is asymmetric yet still has near zero momentum transport. A conceptual understanding of this is left for future work.

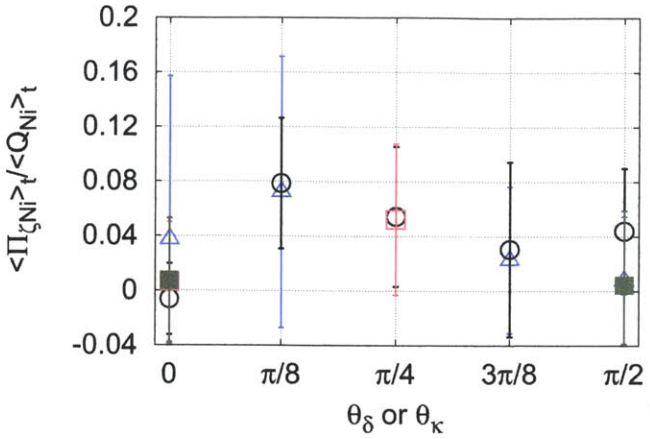

Figure 5-4: Time-averaged ratio of ion angular momentum and heat fluxes for the geometry of fig. 5-3 (green, filled squares) with the elongated results (empty shapes) shown for comparison.

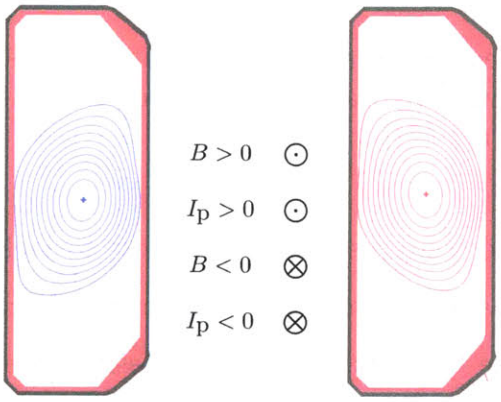

Figure 5-5: The a^+ (left, blue) and a^- (right, red) magnetic flux surfaces from the TCV experiment (figure from ref. [74]).

5.4 TCV up-down asymmetry experiment [74, 75]

The Tokamak à Configuration Variable (TCV) [76, 77] is a Swiss experiment devoted to studying strongly shaped plasmas. It has a particularly large vacuum vessel and powerful PF coils that make it ideal for studying up-down asymmetric configurations.

5.4.1 Experimental overview

In 2010, Camenen *et al.* published the results of a TCV experimental study of the effects of up-down asymmetry on intrinsic rotation. In order to isolate the effect of

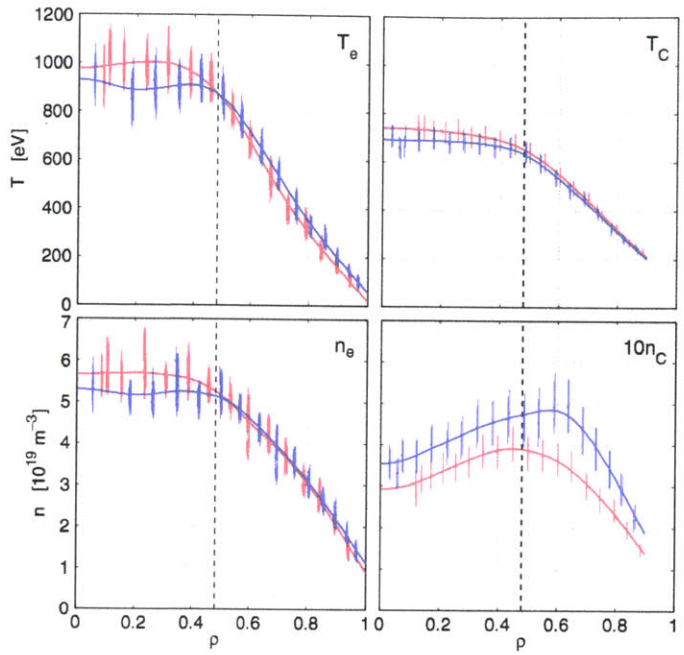

Figure 5-6: The measured temperature and density profiles from the a^+ (blue) and a^- (red) configurations with the sawtooth inversion radius indicated by the vertical dashed line (figure from ref. [74]).

up-down asymmetry, the study used multiple shots to look for a differential effect on the rotation profile between two asymmetric magnetic configurations (see fig. 5-5). The shots were made to be as identical as possible (see fig. 5-6) except for key changes in the sign of three quantities: the equilibrium flux surface asymmetry, the toroidal magnetic field, and the plasma current. In each shot, the toroidal rotation of the carbon impurity species was measured from Doppler shift of charge exchange radiation. The rotation of the main ion species, deuterium, is then calculated from the carbon rotation using a neoclassical physics code.

We choose to identify the two magnetic configurations by a^+ and a^-, indicating the sign of the asymmetry with the sign of the elongation tilt angle of the flux surfaces (see fig. 5-5). The direction of the toroidal magnetic field is signified by b^+ and b^-, where positive is defined to be in the $\hat{e}_\zeta$ direction, clockwise when viewed from above the machine. The direction of the plasma current is similarly defined and signified by j^+ or j^-. Theoretically, one of these parameters could have been removed by using it to define the signs of the other two. However, it was desirable to vary all three to

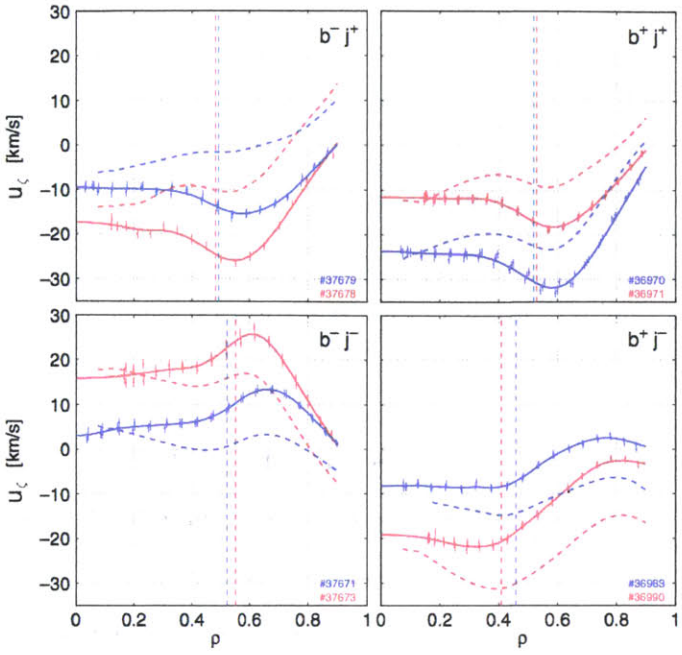

Figure 5-7: The measured rotation profiles for deuterium (solid) and the carbon impurity (dashed) from the a^+ (blue) and a^- (red) configurations with the sawtooth inversion radius indicated in each case by the vertical dashed lines (figure from ref. [74]).

check for any unexpected symmetry breaking from the practicalities of the machine. Lastly, we define the sign of any quantity Q to be $s_Q \equiv \text{sign}\,(Q)$.

According to theory, the sign of the intrinsic momentum flux is given by $s_{\Pi_{int}} = s_a s_b s_j$, where positive indicates an outwards flux of momentum in the $\hat{e}_\zeta$ direction. A positive momentum flux will expel momentum from the core of the plasma, creating a more hollow rotation profile and a more positive rotation gradient. This is definitively confirmed by the experimental results outside the sawtooth inversion radius, where the asymmetry is the strongest. We can see in the upper-right and lower-left plots of fig. 5-7 (where $s_b s_j > 0$) that the a^+ has a more hollow rotation profile and more positive rotation gradients. The other two plots (where $s_b s_j < 0$) see the opposite trend as expected.

Camenen *et al.* define a parameter $\Delta u_\zeta \equiv u_\zeta|_{\rho=0.65} - u_\zeta|_{\rho=0.85}$ which indicates the average toroidal velocity gradient over a 5.55 cm radial region near the plasma edge. However, even within a given $a^\pm b^\pm j^\pm$ configuration, both co-current and counter-

b^+	j^+		j^-		b^-	j^+		j^-	
a^+	**−18.0**	−19.4	—		a^+	**−6.9**	−11	**5.8**	8.4
	—		**−1.9***	−0.1		**−1.1***	−3.4	—	
a^-	**−10.1**	−12.4	—		a^-	**−15.8**	−18.6	**18.7**	18.4
	−1.1*	−1.3	**−5.9***	−4.9		—		—	

Table 5.1: Δu_ζ in km/s where bold font indicates deuterium, regular font indicates carbon, an asterisk denotes co-current central rotation cases, and the gray background denotes that $s_a s_b s_j > 0$ (table adapted from ref. [74]).

current rotation profiles were experimentally observed. Those shots with co-current rotation had non-monotonic rotation profiles near the edge that obscured the effects of up-down asymmetry and led to smaller average gradients. As a result, co-current and counter-current cases are listed separately in table 5.1 and should be compared separately. Nevertheless, in all cases we still expect that $s_a s_b s_j > 0$ will lead to a more negative Δu_ζ. We see that there are a total of 11 valid comparisons and 9 match up as expected. No satisfying explanation for the two disagreeing comparisons has been determined, other than suggesting that the $a^+b^-j^-$ case is perhaps errant.

5.4.2 Comparison to GS2 results

Ref. [74] provides exactly enough information to allow comparison with our results for $\langle \Pi^{ud}_{\zeta Ni} \rangle_t / \langle Q_{Ni} \rangle_t$ from Section 5.2. Here, in order to compare with experiment, we will interpret the reference macroscopic length, l_r, as the tokamak minor radius, a, implying that $r_{\psi N} = \rho$. We can then invert eq. (5.4) to get

$$\frac{\langle \Pi^{ud}_{\zeta Ni} \rangle_t}{\langle Q_{Ni} \rangle_t} \approx m_{Ni} R_{0N} Pr_i \frac{\left\langle \frac{\partial u_{\zeta Ni}}{\partial \rho} \right\rangle_t}{\left\langle \frac{\partial T_{Ni}}{\partial \rho} \right\rangle_t}. \tag{5.6}$$

Using the normalizations of table 3.2 we find that

$$\frac{\langle \Pi^{ud}_{\zeta Ni} \rangle_t}{\langle Q_{Ni} \rangle_t} \approx m_i R_0 Pr_i \frac{v_{thr}}{2a} \frac{\left\langle \frac{\partial u_{\zeta i}}{\partial r_\psi} \right\rangle_t}{\left\langle \frac{\partial T_i}{\partial r_\psi} \right\rangle_t}. \tag{5.7}$$

However, the TCV experiment measured a differential effect between two mirror opposite up-down asymmetric equilibrium. From inspection of fig. 5-5 we see that, primarily, the flux surfaces were elongated with $\theta_\kappa = \frac{\pi}{8}$ for the a^+ configuration and $\theta_\kappa = -\frac{\pi}{8}$ for a^-. That means we will recast eq. (5.7) as

$$\left.\frac{\langle \Pi^{ud}_{\zeta Ni}\rangle_t}{\langle Q_{Ni}\rangle_t}\right|_{\theta_\kappa=\frac{\pi}{8}} - \left.\frac{\langle \Pi^{ud}_{\zeta Ni}\rangle_t}{\langle Q_{Ni}\rangle_t}\right|_{\theta_\kappa=-\frac{\pi}{8}} \approx m_i R_0 Pr_i \frac{v_{thr}}{2a}\left(\left.\frac{\left\langle \frac{\partial u_{\zeta i}}{\partial r_\psi}\right\rangle_t}{\left\langle \frac{\partial T_i}{\partial r_\psi}\right\rangle_t}\right|_{a^+} - \left.\frac{\left\langle \frac{\partial u_{\zeta i}}{\partial r_\psi}\right\rangle_t}{\left\langle \frac{\partial T_i}{\partial r_\psi}\right\rangle_t}\right|_{a^-}\right). \tag{5.8}$$

Also, the averages over the turbulence time scale are already inherent in the experimental techniques used to measure the flow and temperature gradients, so they may be dropped. We also observe from fig. 5-6 that the temperature profiles for a^+ and a^- are more or less identical. Since the paper provides the difference in velocity Δu_ζ, we must discretize the derivatives about $\rho = 0.75$ to get

$$\left.\frac{\langle \Pi^{ud}_{\zeta Ni}\rangle_t}{\langle Q_{Ni}\rangle_t}\right|_{\theta_\kappa=\frac{\pi}{8}} - \left.\frac{\langle \Pi^{ud}_{\zeta Ni}\rangle_t}{\langle Q_{Ni}\rangle_t}\right|_{\theta_\kappa=-\frac{\pi}{8}} \approx m_i R_0 Pr_i \frac{v_{thr}}{2a}\left(\frac{\Delta u_\zeta|_{a^+} - \Delta u_\zeta|_{a^-}}{\Delta T_i}\right) \tag{5.9}$$

where $\Delta T_i \equiv T_i|_{\rho=0.65} - T_i|_{\rho=0.85}$ is defined analogously to Δu_ζ. Using the upper left plot of fig. 5-6 we can estimate both $T_i|_{\rho=0.75} = 400$ eV and $\Delta T_i = 400$ eV. Also, we approximate the difference in Δu_ζ between a^+ and a^- by averaging over the three sets of counter-current measurements listed in table 5.1 to get $\Delta u_\zeta|_{a^+} - \Delta u_\zeta|_{a^-} = 8$ km/s. Now we use that $m_i = m_D = 2$ amu, $R_0 = 0.88$ m, $l_r = a = 0.25$ m, and that $Pr_i = 0.55$ is roughly constant to find the experimental value to be

$$\left(\left.\frac{\langle \Pi^{ud}_{\zeta Ni}\rangle_t}{\langle Q_{Ni}\rangle_t}\right|_{\theta_\kappa=\frac{\pi}{8}} - \left.\frac{\langle \Pi^{ud}_{\zeta Ni}\rangle_t}{\langle Q_{Ni}\rangle_t}\right|_{\theta_\kappa=-\frac{\pi}{8}}\right)_{exp} \approx 0.08. \tag{5.10}$$

By using fig. 5-2, GS2 simulations give

$$\left(\left.\frac{\langle \Pi^{ud}_{\zeta Ni}\rangle_t}{\langle Q_{Ni}\rangle_t}\right|_{\theta_\kappa=\frac{\pi}{8}} - \left.\frac{\langle \Pi^{ud}_{\zeta Ni}\rangle_t}{\langle Q_{Ni}\rangle_t}\right|_{\theta_\kappa=-\frac{\pi}{8}}\right)_{sim} \approx 0.16 \tag{5.11}$$

which only differs from the experimental value by a factor of two. In fact, it would be unreasonable to expect more than an order of magnitude agreement considering we took the large aspect ratio limit and averaged over the entire outer region of the plasma. Furthermore, the elongated Cyclone base case geometry used for the simulations is considerably different than the geometry of TCV. Still, this comparison shows that neither the simulations nor the experimental results appear unreasonable.

In TCV, the introduction of up-down asymmetry was able to increase the up-down symmetric rotation profiles by roughly 50%. The rotation present in the up-down symmetric case was due to effects that are formally small in ρ_* (see Section 1.2). However, in larger machines, ρ_* is smaller and external momentum injection is less feasible. This means that the effect of up-down asymmetry will be much more significant in these larger devices. It may not be possible to access new regimes of rotation using intrinsic rotation, but it does seem that the level of rotation seen in current machines can be generated in future, reactor-sized devices by using up-down asymmetry.

Chapter 6

Conclusions

This thesis analyzed the equilibrium, stability, and transport characteristics of tokamaks with up-down asymmetric poloidal cross-sections.

The results of MHD equilibrium analysis (Section 2.1) demonstrated that external PF coils only have direct control over the outermost flux surface. Inside the plasma the toroidal current distribution has a significant effect on modifying the flux surface shape. It was shown that hollow current profiles are optimal for supporting up-down asymmetry to the magnetic axis. Furthermore, ellipticity, the lowest harmonic shaping effect, penetrated to the magnetic axis most effectively. The effect of the Shafranov shift was studied and found not to significantly affect asymmetry penetration. We then looked at the stability of tilted elliptical flux surfaces to axisymmetric modes and found that is was better than traditional vertically elongated flux surfaces (see fig. 2-7).

Chapter 3 detailed the modification and testing of GS2 to support the modeling of up-down asymmetric tokamak configurations.

This newly modified code was applied to model the turbulent energy transport in tilted elliptical tokamaks. Figs. 4-2 and 4-5 show linear and nonlinear evidence that elliptical flux surfaces with a tilt may experience significantly reduced turbulent energy transport, particularly below some currently unknown values of the background gradients.

Furthermore, the results of nonlinear momentum flux simulations, shown in fig.

Advantages
- Possible inherent reduction in turbulent energy transport (figs. 4-2 and 4-5) - Increased toroidal rotation (fig. 5-2), likely dominating in a reactor + Allows violation of the Troyon limit (Section 1.1.3) + Suppresses turbulent energy transport (Section 1.1.3) - Possibility of increasing divertor surface area, due to increased major radial position (Section 4.3) - More inboard space and shorter magnet length at peak on-coil field (fig. 4-6)
Disadvantages
- Estimated 20% decrease in the Troyon-limited fusion power at constant stability to axisymmetric modes (fig. 4-10) - Asymmetric toroidal field magnet stresses (Section 4.3)

Table 6.1: Summary of the tradeoffs of a elongated tokamak with a tilt of $\pi/8$ relative to a traditional vertically elongated tokamak.

5-2 agree with TCV experimental results. They both predict $\frac{1}{v_{thi}}\frac{du_{\zeta i}}{d\rho}$ to be approximately 5% of $\frac{1}{T_i}\frac{dT_i}{d\rho}$ for elliptical flux surfaces with a $\pi/8$ tilt. The introduction of this tilt in TCV was enough to change to core rotation by over 50% [74]. However, in larger tokamaks ρ_* is smaller, so all sources of intrinsic rotation except up-down asymmetry are reduced. This means, in a reactor with a $\pi/8$ tilt, we would still expect $\frac{1}{v_{thi}}\frac{du_{\zeta i}}{d\rho}$ to be approximately 5% of $\frac{1}{T_i}\frac{dT_i}{d\rho}$, but the effects of up-down asymmetry would dominate the rotation profile.

These results are summarized in table 6.1 and merit further investigation into the viability of a tilted elliptical tokamak as a reactor. This includes determining the operating space that sees a turbulent energy transport reduction from elongation tilt and the stability properties to nonaxisymmetric MHD.

Appendix A

Symbol Glossary

Miscellaneous

$_{0,1,2,...}$		Number subscript, indicates the order of the quantity in the expansion parameter order the poloidal mode number.
$_{\|\|}$		Parallel subscript, indicating the vector component in the direction of $\vec{B}$.
$_{\perp}$		Perpendicular subscript, indicating the vector components perpendicular to $\vec{B}$.
$\langle \ldots \rangle_{\varphi}$		Average over gyromotion, $\langle \ldots \rangle_{\varphi} \equiv \frac{1}{2\pi} \int_0^{2\pi} \Big\vert_{\vec{R}_{gc}, w_{\|\|}, \mu, t} d\varphi \, (\ldots)$.
$\langle \ldots \rangle_{\psi}$		Flux surface average, $\langle \ldots \rangle_{\psi} \equiv \left(\frac{dV}{d\psi} \right)^{-1} \int_0^{2\pi} d\theta \int_0^{2\pi} d\zeta \frac{(\ldots)}{\vert \vec{B} \cdot \vec{\nabla} \theta \vert}$.
$\langle \ldots \rangle_{t}$		Time average over the turbulent time scale, $\langle \ldots \rangle_{t} \equiv \frac{1}{t_{corr}} \int_{t_0}^{t_0 + t_{corr}} dt \, (\ldots)$.
$\langle \ldots \rangle_{V}$		Volume average, $\langle \ldots \rangle_{V} \equiv \int dV \, (\ldots) \, / \int dV$.
$\{\ldots, \ldots\}$	eq. (1.27)	Poisson bracket.
$\tilde{}$		Tilde, indicates a quantity defined outside the plasma region.

Greek letters

α	eq. (1.17)	Tokamak coordinate in the direction perpendicular to the magnetic field within the flux surface.

$\alpha^\dagger$		Dummy integration variable.
α		α subscript, indicating the vector component in the direction of α.
β_p		Poloidal beta, ratio of plasma to poloidal magnetic field pressure, $\beta_p \equiv \frac{2\mu_0 \langle p \rangle_V}{B_{pa}^2}$.
β_N	eq. (1.5)	Normalized plasma beta.
β_T	eq. (1.1)	Toroidal beta, ratio of plasma to magnetic field pressure.
γ		Mode growth rate, $\gamma \equiv \text{Imag}[\omega]$.
γ_c		Ratio of specific heats, also called the adiabatic index.
γ_E		Tokamak flow shear, $\gamma_E \equiv \frac{\rho}{q}\frac{d\Omega_\zeta}{d\rho}$.
$\vec{\Gamma}_B$		Magnetic field flux.
Γ_s	eq. (1.31)	Species flux surface averaged total particle flux.
δ	table 3.1, eq. (3.3)	Flux surface triangularity.
δ_M		Miller equilibrium flux surface triangularity, $\delta_M \equiv \sin(\delta)$.
Δu_ζ		Average toroidal velocity gradient in the outer part of the tokamak plasma, $\Delta u_\zeta \equiv u_\zeta\|_{\rho=0.65} - u_\zeta\|_{\rho=0.85}$.
ΔT_s		Species average temperature gradient in the outer part of the tokamak plasma, $\Delta T_s \equiv T_s\|_{\rho=0.65} - T_s\|_{\rho=0.85}$.
ϵ		Tokamak inverse aspect ratio, $\epsilon \equiv a/R_0$.
ζ	fig. 1-1	Tokamak toroidal angle.
ζ		ζ subscript, indicating the vector component in the direction of ζ.
θ	fig. 1-1	Poloidal angle, $\theta \equiv \arctan\left(\frac{Z}{R-R_0}\right)$.
θ_δ	fig. 3-2b	Tokamak triangularity tilt angle.
θ_κ	fig. 3-2a	Tokamak elongation tilt angle.
$\vartheta_{B_{max}}$		The poloidal location of the maximum magnetic field in GS2.
ϑ	eq. (3.16)	Poloidal coordinate.
ϑ_{min}		The value of ϑ which minimizes R on a given flux surface.
ϑ_{shift}		Constant used to translate the GS2 definition of ϑ such that $\vartheta_{B_{max}} = \pm\pi$, $\vartheta_{shift} \equiv \pm\pi - \vartheta_{B_{max}}$.

κ		Tokamak flux surface elongation, $\kappa \equiv b/a$.
$\vec{\kappa}_c$		Magnetic field curvature, $\vec{\kappa}_c \equiv \hat{b} \cdot \vec{\nabla}\hat{b}$.
λ_N		Velocity space coordinate, $\lambda_N \equiv \mu/\mathscr{E}$.
$\lambda_\pm$	eq. (2.101)	Eigenvalues of a two dimensional matrix.
μ		Magnetic moment, $\mu \equiv \frac{m_s w_\perp^2}{2B}$.
μ_w		Permeability of the vacuum vessel wall.
μ_0		Permeability of free space.
π		Ratio of a circle's circumference to its diameter, $\pi = 3.14159\ldots$.
$\Pi_{\zeta s}^{ud}$		Species up-down asymmetric contribution to the flux surface averaged total flux of toroidal angular momentum.
$\Pi_{\zeta s}$	eq. (1.32)	Species flux surface averaged total momentum flux.
ρ	fig. 1-1	Tokamak normalized flux surface label, $\rho \equiv \sqrt{\psi/\psi_b}$.
$\vec{\rho}_s$		Particle gyroradius, $\vec{\rho}_s \equiv \frac{\vec{v}_\perp}{\vec{\Omega}_s}$.
ρ_*		Rho-star, $\rho_* \equiv \rho_i/a$.
σ_{err}		The standard deviation of the fractional error at each ϑ grid point of ϕ_N in the stationary mode test case.
σ_w		Conductivity of the vacuum vessel wall.
$\langle \sigma v \rangle_{DT}$		DT fusion reaction rate constant.
τ_E	eq. (1.2)	Energy confinement time.
τ_w	eq. (1.9)	Magnetic field energy confinement time by a vacuum vessel wall.
ϕ		Turbulent electrostatic potential.
$\tilde{\phi}$		Error magnetic field that arises from corrections that are necessary to the pure wire field.
Φ		Background electrostatic potential.
φ	eq. (1.18)	Particle gyroangle.
χ		Tokamak toroidal flux, $\chi \equiv \frac{1}{2\pi}\int_0^{2\pi} d\theta \int_0^a dr_\psi \left(r_\psi B_\zeta(R)\right)$.
ψ		Tokamak poloidal magnetic field flux coordinate, $\psi \equiv \frac{1}{2\pi}\int d\vec{S} \cdot \vec{B}_p$.
ψ_{ext}		Poloidal flux from all external coils acting on the plasma.

ψ_w		Poloidal flux from a wire carrying current $I_p\hat{e}_\zeta$ placed at $(R_{0b}, 0)$.
ψ_{val}		A given, specific value of the tokamak poloidal magnetic field flux coordinate.
ψ		ψ subscript, indicating the vector component in the direction of ψ.
ω		Mode angular frequency.
Ω_s		Particle angular gyrofrequency, $\Omega_s \equiv \frac{Z_s e B}{m_s c}$.
Ω_ζ		Tokamak angular rotation frequency, $\Omega_\zeta \equiv u_\zeta / R$.
$\Omega_{\zeta s}$		Species tokamak angular rotation frequency, $\Omega_{\zeta s} \equiv u_{\zeta s}/R$.

Roman letters

a	fig. 1-1	Tokamak minor radius.
$a^\pm$	fig. 5-5	The direction of the TCV up-down asymmetry, given by the sign of θ_κ.
a_{sym}		Outdated GS2 parameter used to create divertor-like geometries.
a_w		Vacuum vessel wall minor radius.
$axis$		$axis$ subscript, indicating the location of the magnetic axis.
A		Positive constant form for constant current profile, $A \equiv \mu_0 j_\zeta R_0$.
A_p		Positive constant for pressure contribution to constant current profile, $A_p \equiv -\mu_0 R_0^2 \frac{dp}{d\psi}$.
A_m		Positive constant for magnetic contribution to constant current profile, $A_m \equiv -\frac{1}{2}\frac{d}{d\psi}(I^2)$.
A_h		Positive constant for on-axis $\mu_0 j_\zeta R_0$ in the linear, hollow current profile.
A_c		Positive constant for on-axis $\mu_0 j_\zeta R_0$ in the linear, peaked current profile.
A'_h		Positive constant for slope of $\mu_0 j_\zeta R_0$ in the linear, hollow current profile.
A'_c		Positive constant for slope of $\mu_0 j_\zeta R_0$ in the linear, peaked current profile.

$\vec{a}_s$	eq. (1.26)	Particle acceleration.
b	fig. 1-1	Tokamak ellipse major radius.
$\hat{b}$		Magnetic field unit vector, $\hat{b} \equiv \frac{\vec{B}}{B}$.
$_b$		Boundary subscript, indicating the value is evaluated at the outermost flux surface with plasma.
$b^{\pm}$		The direction of the TCV toroidal magnetic field, positive is defined to be clockwise viewed from above the machine.
$\vec{B}$		Magnetic field.
$\vec{B}_{ext}$	eq. (2.37), eq. (2.96)	Magnetic field from external coils acting on the plasma.
$\vec{B}_p$		Tokamak poloidal magnetic field, $\vec{B}_p \equiv \vec{\nabla}\zeta \times \vec{\nabla}\psi$.
B_{pa}		Edge value of the tokamak poloidal magnetic field, $B_{pa} \equiv B_p(a)$.
$\vec{B}_{shape}$		External magnetic field used to create the desired flux surface shape.
$\vec{B}_{tot}$		The total magnetic field.
$\vec{B}_w$	eq. (2.38)	The magnetic field from a wire carrying current $I_p\hat{e}_\zeta$ placed at $(R_{0b}, 0)$.
$\vec{B}_v$		Tokamak required vertical field for major radial equilibrium, $\vec{B}_v \equiv \frac{1}{I_p^2}\vec{I}_p \times \vec{F}_p$.
$\vec{B}_{v0}$	eq. (2.91)	Tokamak required vertical field for major radial equilibrium at the equilibrium position.
B_0		Tokamak on-axis magnetic field, $B_0 \equiv B_\zeta(R_0)$.
c		Speed of light.
$c_{\sigma v}$		$\langle\sigma v\rangle_{DT}$ reaction rate constant of proportionality, $\langle\sigma v\rangle_{DT} \approx c_{\sigma v}T_i^2$ and $c_{\sigma v} = 1.1 \times 10^{-24}$ m^3/(keV^2-s).
$_c$		Subscript c, indicating the carbon impurity species.
$_C$		Subscript C, indicating the cosine coefficient in a Fourier series.
C_{cm}		Lowest order Fourier cosine coefficient, where $m \geq 0$ is an integer.
C_{hm}		Lowest order Fourier cosine coefficient, where $m \geq 0$ is an integer.

C_m		Lowest order Fourier cosine coefficient, where $m \geq 0$ is an integer.
C'_m		Next order Fourier cosine coefficient, where $m \geq 0$ is an integer.
C'_{unrot}	eq. (2.28)	Next order Fourier cosine coefficient when $\theta_{\kappa b} = 0$.
$C_{ss'}$		Collision operator.
$C^{(l)}_{ss'}$		Linearized collision operator.
d_w		Vacuum vessel wall thickness.
$D_{\Pi s}$		Species momentum diffusion constant.
D_{cm}		Lowest order Fourier sine coefficient, where $m \geq 0$ is an integer.
D_{hm}		Lowest order Fourier sine coefficient, where $m \geq 0$ is an integer.
D_m		Lowest order Fourier sine coefficient, where $m \geq 0$ is an integer.
D'_m		Next order Fourier sine coefficient, where $m \geq 0$ is an integer.
D_{Qs}		Species heat diffusion constant.
D'_{unrot}	eq. (2.29)	Next order Fourier sine coefficient when $\theta_{\kappa b} = 0$.
D_w		Diffusion constant of the vacuum vessel wall.
e		Proton charge.
$\hat{e}_l$		Unit vector in the l direction, $\hat{e}_l \equiv \vec{\nabla} l / \left\vert \vec{\nabla} l \right\vert$.
e		Electron subscript, indicating the electron species.
$\vec{E}$		Electric field.
$\mathscr{E}$		Particle energy, $\mathscr{E} \equiv m_s w^2/2$.
$E_e(k_e)$		The complete elliptic integral of the second kind, $E_e(k_e) \equiv \int_0^{\pi/2} d\alpha^\dagger \sqrt{1 - k_e^2 \sin^2(\alpha^\dagger)}$.
E_m		Stored magnetic field energy.
f_s		Distribution function.
$\vec{F}_{ext}$		External force acting on the plasma, $\vec{F}_{ext} \equiv \vec{I}_p \times \vec{B}_{ext}$.
F_{Ms}	eq. (1.13)	Maxwellian distribution function.
$\vec{F}_p$	eq. (2.100)	Total self-force acting on the plasma from the tire tube and hoop forces.

$\vec{F}_{p0}$		Total self-force acting on the plasma from the tire tube and hoop forces at the equilibrium position, $\vec{F}_{p0} \equiv \vec{F}_p\Big\vert_{R=R_{0b},Z=0}$.
$\vec{F}_{tot}$	eq. (2.98)	Sum of all forces acting on the plasma.
$_{gB}$	App. B	GyroBohm subscript, indicating gyroBohm estimates for a given quantity.
g_s	eq. (3.22)	Complementary distribution function.
G	eq. (2.61)	Free space Green's function.
$\bar{h}_s$	eq. (1.19)	Nonadiabatic portion of the distribution function.
h_s	eq. (1.20)	Fourier-analyzed nonadiabatic portion of the distribution function.
i		The imaginary unit, $i \equiv \sqrt{-1}$.
$_i$		Ion subscript, indicating the ion species.
I		Flux function related to the poloidal current, $I \equiv RB_\zeta = \mu_0 \int_{R_0}^{R_0+a} dR\,(Rj_Z\,(R, Z=0))$.
$I_m\,(x)$		m^{th} order modified Bessel function of the first kind.
I_p		Tokamak plasma current.
$\vec{j}$		Current density.
$j^{\pm}$		The direction of the TCV plasma current, positive is defined to be clockwise viewed from above the machine.
$J_m\,(x)$		m^{th} order Bessel function of the first kind.
$\vec{k}$		Mode angular wavenumber.
k_e	eq. (2.44)	Argument of the elliptic integrals.
k_{e0}		Argument of the elliptic integrals at the flux surface center, $k_{e0}\,(R, Z) \equiv k\,(R, Z, R_{0b}, 0)$.
$K_e\,(k_e)$		The complete elliptic integral of the first kind, $K_e\,(k_e) \equiv \int_0^{\pi/2} d\alpha^\dagger \left(1 - k_e^2 \sin^2\left(\alpha^\dagger\right)\right)^{-1/2}$.
l		Length.
l_i		Dimensionless internal inductance per unit length, $l_i \equiv \frac{\langle B_p^2 \rangle_V}{B_{pa}^2}$.
l_{corr}		Turbulence correlation length.

l_p		Characteristic size of the plasma.
L		Inductance.
^{L}		L superscript , indicates a lowest order quantity in the expansion parameter.
L_ζ		Tokamak toroidal circumference.
L_e		Contribution to the total inductance from outside the plasma.
L_i		Contribution to the total inductance from inside the plasma.
L_{ns}		Temperature scale length, $L_{ns} \equiv -n_s \left(\frac{\partial n_s}{\partial r_\psi}\right)^{-1}$.
L_p		Tokamak poloidal circumference.
L_{Ts}		Temperature scale length, $L_{Ts} \equiv -T_s \left(\frac{\partial T_s}{\partial r_\psi}\right)^{-1}$.
m		Poloidal mode number.
m_s		Particle mass.
n		Toroidal mode number.
$\hat{n}$	eq. (2.57)	The surface normal unit vector, pointing outwards from the plasma region.
n_c	eq. (2.102)	Decay index (also called the marginal index for stability).
n_s		Species density, $n_s \equiv \int d^3v\,(f_s)$.
^{N}		N superscript, indicates a next order quantity in the expansion parameter.
$_N$	table 3.1, table 3.2	N subscript, indicating a GS2 normalized quantity.
$O(\ldots)$		Indicates the order of terms that have been neglected.
p		Plasma thermal pressure, $p \equiv \sum_s n_s T_s$.
p_f		Volumetric fusion power density.
P_f		Total fusion power.
P_{loss}		Power lost out of the plasma boundaries.
Pr_s		Species Prandtl number, $Pr_s \equiv \frac{D_{\Pi s}}{D_{Qs}}$.

q		Tokamak safety factor, $q \equiv \frac{1}{2\pi} \oint\big\vert_{\psi} d\vartheta \left(\frac{I(\psi)}{R^2 \vec{B}\cdot\vec{\nabla}\vartheta}\right)$.
q_a		Tokamak edge safety factor, $q_a \equiv q\,(a)$.
q_{loc}		Tokamak local safety factor, $q_{loc} \equiv \frac{I(\psi)}{R^2 \vec{B}\cdot\vec{\nabla}\vartheta}$.
Q_{DT}		Total fusion energy yield per D-T reaction, $Q_{DT} = 17.6$ MeV.
Q_s	eq. (1.33)	Species flux surface averaged total heat flux.
r		Cylindrical radius, $r \equiv \sqrt{(R - R_0)^2 + Z^2}$.
$_r$		r subscript, indicating a GS2 reference quantity.
r_ψ	eq. (2.15)	Tokamak radius flux surface label, $r_\psi \equiv a\rho = a\sqrt{\psi/\psi_b}$.
$\vec{r}_p$	fig. 1-4	Particle position coordinate.
R	fig. 1-1	Tokamak major radial coordinate.
R^{new}	eq. (3.16)	Modified GS2 major radial flux surface parameterization.
R^{old}	eq. (3.3)	Original GS2 major radial flux surface parameterization.
$_R$		R subscript, indicating the vector component in the direction of $\hat{e}_R$.
$\vec{R}_{gc}$	fig. 1-4, eq. (1.16)	Particle guiding center position.
R_{geo}		GS2 magnetic field reference point.
R_{max}		The maximum value of R on a given flux surface.
R_{min}		The minimum value of R on a given flux surface.
R_0	fig. 1-1	Tokamak major radius.
$\hat{s}$	table 3.1	Tokamak magnetic shear.
$_s$		Species subscript, where $s \in \{i, e, r, tot, C\}$ indicating either ion, electron, reference, total, or carbon quantities respectively.
$_S$		Subscript S, indicating the sine coefficient in a Fourier series.
$s_{\Pi_{int}}$		The direction of the TCV intrinsic momentum flux, positive is will expel momentum from the tokamak core creating a more hollow rotation profile.

s_a	fig. 5-5	The sign of the TCV up-down asymmetry, given by the sign of θ_κ.
s_b		The direction of the TCV toroidal magnetic field, positive is defined to be clockwise viewed from above the machine.
s_j		The direction of the TCV plasma current, positive is defined to be clockwise viewed from above the machine.
s_Q		The sign of a given quantity, $s_Q \equiv \text{sign}\,(Q)$.
$\vec{S}$		Vector normal to a surface.
t		Time coordinate.
$\hat{t}$		The surface tangent unit vector in the poloidal plane.
t_{corr}		Turbulence correlation time.
t_{shot}		Duration of tokamak plasma shot.
T_s		Species temperature, $T_s \equiv \frac{2}{3n_s}\int d^3v\left(\frac{m_s}{2}v^2 f_s\right)$.
tot		Total subscript, indicating the quantity is summed over all species.
$\vec{u}$		Bulk plasma flow velocity, $\vec{u} \equiv \sum_s n_s m_s \vec{u}_s / \sum_s n_s m_s$.
$\vec{u}_s$		Species flow velocity, $\vec{u}_s \equiv \frac{1}{n_s}\int d^3v\,(\vec{v} f_s)$.
$\vec{v}$		Velocity coordinate.
$\vec{v}_\phi$		Fourier transformed turbulent $\vec{E}\times\vec{B}$ drift velocity, $\vec{v}_\phi \equiv -i\vec{k}\phi \times \vec{B}/B^2$.
$\vec{v}_{\phi s}$	eq. (1.30)	Species turbulent $\vec{E}\times\vec{B}$ drift velocity.
$\vec{v}_{ds}$	eq. (1.24), eq. (1.25)	Species guiding center particle drift velocity, $\vec{v}_{ds} \equiv \left(-\vec{\nabla}\Phi\times\vec{B}\right)/B^2 + \frac{\mu}{\Omega_s}\hat{b}\times\vec{\nabla}B + \frac{w_\parallel^2}{\Omega_s}\hat{b}\times\left(\hat{b}\cdot\vec{\nabla}\hat{b}\right)$.
v_{ths}		Thermal velocity, $v_{ths} \equiv \sqrt{2T_s/m_s}$.
V		Volume.
V_N		Normalized volume, $V_N \equiv V/l_r^3$.
$\vec{w}$		Velocity coordinate in the frame rotating with the bulk plasma flow, $\vec{w} \equiv \vec{v} - \vec{u}$.
W	eq. (1.3)	Plasma total stored energy.
x		Turbulence scale radial coordinate, $\hat{e}_x \equiv \hat{e}_\psi$.

X		Tokamak Coordinate, $X \equiv R - R_0 = r\cos(\theta)$.
X'		Tokamak Coordinate X in the coordinate system aligned with the ellipse axes.
y		Turbulence scale poloidal coordinate, $\hat{e}_y \equiv \hat{b} \times \hat{e}_\psi$.
Y		Tokamak Coordinate, $Y \equiv Z = r\sin(\theta)$.
Y'		Tokamak Coordinate Y in the coordinate system aligned with the ellipse axes.
Z		Axial coordinate.
Z^{new}	eq. (3.17)	Modified GS2 axial flux surface parameterization.
Z^{old}	eq. (3.4)	Original GS2 axial flux surface parameterization.
$_Z$		Z subscript, indicating the vector component in the direction of $\hat{e}_Z$.
Z_s		Particle charge number.

Appendix B

Gyrobohm units

GyroBohm diffusion is closely related to Bohm diffusion, which are both orderings of the cross-field diffusion coefficient. Bohm diffusion orders $D_{Bs} \sim \rho_s v_{ths}$, whereas gyroBohm is defined by the more optimistic ordering $D_{gBs} \sim \frac{\rho_s}{l_r} D_{Bs}$. The gyroBohm ordering has been found to be appropriate for turbulent transport and produces an ordering for the radial fluxes given by GS2 through Fick's first law of diffusion

$$\Gamma_s = -D_{\Gamma s} \frac{\partial n_s}{\partial r}, \tag{B.1}$$

$$\Pi_{\zeta s} = -D_{\Pi s} R^2 n_s m_s \frac{\partial \Omega_{\zeta s}}{\partial r}, \tag{B.2}$$

$$Q_s = -D_{Qs} n_s \frac{\partial T_s}{\partial r}. \tag{B.3}$$

Introducing the gyroBohm diffusion coefficient ordering we obtain

$$\Gamma_{gBs} \sim \frac{\rho_s^2 v_{ths}}{l_r} \frac{1}{l_r} \left(n_s \right), \tag{B.4}$$

$$\Pi_{gBs} \sim \frac{\rho_s^2 v_{ths}}{l_r} \frac{1}{l_r} \left(l_r n_s m_s v_{ths} \right), \tag{B.5}$$

$$Q_{gBs} \sim \frac{\rho_s^2 v_{ths}}{l_r} \frac{1}{l_r} \left(n_s T_s \right). \tag{B.6}$$

Therefore, the gyroBohm reference units are defined to be

$$\Gamma_{gBr} \equiv \frac{\rho_r^2}{l_r^2} n_r v_{thr}, \tag{B.7}$$

$$\Pi_{gBr} \equiv \frac{\rho_r^2}{l_r^2} n_r l_r m_r v_{thr}^2, \tag{B.8}$$

$$Q_{gBr} \equiv \frac{\rho_r^2}{l_r^2} n_r T_r v_{thr}. \tag{B.9}$$

All fluxes output by GS2 are normalized by these gyroBohm values.

Appendix C

GS2 Sample Input File

```
! CYCLONE BASE CASE ----------------------------------------

&collisions_knobs
 collision_model='none'
/

&hyper_knobs ! appropriate for nonlinear runs only
 hyper_option = 'visc_only'
 const_amp = .false.
 isotropic_shear = .false.
 D_hypervisc = 0.1
/

&theta_grid_parameters
 ntheta= 32
 nperiod= 1
 rhoc = 0.54
 qinp = 1.4
 Rmaj = 3.0
 R_geo = 3.0
 shift = 0.0
 akappa = 1.0
 akappri = 0.0
 tri = 0.0
 tripri = 0.0
 thetak = 0.0 ! parameter not included in standard GS2 distribution
 thetakp = 0.0 ! parameter not included in standard GS2 distribution
 thetad = 0.0 ! parameter not included in standard GS2 distribution
 thetadp = 0.0 ! parameter not included in standard GS2 distribution
/
```

```
&parameters
 beta = 0.0
 zeff = 1.0
/
&theta_grid_eik_knobs
 itor = 1
 iflux = 0
 irho = 2
 ppl_eq = F
 gen_eq = F
 efit_eq = F
 local_eq = T
 eqfile = 'dskeq.cdf'
 equal_arc = T
 bishop = 4
 s_hat_input = 0.8
 beta_prime_input = 0.0
 delrho = 1.e-3
 isym = 0
 writelots = F
/
&fields_knobs
 field_option='implicit'
/
&gs2_diagnostics_knobs
 print_flux_line = T
 write_nl_flux = T
 print_line = F
 write_line = F
 write_omega = F ! appropriate for linear runs only
 write_ascii = F
 write_final_fields = T
 write_symmetry = T
 write_eigenfunc = T
 write_g = F
 write_verr = F
 nwrite=     100
 navg=       50
 omegatinst = 500.0
 save_for_restart = .true.
 omegatol = -1.0e-3
/
&le_grids_knobs
 ngauss = 5
 negrid = 12
```

```
 vcut= 2.5
/
&dist_fn_knobs
 adiabatic_option="iphi00=2"
 gridfac=   1.0
 boundary_option="linked"
/

&kt_grids_knobs
 grid_option='box'
/
&kt_grids_box_parameters
 ! naky = (ny-1)/3 + 1
 ny = 64
 ! nakx = 2*(nx-1)/3 + 1
 nx = 192
 ! ky_min = 1/y0
 y0 = 10.0
 jtwist = 5
/
&init_g_knobs
 chop_side = F
 phiinit=   1.e-3
 restart_file = "nonlinearRun.nc"
 ginit_option= "noise"
/
&knobs
 fphi =   1.0
 fapar =  0.0
 faperp = 0.0
 delt = 0.05
 nstep = 100000
/
&species_knobs
 nspec=          2
/
&species_parameters_1
 z=   1.0
 mass=   1.0
 dens=   1.0
 temp=   1.0
 tprim=  2.300
 fprim=  0.733
 uprim=  0.0
 vnewk=  0.0
```

```
 type='ion'
/
&dist_fn_species_knobs_1
 fexpr= 0.45
 bakdif= 0.05
/
&species_parameters_2
 z=     -1.0
 mass=   2.7e-4
 dens=   1.0
 temp=   1.0
 tprim=  2.300
 fprim=  0.733
 uprim=  0.0
 vnewk=  0.0
 type='electron'
/
&dist_fn_species_knobs_2
 fexpr= 0.45
 bakdif= 0.05
/
&theta_grid_knobs
 equilibrium_option='eik'
/
&nonlinear_terms_knobs
 nonlinear_mode='on'
 cfl = 0.25
/
&reinit_knobs
 delt_adj = 2.0
 delt_minimum = 1.e-4
/
&layouts_knobs
 layout = 'lxyes'
 local_field_solve = F
/
```

Bibliography

[1] F.I. Parra, M. Barnes, and A.G. Peeters. Up-down symmetry of the turbulent transport of toroidal angular momentum in tokamaks. *Phys. Plasmas*, 18(6):062501, 2011.

[2] Y. Camenen, A.G. Peeters, C. Angioni, F.J. Casson, W.A. Hornsby, A.P. Snodin, and D. Strintzi. Transport of parallel momentum induced by current-symmetry breaking in toroidal plasmas. *Phys. Rev. Lett.*, 102:125001, 2009.

[3] A.M. Dimits, G. Bateman, M.A. Beer, B.I. Cohen, W. Dorland, G.W. Hammett, C. Kim, J.E. Kinsey, M. Kotschenreuther, A.H. Kritz, et al. Comparisons and physics basis of tokamak transport models and turbulence simulations. *Phys. Plasmas*, 7:969, 2000.

[4] M. Greenwald. Fusion plasmas. *Wiley Encyclopedia of Electrical and Electronics Engineering*, 2001.

[5] R. Aymar et al. Summary of the ITER final design report. *ITER document G A0 FDR*, 4:01, 2001.

[6] J. Wesson. *Tokamaks*, chapter 1.5, page 11. Oxford University Press, third edition, 2004.

[7] F. Troyon, R. Gruber, H. Saurenmann, S. Semenzato, and S. Succi. MHD-limits to plasma confinement. *Plasma Phys. Control. Fusion*, 26(1A):209, 1984.

[8] J. Wesson. *Tokamaks*, chapter 6.16, page 347. Oxford University Press, third edition, 2004.

[9] F.L. Hinton and S.K. Wong. Neoclassical ion transport in rotating axisymmetric plasmas. *Physics of Fluids*, 28:3082, 1985.

[10] P.J. Catto, I.B. Bernstein, and M. Tessarotto. Ion transport in toroidally rotating tokamak plasmas. *Physics of Fluids*, 30:2784, 1987.

[11] A.E. White, L. Schmitz, G.R. McKee, C. Holland, W.A. Peebles, T.A. Carter, M.W. Shafer, M.E. Austin, K.H. Burrell, J. Candy, et al. Measurements of core electron temperature and density fluctuations in DIII-D and comparison to nonlinear gyrokinetic simulations. *Physics of Plasmas*, 15(5):056116, 2008.

[12] J. Citrin, C. Bourdelle, J.W. Haverkort, G.M.D. Hogeweij, F. Jenko, P. Mantica, M.J. Pueschel, D. Told, et al. Ion temperature profile stiffness: nonlinear gyrokinetic simulations and comparison with experiment. *arXiv preprint arXiv:1303.2217*, 2013.

[13] N.T. Howard, M. Greenwald, D.R. Mikkelsen, A.E. White, M.L. Reinke, D. Ernst, Y. Podpaly, and J. Candy. Measurement of plasma current dependent changes in impurity transport and comparison with nonlinear gyrokinetic simulation. *Physics of Plasmas*, 19:056110, 2012.

[14] F.I. Parra and P.J. Catto. Turbulent transport of toroidal angular momentum in low flow gyrokinetics. *Plasma Physics and Controlled Fusion*, 52(4):045004, 2010.

[15] C.P. Ritz, H. Lin, T.L. Rhodes, and A.J. Wootton. Evidence for confinement improvement by velocity-shear suppression of edge turbulence. *Phys. Rev. Lett.*, 65(20):2543, 1990.

[16] K.H. Burrell. Effects of $E \times B$ velocity shear and magnetic shear on turbulence and transport in magnetic confinement devices. *Phys. Plasmas*, 4(5):1499, 1997.

[17] M. Barnes, F.I. Parra, E.G. Highcock, A.A. Schekochihin, S.C. Cowley, and C.M. Roach. Turbulent transport in tokamak plasmas with rotational shear. *Phys. Rev. Lett.*, 106(17):175004, 2011.

[18] E.G. Highcock, M. Barnes, A.A. Schekochihin, F.I. Parra, C.M. Roach, and S.C. Cowley. Transport bifurcation in a rotating tokamak plasma. *Phys. Rev. Lett.*, 105(21):215003, 2010.

[19] F.I. Parra, M. Barnes, E.G. Highcock, A.A. Schekochihin, and S.C. Cowley. Momentum injection in tokamak plasmas and transitions to reduced transport. *Phys. Rev. Lett.*, 106(11):115004, 2011.

[20] E.G. Highcock. *The Zero-Turbulence Manifold in Fusion Plasmas.* PhD thesis, University of Oxford, April 2012.

[21] P.W. Terry. Suppression of turbulence and transport by sheared flow. *Rev. Mod. Phys.*, 72:109, 2000.

[22] J. Wesson. *Tokamaks*, chapter 6.9, page 328. Oxford University Press, third edition, 2004.

[23] L.E. Zakharov and S.V. Putvinskii. Effect of plasma rotation in a tokamak on the stabilizing effect of a conducting wall. *Sov. J. Plasma Phys*, 13:68, 1987.

[24] H. Reimerdes, T.C. Hender, S.A. Sabbagh, J.M. Bialek, M.S. Chu, A.M. Garofalo, M.P. Gryaznevich, D.F. Howell, G.L. Jackson, R.J. La Haye, et al. Cross-machine comparison of resonant field amplification and resistive wall mode stabilization by plasma rotation. *Physics of Plasmas*, 13(5):56107, 2006.

[25] A. Bondeson and M. Persson. Stabilization by resistive walls and q-limit disruptions in tokamaks. *Nuclear fusion*, 28(10):1887, 1988.

[26] E.J. Strait, T.S. Taylor, A.D. Turnbull, J.R. Ferron, L.L. Lao, B. Rice, O. Sauter, S.J. Thompson, and D. Wróblewski. Wall stabilization of high beta tokamak discharges in DIII-D. *Phys. Rev. Lett.*, 74(13):2483, 1995.

[27] C.G. Gimblett. On free boundary instabilities induced by a resistive wall. *Nuclear fusion*, 26(5):617, 1986.

[28] A. Bondeson and D.J. Ward. Stabilization of external modes in tokamaks by resistive walls and plasma rotation. *Phys. Rev. Lett.*, 72:2709, 1994.

[29] B. Hu and R. Betti. Resistive wall mode in collisionless quasistationary plasmas. *Phys. Rev. Lett.*, 93(10):105002, 2004.

[30] J.M. Finn. Stabilization of ideal plasma resistive wall modes in cylindrical geometry: The effect of resistive layers. *Physics of Plasmas*, 2:3782, 1995.

[31] R. Betti and J.P. Freidberg. Stability analysis of resistive wall kink modes in rotating plasmas. *Phys. Rev. Lett.*, 74(15):2949, 1995.

[32] A.M. Garofalo, E.J. Strait, L.C. Johnson, R.J. La Haye, E.A. Lazarus, G.A. Navratil, M. Okabayashi, J.T. Scoville, T.S. Taylor, and A.D. Turnbull. Sustained stabilization of the resistive-wall mode by plasma rotation in the DIII-D tokamak. *Phys. Rev. Lett.*, 89(23):235001, 2002.

[33] S.A. Sabbagh, R.E. Bell, M.G. Bell, J. Bialek, A.H. Glasser, B. LeBlanc, J.E. Menard, F. Paoletti, D. Stutman, E. Fredrickson, et al. Beta-limiting instabilities and global mode stabilization in the national spherical torus experiment. *Physics of Plasmas*, 9(5):2085, 2002.

[34] P.C. de Vries, G. Waidmann, A.J.H. Donné, and F.C. Schüller. MHD-mode stabilization by plasma rotation in TEXTOR. *Plasma Phys. Control. Fusion*, 38(4):467, 1996.

[35] S. Suckewer, H.P. Eubank, R.J. Goldston, E. Hinnov, and N.R. Sauthoff. Toroidal plasma rotation in the Princeton Large Torus induced by neutral-beam injection. *Phys. Rev. Lett.*, 43(3):207, 1979.

[36] J.E. Rice, A. Ince-Cushman, L.-G. Eriksson, Y. Sakamoto, A. Scarabosio, A. Bortolon, K.H. Burrell, B.P. Duval, C. Fenzi-Bonizec, M.J. Greenwald, et al. Inter-machine comparison of intrinsic toroidal rotation in tokamaks. *Nuclear Fusion*, 47(11):1618, 2007.

[37] G.G. Howes, S.C. Cowley, W. Dorland, G.W. Hammett, E. Quataert, and A.A. Schekochihin. Astrophysical gyrokinetics: Basic equations and linear theory. *ApJ*, 651(1):590, 2006.

[38] P.J. Catto. Linearized gyro-kinetics. *Plasma Physics*, 20(7):719, 1978.

[39] E.A. Frieman and L. Chen. Nonlinear gyrokinetic equations for low-frequency electromagnetic waves in general plasma equilibria. *Physics of Fluids*, 25:502, 1982.

[40] F.I. Parra and P.J. Catto. Limitations of gyrokinetics on transport time scales. *Plasma Physics and Controlled Fusion*, 50(6):065014, 2008.

[41] I.G. Abel, G.G. Plunk, E. Wang, M.A. Barnes, S.C. Cowley, W. Dorland, and A.A. Schekochihin. Multiscale gyrokinetics for rotating tokamak plasmas: Fluctuations and transport. *Rep. Prog. Phys*, 2012.

[42] G.R. McKee, C.C. Petty, R.E. Waltz, C. Fenzi, R.J. Fonck, J.E. Kinsey, T.C. Luce, K.H. Burrell, D.R. Baker, E.J. Doyle, et al. Non-dimensional scaling of turbulence characteristics and turbulent diffusivity. *Nuclear Fusion*, 41(9):1235, 2001.

[43] H. Sugama, T.H. Watanabe, M. Nunami, and S. Nishimura. Momentum balance and radial electric fields in axisymmetric and nonaxisymmetric toroidal plasmas. *Plasma Phys. Control. Fusion*, 53(2):024004, 2011.

[44] Y. Camenen, Y. Idomura, S. Jolliet, and A.G. Peeters. Consequences of profile shearing on toroidal momentum transport. *Nuclear Fusion*, 51(7):073039, 2011.

[45] M. Barnes, F.I. Parra, J.P. Lee, E.A. Belli, M.F.F. Nave, and A.E. White. Intrinsic rotation driven by non-maxwellian equilibria in tokamak plasmas. 2013.

[46] Y. Camenen, A.G. Peeters, C. Angioni, F.J. Casson, W.A. Hornsby, A.P. Snodin, and D. Strintzi. Intrinsic rotation driven by the electrostatic turbulence in up-down asymmetric toroidal plasmas. *Phys. Plasmas*, 16(6):062501, 2009.

[47] A.G. Peeters and D. Strintzi. The effect of a uniform radial electric field on the toroidal ion temperature gradient mode. *Phys. Plasmas*, 11:3748, 2004.

[48] H. Lütjens, A. Bondeson, and A. Roy. Axisymmetric MHD equilibrium solver with bicubic Hermite elements. *Computer Physics Communications*, 69(2):287, 1992.

[49] J.P. Freidberg. *Ideal Magnetohydrodynamics.* Plenum Press, New York, NY, 1987.

[50] A. Kuiroukidis and G.N. Throumoulopoulos. Symmetric and asymmetric equilibria with non-parallel flows. *Phys. Plasmas*, 19(2):022508, 2012.

[51] J.P. Freidberg. *Ideal Magnetohydrodynamics*, chapter 6.4, page 126. Plenum Press, New York, NY, 1987.

[52] J.P. Freidberg. *Plasma Physics and Fusion Energy*, chapter 11.7, page 271. Cambridge University Press, 2007.

[53] S.P. Hakkarainen, R. Betti, J.P. Freidberg, and R. Gormley. Natural elongation and triangularity of tokamak equilibria. *Physics of Fluids B: Plasma Physics*, 2:1565, 1990.

[54] J. Jackson. *Classical Electrodynamics*, chapter 5.5, page 123. Wiley, third edition, 1999.

[55] M. Ariola and A. Pironti. *Magnetic control of tokamak plasmas*, page 144. Springer, 2008.

[56] M.S. Chance, A.D. Turnbull, and P.B. Snyder. Calculation of the vacuum green's function valid even for high toroidal mode numbers in tokamaks. *Journal of Computational Physics*, 221(1):330, 2007.

[57] J. Wesson. *Tokamaks*, chapter 3.8, page 123. Oxford University Press, third edition, 2004.

[58] O. Gruber, K. Lackner, G. Pautasso, U. Seidel, and B. Streibl. Vertical displacement events and halo currents. *Plasma Phys. Control. Fusion*, 35(SB):B191, 1993.

[59] P.H. Rebut, R.J. Bickerton, and B.E. Keen. The Joint European Torus: installation, first results and prospects. *Nuclear Fusion*, 25(9):1011, 1985.

[60] M. Sugihara, M. Shimada, H. Fujieda, Y. Gribov, K. Ioki, Y. Kawano, R. Khayrutdinov, V. Lukash, and J. Ohmori. Disruption scenarios, their mitigation and operation window in ITER. *Nuclear Fusion*, 47(4):337, 2007.

[61] V.S. Mukhovatov and V.D. Shafranov. Plasma equilibrium in a tokamak. *Nuclear Fusion*, 11(6):605, 1971.

[62] H.P. Furth and S. Yoshikawa. Adiabatic compression of tokamak discharges. *Physics of Fluids*, 13:2593, 1970.

[63] M. Kotschenreuther, G. Rewoldt, and W.M. Tang. Comparison of initial value and eigenvalue codes for kinetic toroidal plasma instabilities. *Computer Physics Communications*, 88(2):128–140, 1995.

[64] R.L. Miller, M.S. Chu, J.M. Greene, Y.R. Lin-Liu, and R.E. Waltz. Noncircular, finite aspect ratio, local equilibrium model. *Phys. Plasmas*, 5(4):973, 1998.

[65] L.L. Lao, J.R. Ferron, R.J. Groebner, W. Howl, H. St. John, E.J. Strait, and T.S. Taylor. Equilibrium analysis of current profiles in tokamaks. *Nuclear Fusion*, 30(6):1035, 1990.

[66] R.L. Miller and J.W. Van Dam. Hot particle stabilization of ballooning modes in tokamaks. *Nuclear Fusion*, 27(12):2101, 1987.

[67] P.M. De Zeeuw. Matrix-dependent prolongations and restrictions in a blackbox multigrid solver. *Journal of Computational and Applied Mathematics*, 33(1):1, 1990.

[68] J. DeLucia, S.C. Jardin, and A.M.M. Todd. An iterative metric method for solving the inverse tokamak equilibrium problem. *Journal of Computational Physics*, 37(2):183, 1980.

[69] J.M. Greene and M.S. Chance. The second region of stability against ballooning modes. *Nuclear Fusion*, 21(4):453, 1981.

[70] M.A. Barnes. *Trinity: A Unified Treatment of Turbulence, Transport, and Heating in Magnetized Plasmas.* PhD thesis, University of Maryland, January 2008.

[71] J. Kesner, J.J. Ramos, and F.-Y. Gang. Comet cross-section tokamaks. *Journal of Fusion Energy*, 14(4):361, 1995.

[72] M. Greenwald, R.L. Boivin, F. Bombarda, P.T. Bonoli, C.L. Fiore, D. Garnier, J.A. Goetz, S.N. Golovato, M.A. Graf, R.S. Granetz, et al. H mode confinement in Alcator C-Mod. *Nuclear Fusion*, 37(6):793, 1997.

[73] C.M. Bishop, P. Kirby, J.W. Connor, R.J. Hastie, and J.B. Taylor. Ideal MHD ballooning stability in the vicinity of a separatrix. *Nuclear fusion*, 24(12):1579, 1984.

[74] Y. Camenen, A. Bortolon, B.P. Duval, L. Federspiel, A.G. Peeters, F.J. Casson, W.A. Hornsby, A.N. Karpushov, F. Piras, O. Sauter, A.P. Snodin, G. Szepesi, and the TCV Team. Experimental demonstration of an up-down asymmetry effect on intrinsic rotation in the TCV tokamak. *Plasma Phys. Control. Fusion*, 52(12):1, 2010.

[75] Y. Camenen, A. Bortolon, B.P. Duval, L. Federspiel, A.G. Peeters, F.J. Casson, W.A. Hornsby, A.N. Karpushov, F. Piras, O. Sauter, et al. Experimental evidence of momentum transport induced by an up-down asymmetric magnetic equilibrium in toroidal plasmas. *Phys. Rev. Lett.*, 105(13):135003, 2010.

[76] J. Wesson. *Tokamaks*, chapter 11.20, page 589. Oxford University Press, third edition, 2004.

[77] F. Hofmann, J.B. Lister, W. Anton, S. Barry, R. Behn, S. Bernel, G. Besson, F. Buhlmann, R. Chavan, M. Corboz, et al. Creation and control of variably shaped plasmas in TCV. *Plasma Phys. Control. Fusion*, 36(12B):B277, 1994.